Evaluate and Design Battery Support Services for the Electrical Grid

by

Brian de Beer

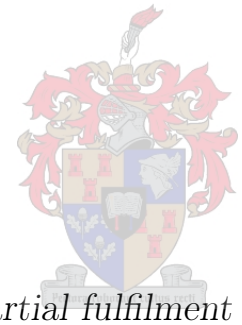

Thesis presented in partial fulfilment of the requirements for the degree of Master of Engineering (Electric and Electronic) in the Faculty of Engineering at Stellenbosch University

Supervisor: Dr. Arnold J. Rix

December 2017

Declaration

By submitting this thesis electronically, I declare that the entirety of the work contained therein is my own, original work, that I am the sole author thereof (save to the extent explicitly otherwise stated), that reproduction and publication thereof by Stellenbosch University will not infringe any third party rights and that I have not previously in its entirety or in part submitted it for obtaining any qualification.

Date: December 2017

Abstract

Evaluate and Design Battery Support Services for the Electrical Grid

B. De Beer

Department of Electric and Electronic Engineering,
University of Stellenbosch,
Private Bag X1, Matieland 7602, South Africa.

Thesis: MEng (Electric and Electronic)

September 2017

Aside from the many existing problems on the electric network; new problems have been introduced with the increased adoption of renewable energy sources. In this thesis, how battery storage systems can be applied in order to address some of the problems is investigated. These problems include: addressing the intermittent nature of photovoltaic power plants, integrating larger photovoltaic power plant into a weak network and optimising battery storage sizing for peak load shaving.

The intermittent nature of photovoltaic systems becomes a problem when there is a high penetration thereof on the electric network because the fluctuating power output is reflected in the network. Fluctuation mitigation methods, incorporating battery storage systems, are investigated and the ramp-rate control strategy is chosen for further analysis. How the strategy influences the battery storage sizing, performance and cost is analysed.

To analyse the impact the ramp-rate strategy has on the performance of a battery type, a battery has to be modelled. How batteries are modelled is investigated and an energy-throughput model is selected to be implemented as a tool. The tool is calibrated for two battery chemistries: a lithium ($LiFePO_4$) and lead-acid ($PbSO_4$) chemistry. It is found that the model favours chemistries, such as the $LiFePO_4$ chemistry, because of its linear degrading nature.

The integration of larger photovoltaic installations on a weak network is investigated. Weak networks, such as high impedance radial networks, can limit power plant installations to weak connections that can restrict the power plant installation capacity. The modelling of weak networks is investigated and one such a model is implemented in DIgSILENT PowerFactory. As a solution, control systems are created where a battery storage system can work in conjunction with an on-load tap changing transformer to prevent abnormal operating conditions during a sudden power loss. Also investigated is how the battery system should be sized in order to provide this support. It is found that batteries

can strengthen the network during sudden power loss conditions. It is also found that the battery systems must be sized for high power output.

The last problem that is investigated is the sizing of battery storage systems for peak load shaving. Battery storage systems are usually sized for the worst case scenario but often the worst case is an anomalous case. A statistical tool called Cook's distance is implemented to identify outlying cases in the load profiles and remove them. The original sizing strategy is optimised and implemented in Python as a tool. Finally, the original sizing strategy is compared to optimised strategy and it is found that in most of the cases the optimised strategy can improve the energy or power requirements.

Finally, the costs of each of the three problems are analysed. It is found that the battery energy storage systems required for PV output fluctuation mitigation make a substantial contribution to the levelised cost of the energy of the PV installation. The same is also found with regards to the battery energy storage system used for network strengthening; however reducing the PV installation capacity can reduce the costs considerably. For the optimised battery sizing strategy, for peak load shaving; levelised costs of energy savings of up to 24% are achieved.

Uittreksel

Evalueer en Ontwerp Battery Ondersteuningsdienste vir die Elektriese Netwerk

("Evaluate and Design Battery Support Services for the Electrical Grid")

B. De Beer

Departement Elektries en Elektronies Ingenieurswese,
Universiteit van Stellenbosch,
Privaatsak X1, Matieland 7602, Suid Afrika.

Tesis: MIng (Elektries en Elektronies)

September 2017

Afgesien van die baie bestaande probleme op die elektriese netwerk, is nuwe probleme aan die lig gebring met die verhoogde aanname van hernubare energiebronne. In hierdie proefskrif, is daar ondersoek hoe batterystelsels toegepas kan word om sommige van hierdie probleme aan te spreek. Hierdie probleme sluit in: die aanspreek van die wisselende aard van fotovoltaïese kragsentrales, die integrasie van groter fotovoltaïese kragstasies op swak netwerke en die optimalisering van battery groottes wat gebruik is vir piek las vermindering.

Die wisselende aard van fotovoltaïese stelsels is 'n probleem wanneer daar 'n hoë penetrasie daarvan op die elektriese netwerk is, omdat dit in die netwerk weerspieël word. Fluktuasie demperstrategieë wat gepaard gaan met battery stelsels, is ondersoek en 'n strategie wat omsetter-uittree beheer toepas is gekies vir verdere analise. Hoe die strategie die battery spesifikasies, prestasie en koste beïnvloed, is ontleed.

Dit is nodig om die impak wat die omsetter beheer strategie het op die battery, te bestudeer. Om dit te kan doen, moet die battery gemodelleer kan word. 'n Ondersoek is gedeon op verskillende battery modelle en 'n energie-deurvoermodel is gekies om implementeer te word en te dien as instrument vir verdere ontledings. Hierdie model is gekalibreer vir twee battery chemikalieë: litium ($LiFePO_4$) en loodsuur ($PbSO_4$). Daar word bevind dat die model voorkeur verleen aan die chemikalie, LiFePO4, as gevolg van sy lineêre verswakkende natuur.

Die integrasie van groter fotovoltaïese installasies op swak netwerke is ondersoek. Swak netwerke, soos hoë impedansie radiale netwerke, kan kragsentrales beperk tot swak verbindingspunte op die netwerk. Die swak netwerk eienskappe by die verbindingspunte kan die installasie kapasiteit van kragsentrales beperk. Die modellering van swak netwerke is ondersoek en een so 'n model is geïmplementeer in DIgSILENT PowerFactory. 'n Beheerstelsel word geskep wat die batterystelsel in staat stel om saam met die verstelbare

transformator te werk. Dit is geïmplementeer as oplossing om abnormale operasionele toestande gedurende skielike kragverlies te vermy. Daar is ook ondersoek hoe groot die batterystelsels moet wees om die nodige ondersteuning te bied. Dit is gevind dat die batterystelsel wel instaat is om die network te versterk teen skielike kragverliese. Daar is ook bevind dat die batterystelsels vir hoë krag ontwerp moet word.

Die laaste probleem wat ondersoek is, is die skalering van die batterystelsels vir pieklasvermiddering. Batterystelsels is gewoonlik geskaleer vir die uiterste gevalle, maar baie van die gevalle is uitskieter gevalle. 'n Statistiese instrument genaamd Cook se afstand, is geïmplementeer om afwykende gevalle te identifiseer en uit lasprofiele te verwyder. Die oorspronklike strategie waarmee batterystelsel geskaleer word, is geöptimaliseer en geïmplementeer in Python as 'n instrument. Ten slotte, is die oorspronklike strategie vergelyk met die geöptimaliseerde strategie en daar is bevind dat die geöptimaliseerde strategie die meeste van die gevalle kan verbeter ten opsigte van energie- of kragvereistes.

Ten slotte is die koste van elk van die drie probleme ontleed. Daar is bevind dat die batterystelsels wat benodig is vir die fluktuasie demping van die fotovoltaïese uitset, 'n wesenlike bydrae maak tot die gelyke koste van energie van die PV kragsentrale. Dieselfde geld ook vir die batterystelsel wat gebruik is vir netwerkversterking. As die fotovoltaïese installasie kapasiteit egter verminder is, kan die koste aansienlik verminder. Vir die geöptimaliseerde battery skalering strategie vir pieklasvermindering, kan 'n kostebesparing van tot 24% behaal word.

Acknowledgements

First and foremost, I offer my sincerest gratitude to my supervisor, Dr Arnold J. Rix, who has supported me throughout my thesis with his patience and knowledge whilst allowing me the room to work in my own way. I attribute the level of my masters degree to his encouragement and effort and without him this thesis could not have been done. One simply could not wish for a better or friendlier supervisor.

Thank you to my parents, Izak and Riana de Beer, for their financial and emotional support and for never giving up on me. Thank you for always being there and being my source of encouragement. My sincere thanks also go to my girlfriend, Catherine Gordon-Grant, for her unfailing support and continuous encouragement throughout the two years of my study.

I would like to thank my friends and fellow office mates: Armand Du Plessis, Tafadzwa Gurupira and JP Botha for their time, knowledge and endless banter that got me through the stressful times.

A big thanks to Scatec Solar and my supervisor for providing the opportunity to pursue a masters degree.

Last but certainly not least, I would like to thank my heavenly Father for His grace, power, wisdom and perseverance that carried me to the end.

Author

Brian de Beer

Dedications

This thesis is dedicated to my parents

Contents

List of Figures

List of Tables

Nomenclature

Constants

$k =$ $1.381 \times 10^{-23}\ J/K$

$R =$ $8.314\ J/mol{\cdot}K$

$q =$ $1.602 \times 10^{-19}\ C$

Variables

B	Pre-exponential factor	[ ]
C	Capacitance	[F]
c	c-rate (Charge/discharge rate)	[ ]
C_{BESS}	Capital cost of BESS per unit energy generated	[USD/kWh]
C_{BOS}	Balance of system cost	[USD/kW]
$C_{batteris}$	Cost of batteries	[USD/kWh]
C_{inst}	Installed system cost	[USD/kW]
$C_{O\&M}$	Operation and maintenance cost	[USD/kW]
E_{total}	Total energy yield	[kWh]
$E_{discharged}$	Total energy discharge	[kWh]
γ	Inverse characteristic constant	[ ]
D_i	Cook's distance	[ ]
E_a	Activation Energy	[J/mol]
E_{bat}	Battery energy capacity	[Wh]
E_{BESS}	BESS energy requirement	[Wh]
E_i	Energy yield for the year	[kWh]
$E_{per.MW}$	Energy yield per year of 1 MW PV installation	[kWh]
G	Conductance	[S]
h_i	Hat value	[ ]
$h_i i$	Leverage	[ ]

I	Current	[A]
I_D	Diode current	[A]
I_L	Light-generated current	[A]
I_{sc}	Short-circuit current	[A]
I_R	Receiving end current	[A]
I_S	Sending end current	[A]
k	k-th data point	[ ]
$LCOE$	Levelised cost of energy	[USD/kWh]
$LCOE_{BESS}$	Levelised cost of energy for BESS	[USD/kWh]
$LCOE_{opt}$	Levelised cost of optimised sizing strategy	[USD/kWh]
$LCOE_{ori}$	Levelised cost of original sizing strategy	[USD/kWh]
$LCOE_{PV}$	Levelised cost of energy for PV	[USD/kWh]
L	Inductance	[H]
ℓ	Distance	[km]
MSE_i	Mean square error	[ ]
N	Number if battery cycles	[ ]
η_{inv}	Inverter efficiency	[%]
η_{PCU}	Power conversion unit efficiency	[%]
η_{rep}	Number of battery replacements	[ ]
P_{BESS}	BESS power requirement	[W]
P_{comp}	Compensation power	[W]
P_{DC}	DC power output	[W]
P_des	Desired power	[kW]
P_{inv}	Inverter power output	[W]
EP_{load}	Load power level	[kW]
P_{PV}	Photovoltaic power output	[W]
R	Resistance	[Ω]
R_{pu}	Per unit resistance	[p.u.]
r_i	Studentised residuals	[ ]
RR_{adj}	Adjustment ramp-rate	[W/min]
RR_{comp}	Compensation ramp-rate	[W/min]
RR_{des}	Desired ramp-rate	[W/min]

RR_{PV}	Photovoltaic ramp-rate	[W/min]
σ_{red}	Percentage reduction	[%]
S	Switching variable	[ ]
S	Apparent power	[VA]
S_{PV}	Rated PV power	[p.u.]
S_{SC}	Short-circuit power	[p.u.]
SCR	Short-circuit ratio	[ ]
SOC	State-of-charge	[%]
SOV_{buff}	State-of-charge buffer	[%]
SOC_{LL}	State-of-charge lower limit	[%]
SOC_{UL}	State-of-charge upper limit	[%]
SOH	State-of-health	[%]
T	Temperature	[K]
U_n	Nominal voltage	[V]
U_PCC	Voltage at point of common coupling	[V]
Q	Energy charge and discharge	[Ah]
Q	Reactive power	[VAr]
Q_c	Cell initial energy capacity	[Ah]
V_d	Diode voltage	[V]
V_{OC}	Open-circuit voltage	[V]
V_R	Receiving end voltage	[V]
V_S	Sending end voltage	[V]
X	Inductive component	[H]
$X_{L.pu}$	Per unit inductive component	[p.u.]
xrr	X/R-ratio	[ ]
Y	Shunt admittance	[S]
Z_{base}	Base impedance	[p.u.]
Z_{grid}	Grid impedance	[p.u.]
Z_{PCC}	Impedance seen by point of common coupling	[p.u.]
Z_{TL}	Transmission line impedance	[p.u.]
Z_{weak}	Weak network impedance	[p.u.]

z Power law factor . . . . . [ ]

Subscripts

0 Initial value

i i-th data point

max maximum value

min minimum value

Abbreviations

AC Alternating Current

BESS Battery Energy Storage System

BOS Balance of System

DC Direct Current

DOD Depth-of-Discharge

DPF DIgSILENT PowerFactory

EV Electric vehicle

FB Flow Battery

GM General Motors

HEV Hybrid-Electric Vehicle

IED Intelligent Electronic Devices

IPP Independent Power Producers

LCOE Levelise Cost of Energy

MSE Mean Square Error

MPPT Maximum Power Point Tracker

NREL National Renewable Energy Laboratory

NSP National Service Provider

OLTC On-load Tap Changing

PCC Point of Common Coupling

PCU Power Conversion Unit

PF Power Factor

PV Photovoltaic

REIPPPP Renewable Energy Independent Power Procurement Programme

RMS Root Mean Square

RPP Renewable Power Plant

SA South Africa

SCADA Supervisory Control and Data Acquisition

SCR Short-Circuit Ratio

SOC State-of-Charge

SOH State-of-Health

UPS Uninterrupted Power Supply

Chapter 1

Introduction

1.1 Research Background

Research shows that 2016 was one of the best years with regards to the growth of the renewable energy sector and it is expected to keep on growing [1]. Some of the world's leading companies, such as Apple Inc. and Tesla, are becoming involved in renewable energy and this is not only due the push for sustainability. The renewable energy fields are showing significant returns on investment, and thus it makes economical sense for businesses to invest [1]. The growth in the renewable industry has driven down the prices of the technologies involved, making it more accessible to entrepreneurs and consumers. With the increased affordability in renewable energy and the network service provider, ESKOM, struggling to provide enough energy to meet the demand; the Department of Energy (DoE) established a public-private partnership known as the Renewable Energy Independent Power Producer Procurement Program (REIPPPP) [2]. This partnership aims to generate 45% of the new electricity from renewable energy sources by 2030 [2].

The adoption of renewable energy sources does not come without challenges. It is well-known that the intermittent nature of renewable energy sources can be problematic especially with higher penetration [3, 4]. This is where battery energy storage systems can be used. Batteries have the capability to store energy for later use. Incorporating batteries into the current electric network can assist with the stability particularly in areas such as renewable energy integration [5]. There are also problems on the electric network that do not pertain to renewable energy sources where batteries are applicable such as overloaded distribution feeders [6]. Battery storage costs have reduced by almost 80% in the last 6 years making batteries more affordable for the energy and electric vehicles markets [7]. Batteries are at the point where they make financial sense to consider for problems pertaining to the electrical network.

Given the complex nature of electric networks, there are many unsolved problems. There are also many solutions to other solved problems. All these solutions typically have one aspect in common: the potential user is not informed of the costs and of how applying the solution will change the cost point. The purpose of this thesis is to provide users with the means to assess the solutions to certain problems so that the required information can be obtained. The aim is to provide a solution whilst answering the questions that usually go unanswered such as how does applying the solution affect utilities financially and how do changes to the solution affect the resulting costs?

In this thesis, three different problems are identified where a battery energy storage system

(BESS) is applicable: the intermittent nature of photovoltaics (PV), PV integration on weak networks and the BESS sizing for overloaded distribution feeders. The intermittent nature of PV is investigated in order to identify solutions that ensure a more stable power output. Weak networks are sensitive to voltage instability; thus, how the network can be strengthened to allow for the integration of larger PV installations is investigated. The optimisation of the BESS sizing strategy is investigated in order to identify possible cost saving points. The cost of each of the solutions will be assessed in order to provide utilities with more information regarding the use of these solutions.

1.2 Problem Statement

A few problems have been identified for further investigation: the fluctuating nature of renewable energy sources, integration of PV on weak networks and BESS sizing for peak load shaving. The situation utilities find themselves in is that there is a lack of the required cost estimations in order for companies to commit to investing in these solutions. A deeper investigation is done into these problems and their respective solutions.

1.2.1 Fluctuation Mitigation for PV Installations

The push for the adoption of renewable energy sources, such as PV, results in an increased penetration of an unstable energy source. The intermittent nature of the source is of concern with regards to the stability and reliability of the electric network because the fluctuations are reflected in the network [8]. In South Africa the electric network does not have a high penetration of renewable energy yet but the targets set by the REIPPPP can change this in the future. The stability is not only an issue in larger public electric networks but also in smaller micro-grids [9].

The managers of utilities, in the market of renewable power plants, that operate on these various networks (the public electric network and micro-grids) are interested in the solutions as they will assist them with the integration of the power plants. However, these managers lack critical information on the costs of the application of these solutions. Thus, how the fluctuations of PV installations can be mitigated using a BESS and how applying these methods influence the cost of the PV installations is investigated. This is done whilst providing the tools necessary for utilities to assess their own respective case studies. The problem will be approached with the following objectives in mind:

- To identify an appropriate fluctuation mitigation method.
- To create a tool with which to asses the fluctuation mitigation method.
- To assess how the fluctuation mitigation method impacts battery performance.
- To assess how the fluctuation mitigation method influences the BESS sizing.
- To assess how the fluctuation mitigation method influences the total system cost.

It is not in the scope of this thesis to compare the various fluctuation mitigation models in detail. It is also not in the scope of this thesis to provide definitive results about the models because these differ on a case to case basis. The aims is to provide users with the means to assess a scenario. It is not in the scope of this thesis to do a detailed financial

breakdown of the costs involved but rather to do an assessment of the basic levelised cost of energy of each subsystem.

1.2.1.1 Battery Performance Modelling

In order to assess how the fluctuation mitigation model influences the battery performance, a battery model is required. The problem with battery models is that they tend to be very complicated and difficult to implement. What battery modelling methods exist and which method is simple to implement is investigated. The following objectives are set:

- To investigate and select a battery modelling strategy.
- To create a tool to use the model and assess battery performance.
- To apply the tool to at least two battery chemistries.

It is not in the scope of this thesis to develop a new modelling method but rather to choose an easy-to-implement model with which users can estimate battery performance. It is also not in the scope of this thesis to compare the various different battery technologies with one another but rather to show how the model works by applying it to two common battery chemistries from two competing battery technologies.

1.2.2 Network Strengthening for PV Installations

In South Africa, utility scale PV power plants are located at remote locations in the Northern Cape. The electric network in these areas is characterised by radial distribution systems. These networks are typically considered as weaker networks because of higher resistance to reactance ratio [10]. Depending on the location, utilities might be limited to weak connection points on the distribution network. The network service provider will not approve the installation of a PV power plant that causes abnormal operating conditions, thus utilities will be restricted to smaller PV installations. How a BESS can be used and sized to assist with the integration of larger PV installations on a weak network is investigated. The higher income from larger installations provides an incentive for the installation of a BESS. It is also investigated how the cost of the BESS compares to the PV installation. The problem will be approached with the following objectives in mind:

- To create a weak network model with a connected PV power plant.
- To simulate sudden power loss conditions.
- To develop a solution consisting of a BESS capable of ensuring grid compliance during a sudden power loss.
- To analyse how the solution affects the total system cost.

For weak network strengthening, the focus is on the active power support from the BESS during an extreme power loss condition. Thus, reactive power support is not in the scope of this thesis. The dynamic stability of the network is also not in the scope of this study, thus dynamic load and power are not considered. Instead the worst case scenario is studied in which maximum voltage drop occurs when a sudden power loss occurs during

a maximum loading condition. The frequency stability of the electric network is also not in the scope of this work. It is not in the scope of this thesis to do a detailed financial breakdown of the costs involved but rather to do an assessment of the basic levelised cost of energy of each subsystem.

1.2.3 Sizing a BESS for Peak Load Shaving

The network service provider (NSP) identifies developed neighbourhoods with peaking distribution feeders. A decision has to be made between upgrading the feeder or applying an alternative such as BESS support. It is very costly to upgrade a distribution feeder especially if no expansion is going to occur in the neighbourhood. In literature, BESSs are typically suggested and applied for peak load shaving [6, 11–13].

The BESSs for peak load shaving are typically sized using the worst case scenarios [13, 14]. This is the best sizing strategy to ensure that feeder specifications are not exceeded; however, it is not necessarily optimal. Assuming that the feeder can operate near or over its rated specifications from time to time, more optimal sizing strategies can be developed. By identifying the outlier cases and excluding them from the sizing strategy, one can provide optimised BESS specifications. How the current sizing strategy can be improved by identifying and removing anomalous power usage cases is investigated. How the new sizing strategy influences the costs of the system is also investigated. The objectives chosen to address the problem are as follows:

- To investigate a method with which outlier data can be identified.
- To develop an optimised BESS sizing strategy of the worst case approach using the investigated method.
- To compare the results from the original sizing strategy to that of the optimised strategy.
- To analyse the cost improvement(if any).

The focus is on providing a more optimised sizing strategy for the BESS. It is not in the scope of this thesis to compare various statistical methods for identifying outlier data points but rather to choose a relevant method, apply it and compare it to the common sizing strategy. It is also not in the scope of this thesis to do a detailed financial breakdown of the costs involved.

1.3 Thesis Overview

1.3.1 Chapter 2: Battery Fundamentals and Modelling

Firstly, battery fundamentals and common battery types are researched. Which ancillary services is relevant to this research is also investigated. This is followed by an investigation into battery modelling and the common modelling types. One model is selected and implemented in Python. A model calibration tool is also developed and the battery model is calibrated for two battery chemistries.

1.3.2 Chapter 3: Photovoltaic Systems

A brief summary of the PV system involved in this thesis is given. The fundamentals of photovoltaics are discussed as well as how their output power is influenced.

1.3.3 Chapter 4: Fluctuation Mitigation of Intermittent PV Generation

Various fluctuation mitigation methods are investigated for the purpose of smoothing the PV power output. One of the methods are chosen and implemented in Python. How the degree of damping influences the PV output as well as the BESS performance and sizing are investigated.

1.3.4 Chapter 5: Network Strengthening

How PV can be integrated into a weak network using a BESS is investigated. Firstly, how networks are modelled and how they are characterised are investigated. When networks are characterised as weak is also investigated. To integrate PV into a weak network, the power plant needs to be grid compliant. The renewable energy grid codes of the network are studied and outlined. A weak network model is created to simulate the problem and to assess the network restrictions. A solution is developed where a BESS operates in conjunction with an on-load tap changing transformer to ensure stable operating conditions.

1.3.5 Chapter 6: Peak Load Shaving

The worst case scenario sizing strategy is investigated and discussed. A statistical tool for identifying outliers is chosen. This is followed by the optimised sizing strategy that implements the statistical tool. How PV impacts the required specifications of then BESS is also investigated. The results are discussed and then conclusion are drawn.

1.3.6 Chapter 7: Cost Analysis

In this chapter cost analyses are done on the problems discussed in Chapters 3 to 5. Firstly, how the levelised cost of energy is determined for each of the systems involved is discussed. This is followed by discussion of the cost data that is used and how the missing data is estimated. How these solutions affect the cost of the systems and the cost of energy production are discussed and illustrated.

1.3.7 Chapter 8: Conclusion and Recommendations

The final conclusions to each of the problems are given and recommendations where appropriate are made.

Chapter 2

Battery Fundamentals and Modelling

A battery is a device which converts chemical energy into electric energy by means of an electrochemical reaction. It allows energy to be stored for later use for example in uninterrupted power supplies (UPS), car ignitions and flashlights. The use of the term "battery" to describe a grouping of electrical devices dates back to 1748 when Benjamin Franklin described an array of charged glass plates (Leyden jars) as a battery [15]. An Italian, Alessandro Volta, built the first electrochemical battery in 1800 [16]. In this thesis, batteries are considered to solve certain problems such as the intermittent nature of photovoltaics (PV), larger PV installations on a weak network and peak load shaving of overloaded distribution feeders.

The problem with selecting batteries, especially with there being a range of similar battery chemistries, is whether or not the battery is sufficient for its purpose and if it is performing well enough under its operating conditions. Modelling a battery can provide a means of estimating the battery's performance. Modelling entails the representation of a battery in a mathematical form; however this can be a difficult process when high accuracy is required.

Different battery modelling methods need to be investigated to identify a simple method, which is more generic, but still gives relevant performance estimations. To ease the process of estimating battery performance, the battery model must be simple enough to apply to other battery chemistries without difficult experimental procedures.

In this chapter, a general overview is given of batteries and the common battery types that exist. Whether or not batteries can be considered for some of ESKOM's ancillary services is investigated. The different methods of modelling a battery are also investigated and one method is chosen to serve as the ageing model for the battery. The method is explained and implemented as a tool with which battery performance can be measured. The chapter is concluded with a discussion of advantages and concerns with regards to the battery ageing model.

2.1 Batteries

A battery is, by definition, a container consisting of one or more cells in which chemical energy is converted into electricity and used as a source of power. In Figure 2.1, it can be seen that these cells contain two electrodes (an anode and a cathode), which during a reduction-oxidation reaction (discharging), cause the electrons to migrate through an electrolyte via the flow of anions and cations. When a load is connected, electrons flow

from the anode (oxidation), through the load, to the cathode (reduction). When the battery recharges, the electrochemical reaction is reversed by means of ionisation of the electrolyte. [17]

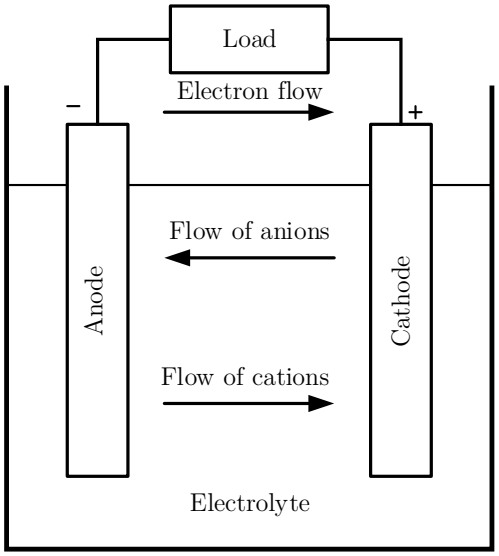

Figure 2.1: Electrochemical operation of a discharging cell. [18]

There are many different types of batteries of which a few are discussed in Section 2.2. Batteries are typically used for short- and long term storage, but can also be used for power conditioning. Ideal characteristics expected from a battery include a long calendar life, low self-discharge, long duty cycle, high charge storage efficiency, low cost and low maintenance. [19].

2.1.1 Classification of Batteries

Electrochemical batteries can be divided into two categories: primary (non-rechargeable) and secondary (rechargeable) batteries.

2.1.1.1 Primary Batteries

A primary battery is defined by its inability to be easily or effectively recharged electrically. The battery is essentially discharged and discarded. A primary cell is called a "dry cell" when an absorbent or separator material is used to contain its electrolyte. [18]

Primary batteries are characterised by their good calender life, high energy density at low to moderate discharge rates, ease of use and low, if any, maintenance. These batteries are typically used in portable devices such as flashlights, cameras and toys where a lightweight source of energy is required. [18]

2.1.1.2 Secondary Batteries

Secondary batteries are also known as "storage batteries" or "accumulators" because they have the ability to be recharged, after being discharged, to their original state.

Secondary battery applications can be divided into two categories [18]:

1. The application where the battery is used as an energy storage device; delivering its energy to the load on demand while generally being connected to a primary energy source for charging. Examples of this application include UPS, hybrid-electric vehicles and utility scale load levelling energy storage systems.

2. The application where the battery is discharged like a primary battery but recharged after use. Examples of this application include portable consumer electronics such as mobile phones, laptop computers, cameras, power tools etc. Electric vehicles can also fall in this category.

Characteristics of secondary batteries include high power density (usually lower than primary batteries), good low-temperature performance, high discharge rates and flat discharge curves. Secondary batteries have poorer charge retention but the lost charge can be restored by recharging. [18] Secondary batteries are considered in this thesis.

2.1.2 Battery Terminology

The battery field also has its own terminology. Below is a list of terms that will be encountered throughout this thesis. [18, 20]

- **Power rating -** refers to the maximum rate at which a battery can charge or discharge. This is measured in amperes (A).
- **Battery capacity -** refers to the maximum amount of energy that can be discharged from a battery without the voltage dropping below a certain specified value unique to the chosen battery type.
- **C-rate -** The c-rate is a measure of the rate at which a battery is charged or discharged. A c-rate of 1C is also known as the one-hour discharge of a battery. In other words, the rate at which a battery discharges in one hour.
- **Depth-of-discharge (DOD) -** a measure, in percentage (%), of how far a battery is discharged. A DOD of no lower than 25% is considered shallow cycling whilst a DOD up to 80% is considered deep cycling.
- **Memory effect -** refers to the gradual loss in maximum battery energy capacity owing to the same repeated partial discharge and recharge cycle.
- **Coulomb efficiency -** refers to the efficiency with which electrochemical reaction transfers energy within a particular system.

2.2 Common Battery Types

2.2.1 Lithium

A lithium battery has a positive electrode (e.g. aluminium with an active material $LiCoO_2$) and a negative electrode (e.g. copper with a carbonaceous material such as graphite) between which ions move to produce a flowing current [21]. There are a range of different lithium chemistries available and some of the popular ones are listed in Table 2.1.

Table 2.1: Lithium chemistries and properties. [18, 22, 23]

Formula	Energy density($Wh.kg^{-1}$)	Relative cycle life
$LiCoO_2$	170 to 185	1000
$LiCo_{1/3}Ni_{1/3}Mn_{1/3}O_2$	155 to 185	3000
$LiNi_{0.8}Co_{0.15}Al_{0.05}O_2$	145 to 165	3000
$LiFePO_4$	100 to 140	>4000
$LiMn_2O_4$	90 to 120	1000

Lithium batteries are known to perform well in terms of Coulomb efficiency. Their advantages include high energy-to-weight ratios, low self-discharge, no memory effect, superior calender life and high specific energy of up to 870 W·h/kg [18, 24]. A disadvantage is the required use of safety circuits which act as battery management systems. These safety circuits protect the battery against over- and under-voltage, over-heating and over-current [24].

Although these batteries have become more affordable, another important disadvantage of the lithium battery is the higher price of the technology. With lithium being a limited resource, this high price may continue to be a problem due to the growing electric vehicle (EV) and hybrid electric vehicle (HEV) industry [25, 26].

Lithium batteries are mainly used in portable devices such as cameras, mobile phones, portable tools and laptops. In the last decade, these batteries are being widely used in EV and HEV applications [25].

2.2.2 Sodium-sulphur

Sodium sulphur (NaS) batteries consist of a positive and a negative electrode using molten sulphur and molten sodium, respectively. Solid beta alumina ceramic electrolyte separates the two electrodes; allowing only the positive sodium ions to go through [24].

NaS advantages include high power and energy density, temperature stability, long cycle life, low cost, high Coulomb efficiency and good safety. Disadvantages include the risk of the high operating temperatures of this battery (300°C - 360°C) and the need to heat the battery externally for optimal performance. [24, 27]

The low cost of NaS batteries is the results of the great availability of the low-cost material required to produce these batteries. This makes this type of battery suitable for mass production. Furthermore, these batteries can easily be scaled to the megawatt range for use in utilities [27–29].

2.2.3 Lead-acid

The lead-acid (Pb-acid) battery is one of the most common and well-known battery technologies. The battery consists of a positive and a negative electrode with lead dioxide and spongy lead as the respective active materials [24]. Diluted sulphuric acid is used as the electrolyte. Lead-acid batteries are made with a variety of plate type choices: pure lead or lead with added calcium and/or antimony. Pure lead is soft and should be handled carefully, but provides low self-discharge and a long life expectancy. Adding

calcium provides a stronger plate with cheaper initial cost, but it is not suitable for repeated deep discharging. Antimony is added to create a stronger plate with less contact resistance and even cheaper initial costs. Antimony-added plates; however, have shorter lives, higher self-discharge and degrade rapidly with deep discharges. [19]

There are two main types of lead-acid batteries: valve-regulated lead-acid (VRLA) and flooded electrolyte. VRLA or sealed lead-acid (SLA) batteries allow for the evolution of excess hydrogen gas. They use catalytic converters to convert much of the hydrogen and oxygen back to water. Only when excessive pressure builds up in the battery is the gas vented. These batteries require more advanced charging control, but require less maintenance. Flooded electrolyte or 'open' batteries use an excess of electrolyte. The electrolyte needs to be replaced regularly because gassing is used to reduce electrolyte stratification. The charging regime for this battery is less strict. [19]

Advantages of lead-acid batteries include the ability to be rugged and resistant to abuse and they are low in cost compared to competing battery types. Disadvantages include low energy density per kilogram, limited cycle life, lower charging times and water loss during overcharge which leads to increased maintenance. [24] Pb-acid batteries are used in smaller, residential scale PV systems, vehicle ignitions, uninterrupted power supply (UPS) systems and lighting.

2.2.4 Nickel-cadmium

Nickel-cadmium (NiCd) batteries are made up of a positive and a negative electrode consisting of nickel hydroxide $Ni(OH)_2$ and cadmium, respectively. They use an alkaline potassium hydroxide electrolyte. This battery is sealed and utilises a recombinant system to prevent electrolyte loss. [30]

Advantages of NiCd batteries include withstanding overcharging, full capacity discharge, robustness, low internal resistance, low maintenance and low self discharge. Disadvantages include low storage efficiency (60-70%) and low capacity increase due to low discharge rates. NiCd is also much more expensive than lead-acid and could require a full discharge to prevent the memory effect. [19]

NiCd batteries are typically used in motorised equipment, power tools, two way radios, commercial and industrial portable products, toys and medical instrumentations. [30]

2.2.5 Nickel-metal-hydride

Nickel-metal-hydride batteries (NiMH) rely on absorption and desorption of hydrogen in a metal alloy during their charge and discharge cycles. The electrolyte consists of an aqueous solution of potassium hydroxide. Most of the solution is absorbed in the electrodes and separator. [19]

When comparing NiMH to NiCd, the former is more efficient at 80-90%, has a lower maximum power and a less noticeable memory effect. However, NiMH batteries are less tolerant of the reversal of voltage polarity compared to NiCd. [19]

NiMH batteries are used where environmental factors are of extreme importance [31] because the are non-toxic and the nickel can be easily recovered. They are also used in portable devices where there is some flexibility in terms of voltage range like electric razors, pagers and cameras.

2.2.6 Flow Battery

The modern flow battery (FB) consists of two electrolyte systems where the electrolytes are simultaneously pumped through two half-cells which are separated by a membrane. The power rating of such a battery is determined by the size and number of electrodes in the cell stacks. The most advanced and developed version of this battery is the vanadium redox-flow battery (VRB) [18, 32].

One of the biggest advantages of the FB is the fact that the power rating and the energy capacity rating are independent of each other. This allows the user to customise the system to a specific requirement. Other advantages include relatively slow ageing of the battery chemicals compared to other battery types, high power and energy capacity, fast charging (cycling through a new electrolyte), long life through a simple electrolyte replacement, low temperature operations, full discharge capability and the use of non-toxic materials. Disadvantages include low efficiency when utilising less than 20% of the rated power, the requirement of equipment consisting of moving mechanical parts, system cost, low energy density and more space intensive equipment. [24, 27, 33, 34]

These batteries are used by large- and small scale-demonstration and commercial products. The FB is fitting for a larger scale of utilisation [27].

2.2.7 Battery Summary

Table 2.2: Summary of battery specifications. [18]

	Energy density Wh/L	Calendar life (years)	Cycle Life	Self-discharge %/mo (20°C)	Maintenance
Lithium	120-640	5+	1000+	2	Low
Sodium-sulphur	151	5-15	2500 to 4500	-	Low
Lead-acid	50-90	3-8	200 to 1500	2-8	Model dependant
Nickel-cadmium	15-100	3-25	500 to 2000	5-20	Model dependant
Nickel-metal-hydride	177-430	5-10	500 to 1000	15-30	Low
Flow batteries	25-75	20-30+	3000 to 10000+	None	Low

2.3 Batteries and Grid Reserves

Grid reserves are extra available energy capacity on the electrical network, whether they are generating reserves (i.e. spinning reserves or non-spinning supplemental reserves) or stored power reserves (i.e. batteries or capacitors). These reserves are expected to be

available within a short time interval for frequency or power support. South Africa's public electricity utility, ESKOM, requires power reserves as one of their ancillary services. These reserves focus on ensuring grid stability, thus this research will look into implementing a battery energy storage system (BESS) to serve the purpose of some of these reserves. The idea is to use BESSs to support the grid in general by functioning as a reserve but also to support the PV power producers by providing a more stable grid-tied power plant. ESKOM's ancillary services document specifies five different types of reserves [35].

2.3.1 Instantaneous Reserves

This type of reserve serves as generation capacity or demand side managed load. It is used to prevent excess frequency deviation and should thus be fully available within 10 seconds. Instantaneous reserves are also required to be sustained for at least 10 minutes. The generators providing this service are expected to respond to high frequencies (above 50.15 Hz) as stipulated by the South African Grid Code.

2.3.2 Regulating Reserves

This type of reserve also serves as generating capacity or demand side managed load. The difference is that it should respond within 10 seconds and be fully activated within 10 minutes. The purpose, according to [35], is to make enough capacity available in order to maintain the frequency close to the target frequency and to keep the tie line flows between control areas within schedule.

2.3.3 10-minute Reserves

This generation capacity or demand side managed load should be able to respond within 10 minutes. This can typically be a quick start generating plant such as hydro or pumped storage. The purpose of these reserves is to restore instantaneous and regulating reserves to their required levels after they have experienced an event. These reserves could be required up to 600 hours per year (this is 50 weeks per year or 4 days a week or 3 hours per day). It is also suggested that these reserves be used as emergency reserves if their costs are close to or more than that of gas turbines.

2.3.4 Supplemental Reserves

This type of reserve also serves as generating capacity or demand side managed load with the difference that it should respond within 6 hours or less. Its purpose is to restore operating reserves.

2.3.5 Emergency Reserves

These reserves should be fully available within 10 minutes and are required for about 10 minutes. This type of reserve is only used when an abnormality occurs and quick action is required. Emergency reserves are required to be under national control. Examples of these reserves are interruptible loads, emergency generator capacity and gas turbine capacity.

2.3.6 Relevant Reserves

Instantaneous and regulating reserves are relevant to this study. PV output fluctuation mitigation, network strengthening and peak load shaving strategies that assist the network are studied. Peak load shaving typically requires quick response but will most likely need to be sustained from 1 to 3 hours maximum. Fluctuation mitigation can be classified under instantaneous reserves since it requires quick response and the duration of passing cloud cover can last several minutes. Network strengthening can be a combination of instantaneous and regulating reserves since a quick response is required but the batteries can also assist in maintaining frequency.

2.4 Battery Modelling

Like humans, batteries are made up of various different parts which age and wear out. Repeated electrochemical reaction tires the electrolyte within the battery and prevents the battery from performing as before. There are a few factors that influence a battery's degradation: a deep depth of discharge (DOD), high c-rates, high and low temperatures and extreme states of charge levels [36–39]. A method is required with which one can model the degradation of the electrolyte in order to more accurately estimate the state of the battery's health. In literature, we find various derived models based on different approaches. For the purpose of this thesis, three approaches are investigated.

2.4.1 Electrochemical Models

Electrochemical models are derived from first principles which makes them more superior in many respects. They are based on the chemical reactions of charging and discharging batteries as well as the consisting chemical concentrations [40]. Due to the scientific nature of these models, they consist of technical algorithms and formulae which rely on detailed sets of specifications and parameters. These include parameters such as electrolyte concentrations and diffusion coefficients. This is proprietary information and is not commonly made available by manufacturers [41, 42]. Extensive testing, experimentation and data collection are required in order to derive the model parameters; thus, making this model expensive and time consuming [42–44]. Due to the complex nature of these models, they are more difficult to implement than their counterparts but are much more accurate. This model is also only relevant to the chemistry that it represents.

2.4.2 Equivalent Circuit Models

As the name suggests, this model consists of an equivalent circuit usually made up of capacitors and resistors [45–47]. These circuits can be set up as first-, second- or third-order resistance-capacitance models and as such their parameters need to be estimated. These are algorithm-based estimation models [46]. The layout and parameters of the circuit allow it to represent the characteristics of a battery. This makes the model attractive since it gives a better representation of the internal physical states as well as the limitations of the battery [42]. The model is also considered fairly accurate and can be used as a generic model to represent a type of battery. Like the electrochemical models, the model also requires extensive testing and experimentation in order to derive the characteristic parameters. This model is considered simpler than the electrochemical model.

2.4.3 Energy-Throughput Models

The energy-throughput (Ah-throughput) model is based on the assumption that a battery can only handle a certain amount of energy throughput in its lifetime [48]. Regardless of how the energy is drawn, once this total energy throughput is reached, the battery is considered unusable due to capacity loss. This model is based on the observation made that no matter what depth-of-discharge is used, when the number of cycles are multiplied with the discharged energy, the resulting curve is assumed flat [48, 49]. These models use pre-determined equations from literature which use more readily available data. These models usually rely on depth-of-discharge data which is made available by manufacturers. This makes the model simpler compared to the other models. The nature of this model makes it more generic but also less accurate than the previously mentioned models.

2.5 Battery Ageing Model

An energy-throughput-based ageing model is chosen for this study. The model is a control-oriented dynamic state-of-health model based on the Arrhenius equation. The Arrhenius equation is presented by Svante Arrhenius in 1889 and it gives the dependence that a chemical reaction has on the absolute temperature [50]. It is chosen for its simplicity and the fact that it is not parametrised by measured data. The model is used in [38] to monitor the battery's state-of-health (SOH) in hybrid electric vehicles and is based on a static model of Bloom *et al.* [51]. Similar variants of the model are used in [52–54].

2.5.1 State-of-Charge

The state-of-charge (SOC) is a measurement of the electrical charge of a battery. It is helpful to know the SOC in order to prevent the over- or under charging of a battery. The model in [38] calculates the SOC using the following equation:

$$SOC(t) = SOC_0 - \frac{1}{Q_0} \cdot \int_0^t Q_i(\tau) d\tau, \tag{2.1}$$

where SOC_0 and Q_0 are the initial SOC and battery capacity in Ah, respectively. $Q_i(\tau)$ represents the energy charged or discharged over time, t. The initial energy capacity of the battery changes over time as it is used. $SOC(t)$ equals one when the battery is fully charged and zero when it is completely discharged.

2.5.2 State-of-Health

The SOH is a measurement of the current battery capacity compared to its initial capacity. According to [55, 56] a battery is considered '*dead*' when it has lost 30% of its initial capacity. The authors of [38, 57] suggest that it is at the 20%-mark. For the purpose of this thesis, the 20%-mark is chosen. The SOH is determined in a similar manner to the SOC:

$$SOH(t) = SOH_0 - \frac{1}{2 \cdot N \cdot Q_0} \cdot \int_0^t |Q_i(\tau)| d\tau, \tag{2.2}$$

where SOH_0 and N are the initial SOH and number of cycles before end-of-life, respectively. It is important to note that charging and discharging are accounted for by the integration thus resulting in the number two in the denominator. The SOH equals one when the battery is capable of its initial capacity and zero when it is only capable of 80% of its initial capacity.

The rate at which the battery loses capacity is influenced by the number of cycles (N) of which the battery is capable. This number is not constant but depends on the operating conditions of the battery. Wang *et al.* [36] concludes that for the $LiFePO_4$ cell, specifically the ANR26650M1, the capacity fade is influenced by the c-rate and cell temperature. In this thesis the ANR26650M1 cell will represent lithium technologies because of its high cycle count and representation in the energy storage, HEV and RE fields [38, 58–60]. Assuming that the lumped cell temperature is kept constant with the battery management system, the only time-variable with a significant impact is the c-rate. Bloom *et al.* [51] propose a model based on a modified Arrhenius equation which estimates the percentage capacity loss $\triangle Q_0$ based on the c-rate. The equation is as follows:

$$\triangle Q_0 = B(c) \cdot \exp\left(\frac{-E_a(c)}{R \cdot T}\right) \cdot Q(c)^z. \tag{2.3}$$

In equation (2.3), c refers to the c-rate, $B(c)$ is the pre-exponential factor, $E_a(c)$ is the activation energy measure in J/mol and $Q(c)$ is the total energy throughput measured in Ah. The equations consist of three constants: the ideal gas constant (R), lumped cell temperature (T) and the power law factor (z). The values of the equation parameters will be discussed in Section 2.6. Equation (2.3) is rewritten, as shown by equation 2.4, to determine the total energy-throughput that the battery experiences in order to lose 20 % of its initial capacity. The energy-throughput changes dynamically as the operating conditions of the battery change.

$$Q(c) = \left[\frac{\triangle Q_0}{B(c) \cdot \exp\left(\frac{-E_a(c)}{R \cdot T}\right)}\right]^{1/z} \tag{2.4}$$

In equation (2.5), $Q(c)$ is divided by the initial cell capacity (Q_c) in order to determine the total number of cycles (N). It is important to note that a single cell capacity is used to represent the battery as a whole because the model parameters are experimentally determined from a single cell as shown by Wang *et al.* [36].

$$N(c) = \frac{Q(c)}{Q_c} \tag{2.5}$$

Similarly, in a study by S. McCluer [53] and R. Jaworski [52] , the lead-acid battery's SOH is determined using the original Arrhenius equation as shown by equation 2.6. In this equation; however, the c-rate does not affect the capacity loss of the battery:

$$\triangle Q = B \cdot \exp\left(\frac{-E_a}{R \cdot T}\right) \cdot Q. \tag{2.6}$$

2.6 Model Calibration

The ageing model consists of parameters which characterise the ageing process of the battery. These parameters change based on the selected battery chemistry. It is important to adjust the parameters such that an accurate representation of the battery is achieved. The parameters are calibrated using a simpler version of the final ageing tool. This is discussed in Section 2.7. Figure 2.2 is a flow diagram which describes the workings of the calibration tool.

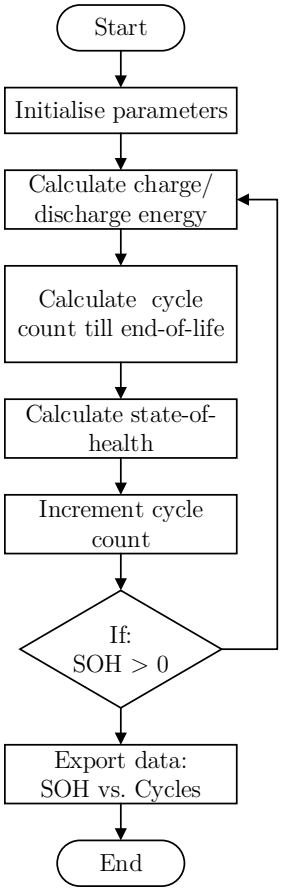

Figure 2.2: Calibration tool flow diagram.

The tool starts by initialising the testing parameters which are required to match the calibration curve with the actual experimental curve. These parameters can be examined in Table 2.3, 2.4 and 2.5. Since the tool has to simulate a battery charge and discharge at a certain DOD, the charge/discharge energy is determined by multiplying the DOD with the battery capacity. Next, the cycle count is determined using the set parameters with equations (2.3) and (2.5). Using the cycle count and charge/discharge energy, the new SOH is determined using equation (2.2) and the cycle count is incremented. This process is repeated until the SOH of the battery reaches zero which indicates that the battery has lost 20 % of its initial capacity. Once the SOH is zero, the data is exported for comparison and plotting.

The current model set-up uses two battery chemistries, lithium-ion and lead-acid. More battery chemistries can be added when their parameters are known and when their ca-

pacity fade versus cycle data is available. The lithium ($LiFePO_4$) chemistry for the ageing model is set up and calibrated using the parameters provided by Wang *et al.* [36] in Tables 2.3 and 2.4. The lead-acid ($PbSO_4$) chemistry is set up and calibrated using the parameters provided by [52, 53] and can also be found in Table 2.3.

Table 2.3: Calibrated parameters for $LiFePO_4$ and $PbSO_4$ batteries.

Parameter	Li-ion	Lead-acid
Q_c	2	1.2
E_a	$31700 - 370.3 \cdot c$	71170
B	(Table 2.4)	1515×10^8
z	0.58	-

Table 2.4: $LiFePO_4$ pre-exponential factors with respect to the c-rate.

c	0.5	2	6	10
$B(c)$	31,630	21,681	12,934	15,512

The lithium batteries are calibrated using the same conditions as stipulated by Wang *et al.* [36] whilst the lead acid batteries are calibrated using data found in a study by W. Marańda [61] of CBS Battery Co, Ltd. The testing conditions of the two battery chemistries can be examined in Table 2.5. The batteries are calibrated over different DODs to match those of the experimental data.

Table 2.5: Battery testing conditions.

Parameter	Unit	Li-ion	Lead-acid
DOD	[%]	10, 20, 50, 80, 90	30,50,100
T	[K]	333	298
$\triangle Q$	[%]	30	20
c	-	0.5	1

The resulting curves for the lithium battery are close to the experimental results in Figure 2.3 but require an increase in z from 0.55 to 0.58 in order to match the results. The final calibrated lithium curve can be examined in Figure 2.4. It is noted that the calibrated curves are almost identical to those of the experimental results. This indicates that the model, with the current parameters, provides a very good estimation of the performance of the lithium chemistry. Since the experimental results and the model results are both linear; a good fit is expected.

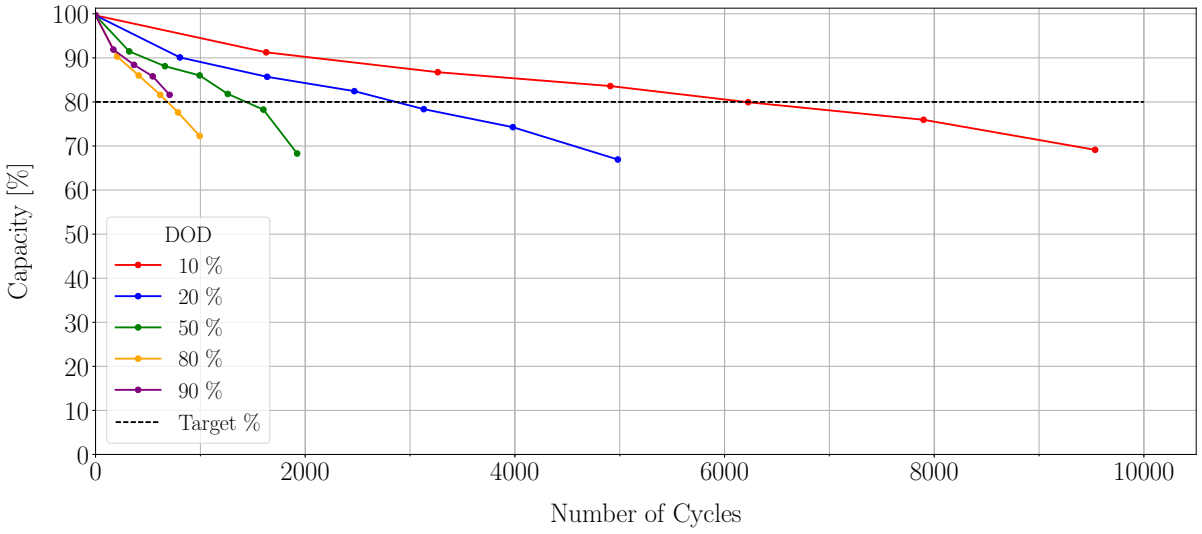

Figure 2.3: Experimental lithium cell capacity fade vs cycles [36].

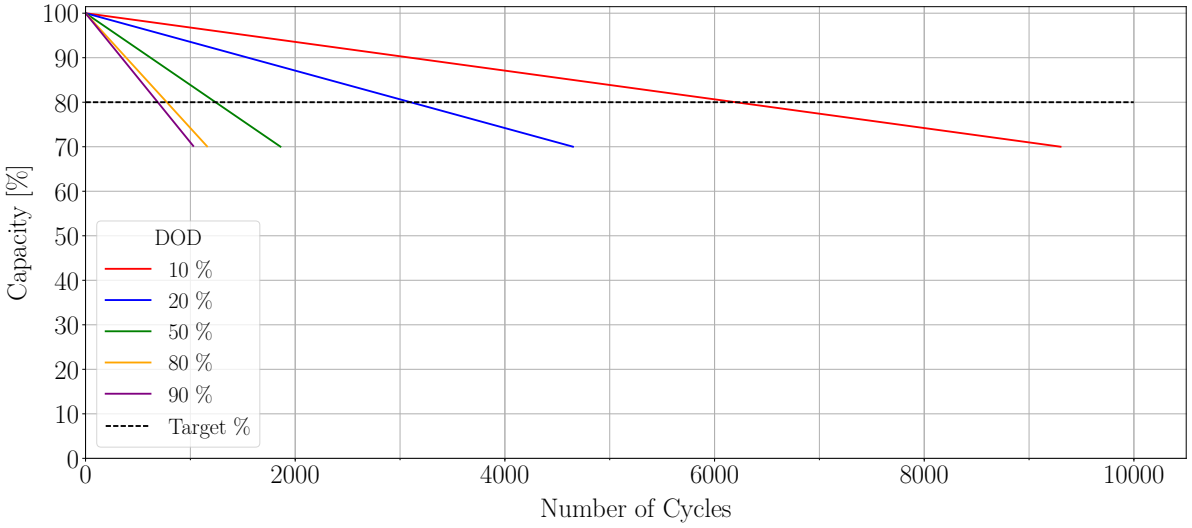

Figure 2.4: Calibrated lithium cell capacity fade versus cycles.

Since the lead-acid battery is modelled using the original Arrhenius equation, the c-rate will not have an effect on the calibration process; however, the process still charges and discharges the battery according to a specified c-rate. The original Arrhenius equation also does not use a power law factor. The lead-acid model is calibrated by adjusting the pre-exponential factor to the point where the calibrated figure is as close to the experimental figure as possible at the relevant DODs. Figure 2.5 shows the experimental capacity fade of a lead-acid cell. According to T. Reddy [18], it takes the cells of the battery from 20 to 25 cycles to achieve rated capacity; the cells then exceed the rated capacity and this then begins to fall off slowly. This is a function of the cell forming.

Due to the non-linear nature of the experimental curve, the calibrated lead-acid model lacks the accuracy of the lithium model. The calibrated curve in Figure 2.6 underestimates

the number of cycles between the 100%- and 85%-mark and overestimates between the 80%- and 60%-mark. It is noted that there is a overall underestimation at the 30% DOD-mark. For the purpose of this thesis, the ageing model is calibrated to lean more towards the lower DODs since lead-acid technologies suffer irreversible life loss during deeper depth of discharges according to T. Reddy [18]. In order for the lead-acid chemistry to remain competitive with the lithium chemistry, it will be restricted to a DOD of no less than 60 %.

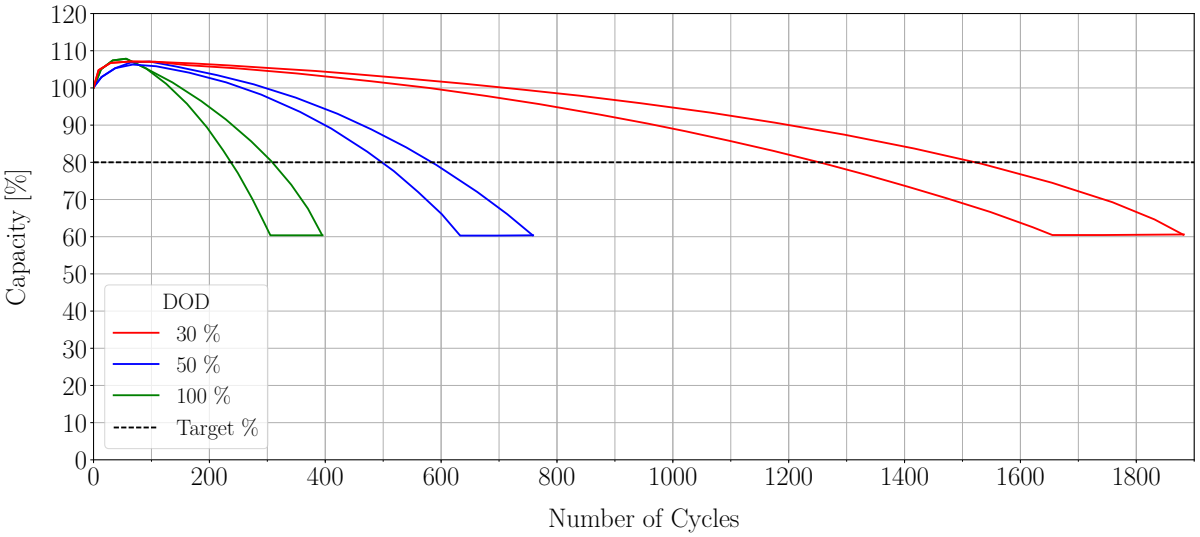

Figure 2.5: Experimental lead-acid cell capacity fade vs cycles.

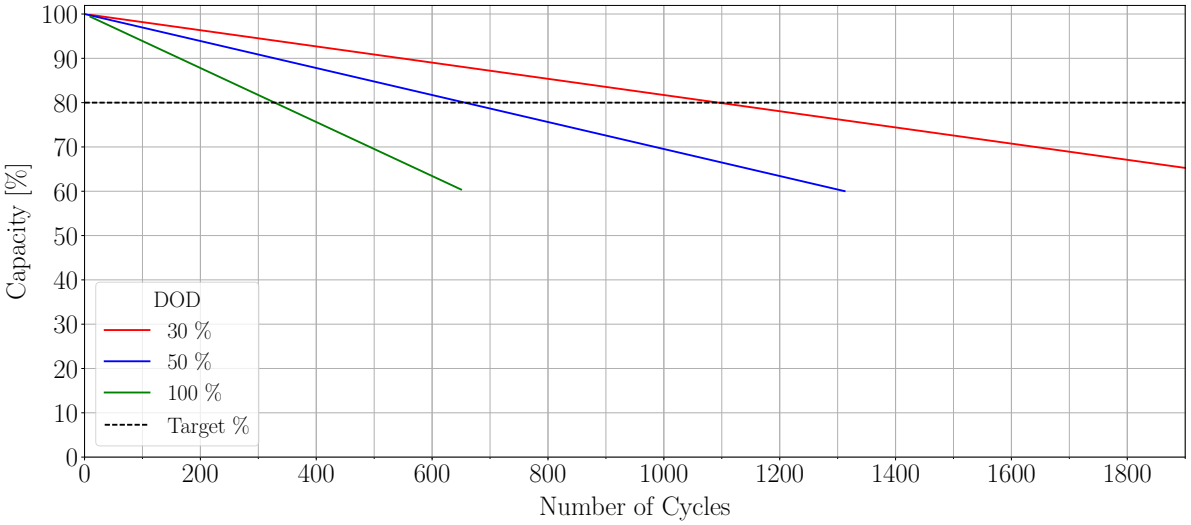

Figure 2.6: Calibrated lead-acid cell capacity fade versus cycles.

2.7 Battery Ageing Tool

The final battery ageing tool is implemented as a Python script which provides the user with a convenient way to analyse battery ageing. This is done by simply selecting the required battery and providing the energy-throughput data. Figure 2.7 shows the sequence that the tool follows.

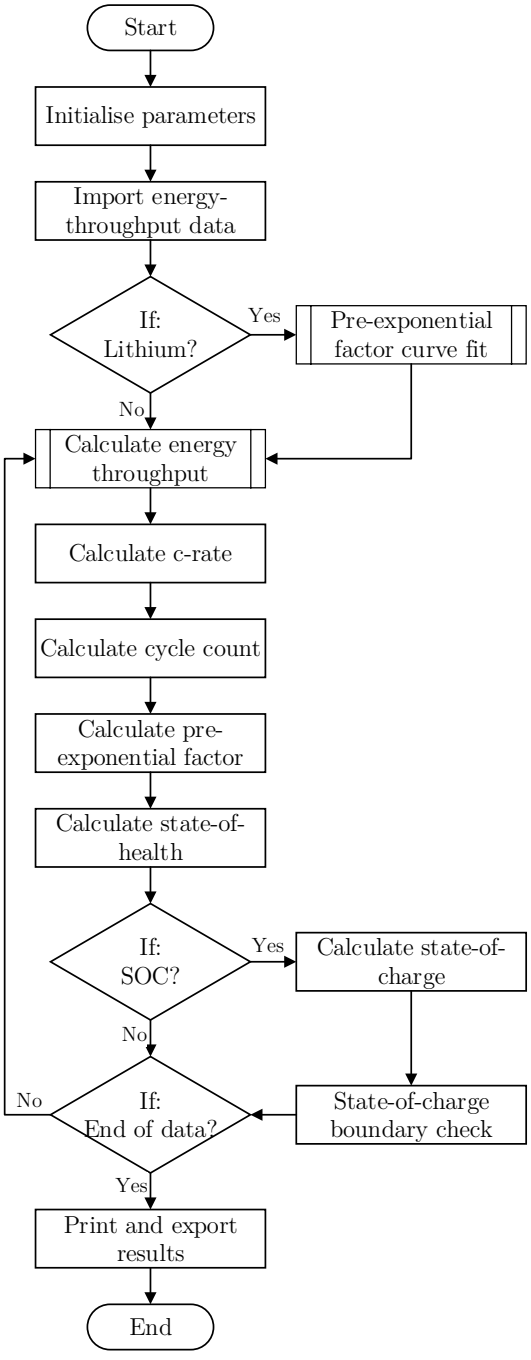

Figure 2.7: Battery ageing tool flow diagram.

The tool starts by initialising the parameters required to analyse the capacity loss. The parameters are kept the same as those of the calibration tool in Section 2.6 with a few alterations. The c-rate is no longer set but is now determined from the input data. The

time-step size of the input data also needs to be specified. The next step in the sequence is to import the input data. The model accepts data in the format as shown by Table 2.6.

Table 2.6: Input data format.

Time-step	Ampere
0001	3
0002	5
...	...

The lithium battery model uses pre-exponential factor data which range over different c-rates. Once the tool confirms that a specific lithium battery is used, it imports the pre-exponential factor data and fits a polynomial equation to it. This curve fit can be examined in Figure 2.8. This allows the model to choose the appropriate factor for a certain c-rate. The tool uses a fixed pre-exponential factor when using the lead-acid battery. The lithium chemistry used in this thesis has different pre-exponential factors over a certain c-rate range; however, this is not the case for every chemistry. It depends on the available information and whether or not experiments have been done to determine more accurate pre-exponential factors. Otherwise, the user has to determine a factor based on the calibration process.

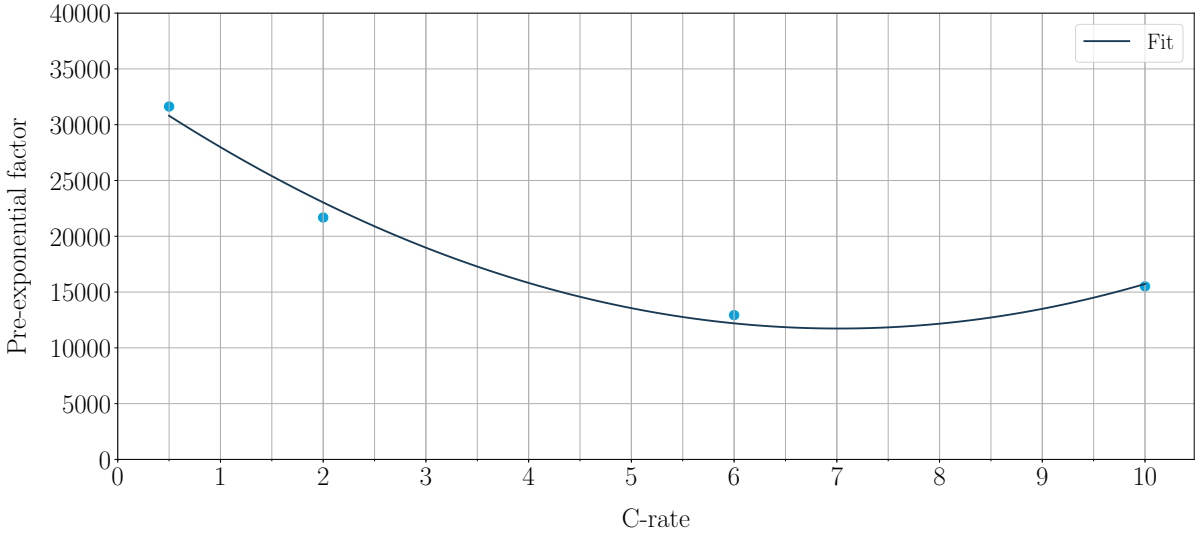

Figure 2.8: Pre-exponential factor curve fit.

The tool starts to iterate over the data by, firstly, calculating the energy throughput between two data points. Once, this has been completed, the average c-rate of the time-step is calculated. The c-rate is then used to calculate the pre-exponential factor. A warning is presented when the c-rate is larger than ten. This is because inaccuracies might have occurred as there is only a limited range to the available pre-exponential factor data. The next step is to calculate the cycle count from equation (2.3) and (2.5). With the cycle count known, the SOH calculation follows using equation (2.2). These

steps are repeated for all the data points and then one can examine how the battery SOH reduces over time.

The SOC is not required for the purpose of this model but is included in the tool to serve as a check to ensure that the battery capacity is not exceeded. This option can be enabled if needed. After the SOC-check, the tool does a check to see if it has processed all the data. Once all the data is processed, the results are displayed to the user in the form of an percentage. However, the user also has the option to export the SOH loss profile for further analysis. Figure 2.9 illustrates the curves of three SOH loss profiles. These curves represent different energy-throughput profiles through the same capacity battery for the period of a year. This can prove quite useful in identifying when excessive battery usage occurs or when the battery is abused the most.

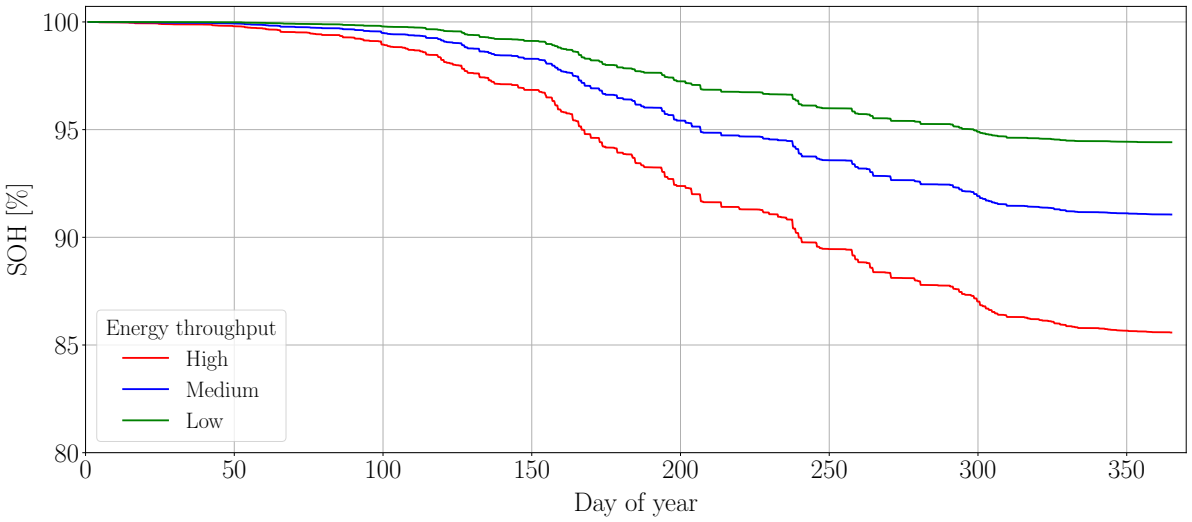

Figure 2.9: Examples of SOH profiles.

2.8 Conclusion

In this chapter, battery fundamentals are discussed as well as the possible ancillary services they can provide for the network's service provider, ESKOM. Various battery modelling methods are investigated and an energy-throughput model is selected to be implemented as a tool to measure battery performance. The model is an energy-throughput-based capacity fade model and it is applied to a lithium ($LiFePO_4$) chemistry and a lead-acid ($PbSO_4$) chemistry. More chemistries can be added if the relevant parameters are known.

The ageing model is implemented as a tool in the form of a Python script. The tool makes it simple to test how a battery performs based on an energy-throughput profile. The tool imports the profile and calculates how its SOH is influenced based on the operating conditions specified by the user. It provides useful SOH profiles which allows the user to assess the battery performance during the course of its use.

Users can add more battery chemistries to the model but it can be difficult to calibrate for them; thus, another tool is developed, similar to the ageing model, to help calibrate for new chemistries. The user has to provide the tool with more readily available parameters and calibrate for the rest. The ageing model is calibrated by matching the manufacturer's

resulting profile to the plot produced by the calibration tool. The user repeatedly adjusts the parameters until a satisfactory fit is found.

The selected ageing model provides a more generic model for which is easier to calibrate when compared to other ageing models such as the equivalent circuit model or the electrochemical model. However, this type of model does trade accuracy for convenience; thus it should only be used as an estimation of a battery's performance.

A study based on the selected model provides detailed parameters for the calibration of the lithium chemistry which results in a very accurate representation. The studies on the lead-acid chemistry do not provide detailed parameters and there are calibrated using the tool. Based on how the model functions, the degradation, at a constant current, is linear. The actual degradation of lead-acid chemistry is exponential, thus the model can not provide an accurate degradation over time, but it can provide a more accurate estimation of when the calibrated SOH level will be reached.

Chapter 3

Photovoltaic Systems

The photovoltaic (PV) systems of interest for this thesis are the utility scale, grid-connected PV systems that include a battery energy storage system (BESS). The system and its various components can be examined in Figure 3.1. The PV panels deliver DC power to the power conversion unit (PCU). The PCU consists of an inverter and a maxium power point tracker (MPPT). The inverter converts direct current (DC) to alternating current (AC) while the MPPT ensures that the PVs are operating at the most efficient point on their I-V curves.

The BESS typically consists of batteries that are paired with a smart controller to manage the charge and discharge of the batteries. The BESS supplies energy as required by the specific situation. These situations typically include: the conditioning of the PV power output, supplementary or emergency power and uninterrupted power supply (UPS).

In this chapter, the fundamentals regarding PV are discussed as well as what affects the PV power output.

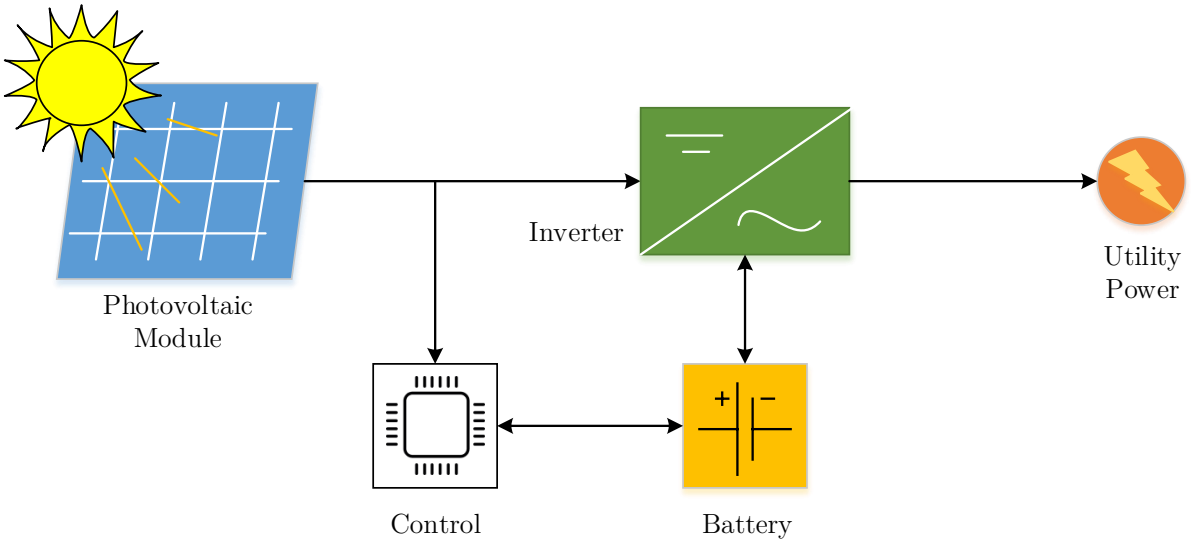

Figure 3.1: System schematic representation.

3.1 Photovoltaics

Light can be seen as discrete packets of energy called photons. When a device or material is capable of converting this photon energy into an electric voltage and current, it is called a *photovoltaic*. If the wavelength of the photon is short enough and its energy high enough, it can cause an electron in the material to break free. These electrons, which break free, can emerge as electric current if they are swept away to a metallic contact by the presence of a nearby electric field. The sun acts as the driving force to power photovoltaics. [20]

3.1.1 Basic Semiconductor Physics

Photovoltaics make use of semiconductor materials in order to convert sunlight into electricity. This type of technology is closely related to transistors, diodes and other semiconductor devices used in solid-state technologies. Pure crystalline silicon is a Group IV element found in the fourth column of the periodic table. It serves as the starting point to nearly all semiconductors. Germanium is another popular Group IV element used as semiconductor for some electronics. Most electronic device, including PV, use silicon with added boron and phosphorous from Group III and IV, respectively. Other variants PV devices can also be made: Gallium and arsenic are used to make GaAs solar cells, copper, indium and selenium are used to make CIS cells and cadmium and tellurium are used to make CdTe cells. [20]

The element silicon consists of 14 protons in its nucleus with 14 electrons orbiting the nucleus as seen in Figure 3.2 (a). The element is tetravalent because it has four valence electrons in the outer orbit. For electronic purposes, these valance electrons are the ones that are important; thus a common, simpler way to draw them is with just the four valence electrons as illustrated in Figure 3.2 (b). [20]

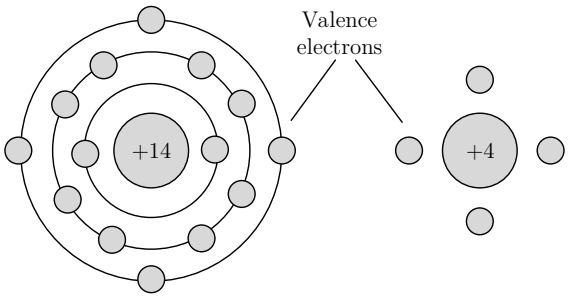

(a) Actual (b) Simplified

Figure 3.2: Representation of silicon with 14 protons and 14 electrons (a). A simplified representation of silicon with four outer electrons (b).

3.1.2 The Band-Gap Energy

Silicon is a perfect electric insulator at zero Kelvin; meaning no electrons are free to move around. When the temperature is increased, energy levels increase for the electrons allowing them to free themselves to act as current; thus the increased temperature allows for increased conductivity. Electrons have energies which fit into certain allowable energy levels or bands as illustrated in Figure 3.3. The electron in the top band, called

the conduction band, allows for the flow of electricity. As illustrated in Figure 3.3, semiconductors, at absolute zero temperature, have no electrons in the conduction band but metals have a partially filled conduction band. This is why metals are natural electric conductors. There is a gap between the different energy bands called the forbidden band. Electrons require a certain amount of energy, called band-gap energy (E_g), in order to cross the forbidden band to the conduction band. Figure 3.3 illustrates the various energy bands for semiconductors. [20]

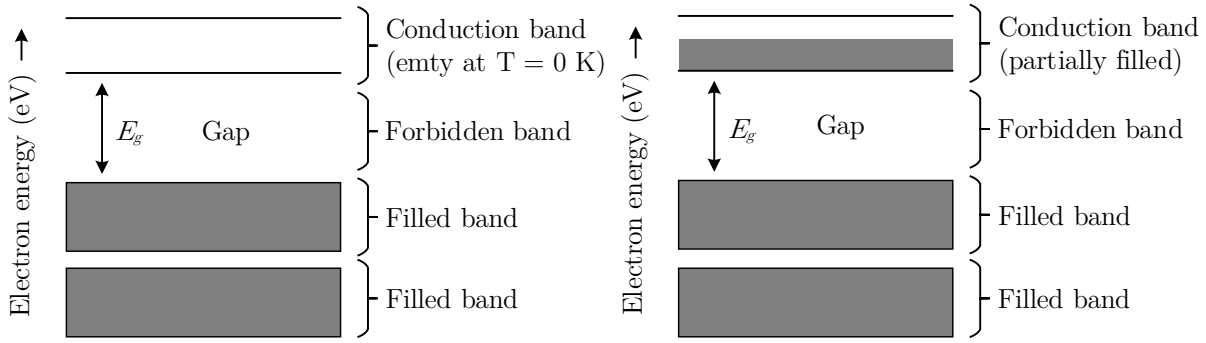

Figure 3.3: Energy bands for semiconductors. [20]

3.1.3 The p-n Junction Diode

The solar cells of a photovoltaic panel consist of p-n junctions. These p-n junctions require exposure to photons in order to create hole-electron pairs. These photons have to provide energy above the band-gap energy in order free electrons into the conduction band. An electric field is required to prevent recombination of the hole-electron pairs. Recombination is the process in which the electrons fall back into the holes. The electric field will push the electrons and holes in separate directions. Using the example of silicon, the electric field is created by establishing two regions within the crystal. This is done using pure silicon which is, on the one side, doped with a small amount of trivalent elements from Group III and doped with pentavalent elements from Group V. [20]

The pentavalent doped side has only four of its five valence electrons bound; leaving one to roam. The pentavalent elements are called the donors since they donate this roaming electron to the other side. A semiconductor doped with a Group V (donor atom) element is called an n-type material. The elements on the trivalent side are called the acceptors since they receive an electron owing to the fact that they have only three covalent bonds; leaving a positively charged hole. A semiconductor doped with a Group III element is called a p-type material. [20]

Joining a p-type and n-type semiconductor, while forming a junction between them, will cause the mobile electrons and holes to drift across the junction. When these holes and electrons cross the junctions, they leave behind immobile negative and positive charges, respectively. These immobile atoms create an electric field which counters the continued flow of electrons and holes. The process of creating immobilised charges continues until the electric field becomes so strong that all movement of the charge carriers stops. This

electric field is called the depletion region. Figure 3.4 illustrates the workings of a p-n junction. [20]

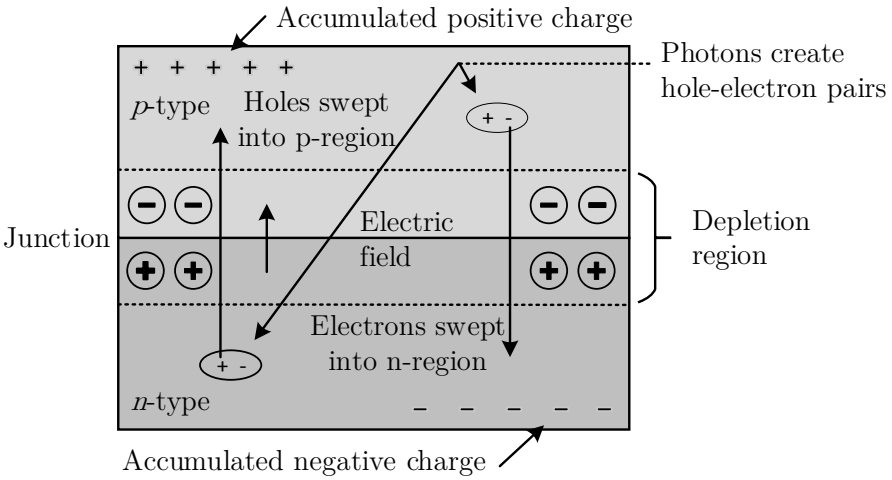

Figure 3.4: The workings of a p-n junction. [20]

3.1.4 Equivalent Circuit for PV Cells

A photovoltaic cell can be characterised by an equivalent circuit that is made up of discrete idealised components as a way to help predict the behaviour of the individual solar cells. Figure 3.5 illustrates a simple equivalent circuit of a PV cell. The circuit consists of a current source in parallel with a real diode. The current (I_L) represents the light-generated current in the cell while I_D represents the voltage-dependant current that is lost due to recombination. V_{OC} represents the open-circuit voltage. [20]

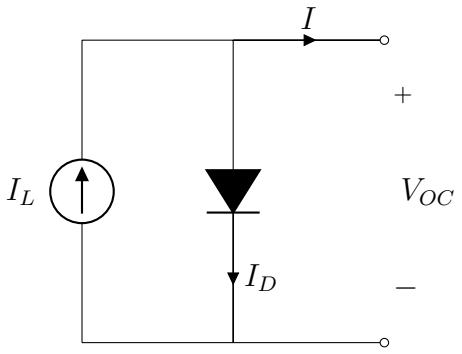

Figure 3.5: Simple solar cell equivalent circuit.

Shorting the leads of the equivalent circuit for a PV cell causes no current to flow through the diode since voltage across the diode equals zero. However, all the current flows through the the shorted leads. Thus, the short-circuit current equals the magnitude of the ideal current source itself ($I_L = I_{SC}$). According to Kirchoff's current law, the current for the equivalent circuit can be written as:

$$I = I_L - I_D = I_{SC} - I_D. \tag{3.1}$$

I_D can be substituted by the Shockley diode equation that describes a p-n junction diode as follows:

$$I = I_{SC} - I_0(e^{qV_d/kT} - 1), \tag{3.2}$$

where q and k are the electron charge ($1.602 \times 10^{-19} C$) and Boltzmann's constant ($1.381 \times 10^{-23} J/K$), respectively. V_d represents the voltage between the diode terminals measured in volts and T represents the junction temperature measured in Kelvin. Rewriting equation (3.2), the short-circuit current for the PV cell can be expressed as:

$$I_{SC} = I + I_0(e^{qV_d/kT} - 1), . \tag{3.3}$$

3.1.5 Impact of Temperature and Irradiance

The output of a PV cell can be represented by an I-V curve which can be represented by the equations of the equivalent circuit model. It is shown that the output of the cell changes when the cell temperature and irradiance change. Figure 3.6 illustrates that an increase in cell temperature can cause a considerable open-circuit voltage drop. Manufacturers will typically indicate this loss on the PV panel data sheet as a percentage deviation per unit temperature.

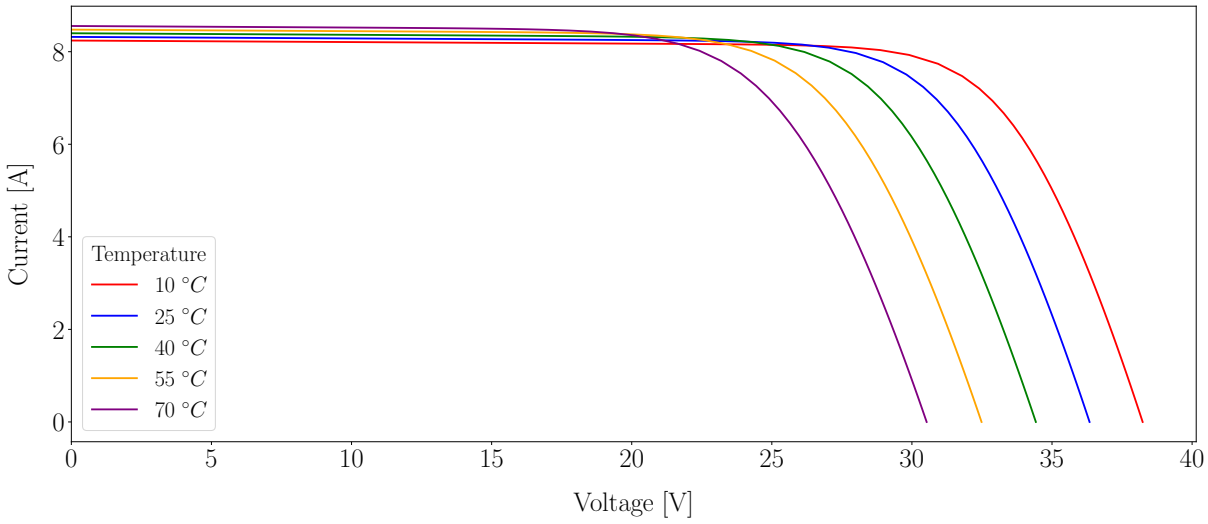

Figure 3.6: Effect of temperature on a PV cell output.

The photon energy from the sun that is converted to electrical energy by the p-n junction, is represented by a measurement called irradiance (W/m^2). The short-circuit current in equation (3.3), is directly proportional to the irradiance which means if the irradiance is reduced by one half the current will be reduced by one half, as illustrated in Figure 3.7. Manufactures typically include the figure in the PV panel data sheet to indicate the panel performance.

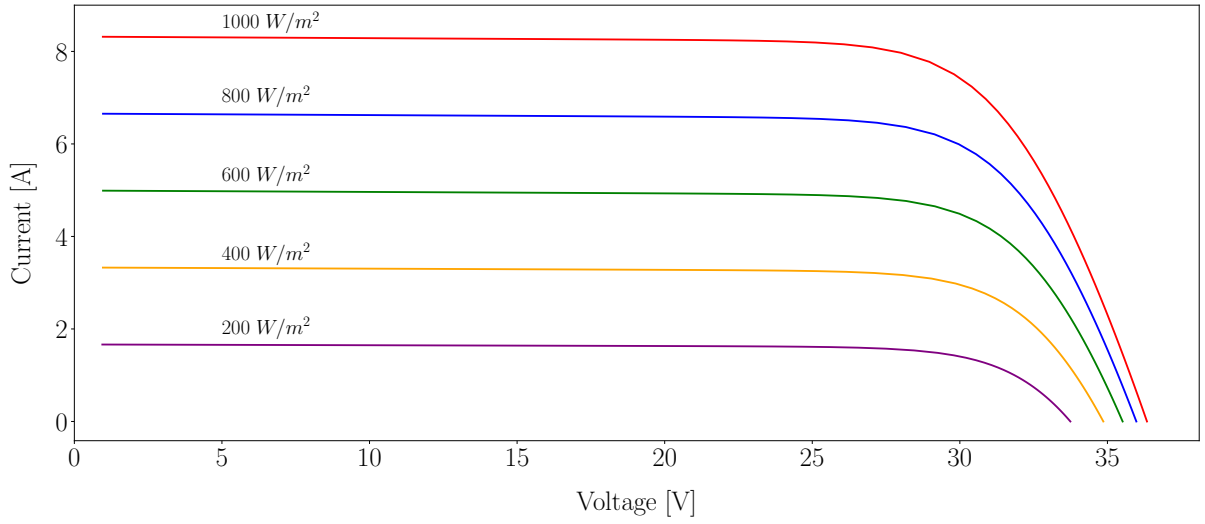

Figure 3.7: Effect of solar irradiance on PV cell output.

Chapter 4

Fluctuation Mitigation of Intermittent PV Generation

A growing solar industry can be observed in South Africa. This is mostly due to the push for the adoption of renewable energy sources and the affordability of the technology [62]. Photovoltaics (PVs) suffers from high variability with regard to its output power due to irregularities in the sun's irradiance caused by passing cloud cover. Thus the increasing penetration of grid-connected PV systems in weak radial distribution systems paired with the high ramp-rates can introduce significant voltage fluctuations [63].

The intermittent nature of the PV output power has been recorded to have a ramp-rate up to 63% of the rated capacity/minute at the La Ola PV plant [3]. One-second irradiance data collected by the National Renewable Energy Laboratory (NREL), from Oahu Island, shows how the ramp-rate of the irradiance fluctuates more than 50% between consecutive measurements [64]. Another study shows that the PV output of a system in Mesa del Sol, Mexico, fluctuates by 20% of its rated capacity/second [4].

Solutions already exist where battery energy storage systems (BESS) are used in conjunction with PV power plants to mitigate the fluctuating output power. These solutions can be divided, by their control strategy, into two categories: moving average control and ramp-rate control. The problem, however, is that the BESS sizing strategies for these fluctuation mitigation methods are unknown as well as the effect that the degree of damping has on the specifications of the BESS. An effective fluctuation mitigation strategy is required which can be implemented in the form of a tool to assist in sizing the BESS and providing a means of assessing how the degree of damping influences the sizing of the BESS.

In this chapter, control strategies for fluctuation mitigation are investigated and compared. One fluctuation mitigation strategy is selected and implemented as a tool in the form of a Python script. The tool is applied to a PV output profile to demonstrate its smoothing capabilities. The tool is also used to determine and compare the BESS requirements for certain degrees of smoothing. The battery energy-throughput profiles from the tool are used with the battery ageing model described in Chapter 2 to determine how degrees of smoothing influence the state-of-health of the battery.

4.1 Control Strategies

In literature, one typically finds two different control strategies: one being based on the moving average method and another based on the ramp-rate control strategy. In order to determine which one is relevant for a given application, it is important to understand the differences between the two control strategies.

These control strategies are typically paired with an energy storage solution to deliver or absorb energy. In [65–67], an electric double layer capacitor is used as energy storage for PV smoothing. Rahman *et al.* [68] use fuel cells to assist PV with its intermittent power output while Tam *et al.* [69] use superconducting magnetic energy storage. Battery storage is used by Hund *et al.* [70], Traube *et al.* [71] and Alam *et al.* [63] to mitigate these fluctuations.

4.1.1 Moving Average Control vs Ramp-rate Control

The moving average approach is a traditionally accepted method used to reduce PV fluctuations. [63] The strategy uses the trend of the average power output in a certain time window in order to predict the required power output for the current time-step. This makes the output dependent on the past power output which leads to a difference in the present PV output. The strategy can be examined in Figures 4.1 (a) and (b). Since the smoothing strategy is paired with an energy storage system, the difference between the PV output and the inverter output causes an unnecessary, over-utilisation of the energy storage system. The dependence on a past window of data and the length of that window can cause the output to lack the desired ramp-rate.

There are plenty of variations of the moving average control strategy. A moving average control paired with a first order low-pass filter is implemented by Ellis *et al.* [72]. An exponential moving average control is used by Samson *et al.* [73] where more weight is given to recent PV output values. Monai *et al.* [67] applied a modified Euler type moving average control. This control predicts the moving average values of a hybrid PV and energy storage system.

The ramp-rate control strategy uses monitoring systems to examine the power output profiles for high ramp-rate events. In the case of such an event, the system utilises an energy storage system to mitigate the fluctuation. An excess increase in power could either be curtailed or absorbed by the energy storage system, whereas the sudden drop in power will be countered with a sudden energy discharge [63]. The strategy can be examined in Figures 4.1 (a) and (c). According to Abdollahy *et al.* [74], the delay in the data communication system can delay the smoothing of the fluctuation and in some cases worsen it. This problem can be overcome by conditioning the power at the PV connection point using its local data.

There are also plenty of different variations of the ramp-rate control strategy.Traube *et al.* [71] use an EV battery charger in combination with a PV inverter to reduce fluctuations by means of a high-pass filter. A controller based on real-time SOC feedback with adaptive smoothing targets is used by Li *et al.* [75]. Lastly, Hill *et al.* [76], Coe *et al.* [77] and Alam *et al.* [63] use storage to assist with ramp-rate control. The control is determined by the SOC of the battery and the allowable ramp-rate droop characteristic.

In Figure 4.1, the moving average control is compared to the ramp-rate control. Both control strategies are applied to the same PV output profile. P_{INV} and P_{COMP} represent

the inverter power output and battery compensation power, respectively. In (a), how the moving average strategy has a smoother output profile while the ramp-rate approach tracks the maximum PV output better can be seen. When examining the output profile of the battery system in (b), how the batteries are continuously used for compensation can be seen. The moving average strategy, and its reliance on historical data, tends to run at an output power less than the actual PV output and uses the energy storage more often. When comparing this to (c), it can be seen that the ramp-rate approach only uses the batteries when the ramp-rate is exceeded.

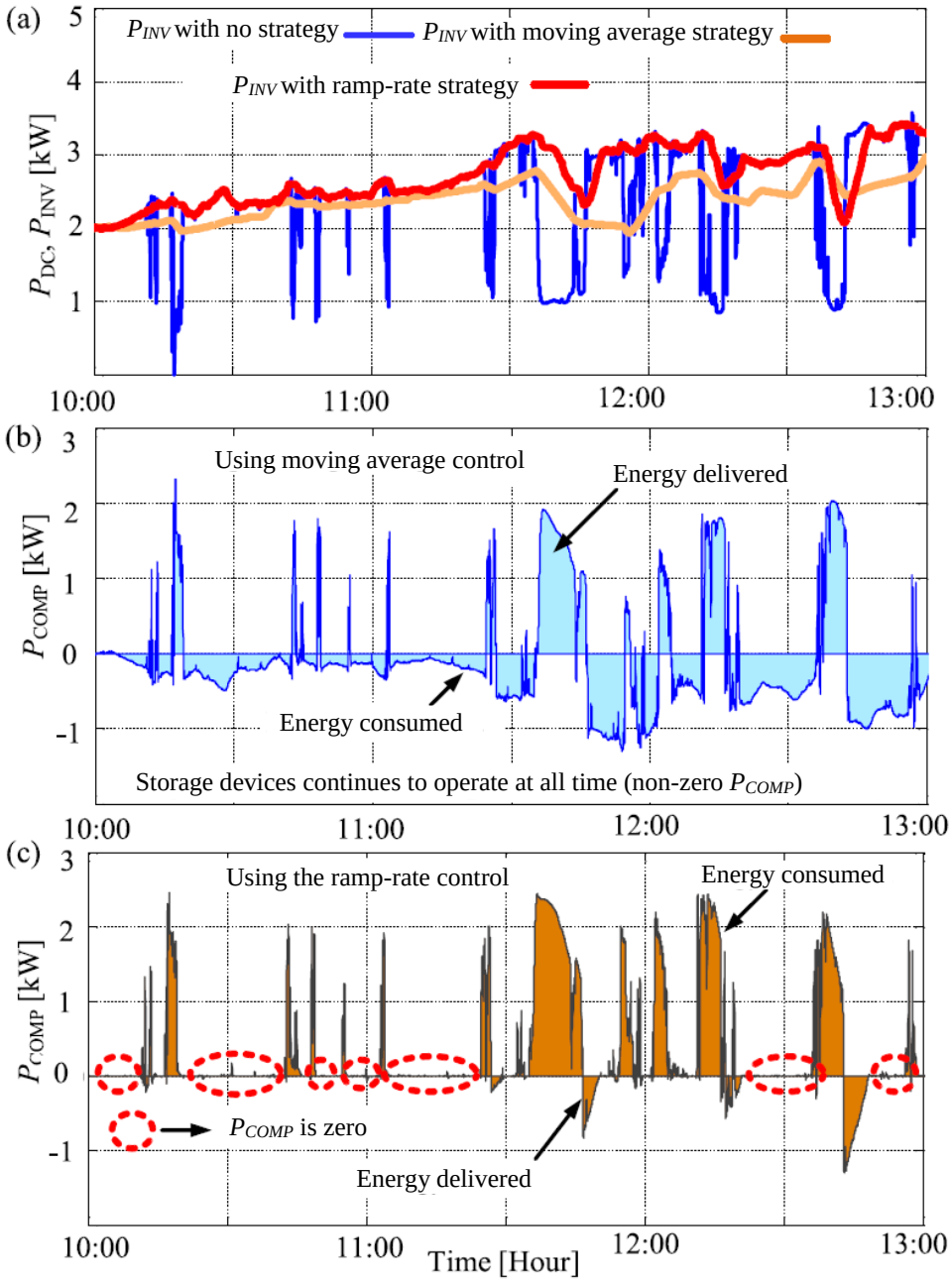

Figure 4.1: PV fluctuation mitigation methods. (a) Inverter profiles with and without fluctuation mitigation. (b) Energy storage profile for moving average strategy. (c) Energy storage profile for a ramp-rate control strategy. [63]

4.2 Ramp-rate Control

The ramp-rate control strategy in this thesis is based on a model developed by Alam *et al.* [63]. The ramp-rate control strategy is chosen over the moving average method since it minimises the use of the battery storage system. Lower energy-throughput extends battery life and ensures an economic operation of the BESS. This specific fluctuation mitigation model incorporates primary ramping and post-ramping strategy to provide an optimal balance between the degree of damping and the SOC level of the battery.

Figure 4.2 summarises the fluctuation mitigation strategy with a plot illustrating how the BESS counters the fluctuations in the PV output. The PV output power is read at a high sample rate per second. This ensures a quick reaction time during a ramping event but there is an element of lag in the system. Once a sudden drop or rise in the PV power output is detected, the BESS is instructed to discharge or absorb energy, according to the ramping stage, in order to damp the inverter output power.

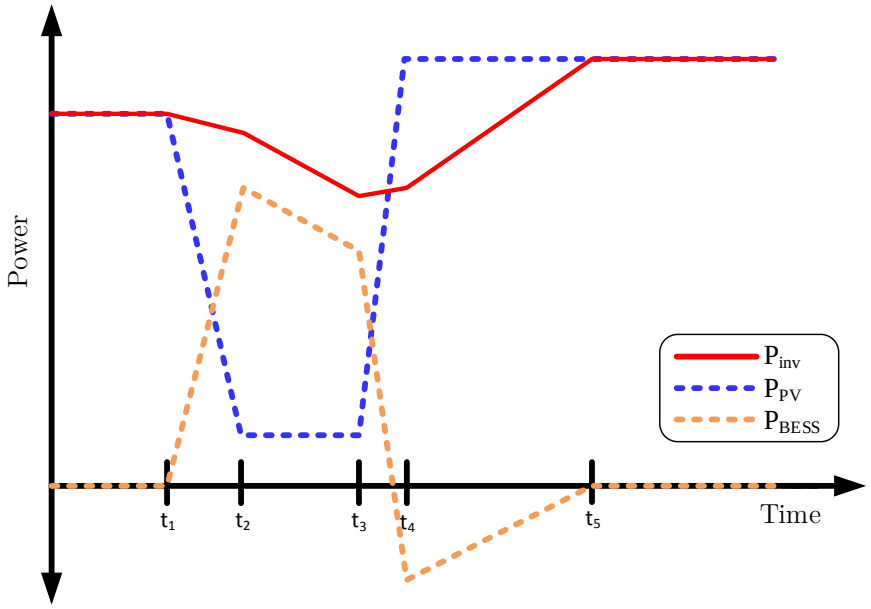

Figure 4.2: Ramp-rate strategy.

The inverter power output consists of the DC power output from the PV panels and the compensation power provided by the BESS. The inverter output can be calculated as follows:

$$P_{inv} = \eta_{inv} \times (P_{PV} + P_{BESS}) \tag{4.1}$$

where P_{inv} is the inverter output power in Watt, P_{PV} is the PV output power in Watt and P_{BESS} is the battery charge or discharge power in Watt. η_{inv} is the inverter efficiency at which the battery and PV power run.

The inverter ramp-rate can be determined by differentiating equation (4.1) with respect to time and is expressed as follows:

$$\frac{dP_{inv}}{dt} = \eta_{inv} \times \left[\frac{dP_{PV}}{dt} + \frac{dP_{BESS}}{dt}\right], \tag{4.2}$$

where ${}^{dP_{inv}}/_{dt}$ is the inverter ramp-rate in W/min, ${}^{dP_{PV}}/_{dt}$ the PV ramp-rate in W/min and ${}^{dP_{BESS}}/_{dt}$ the battery ramp-rate in W/min.

The objective of this fluctuation mitigation method is to control the power output of the inverter such that the ramp-rate stays within the specified boundaries. This is achieved by charging or discharging the energy storage system or limiting the inverter output. Rewriting equation (4.2), the charge/discharge rate of the energy storage system can be expressed by the following:

$$\frac{dP_{BESS}}{dt} = \frac{1}{\eta_{inv}} \times \left.\frac{dP_{inv}}{dt}\right|_{des} - \frac{dP_{PV}}{dt}, \tag{4.3}$$

where ${}^{dP_{inv}}/_{dt}|_{des}$ is the desired ramp-rate of the inverter output. This output value will be negative for a ramp-down event and positive for a ramp-up event. Equation (4.3) represents the basic control strategy of the inverter. For simplicity, equation (4.3) is rewritten as follows:

$$RR_{comp} = \frac{1}{\eta_{inv}} \times RR_{des} - RR_{PV}, \tag{4.4}$$

where RR_{comp} is the compensation ramp-rate from the BESS, RR_{des} is the maximum desired ramp-rate of the inverter and RR_{PV} is the PV ramp-rate. The PV ramp-rate is calculated using a discrete time representation in the following expression:

$$RR_{PV}(k) = \frac{P_{PV}(k) - P_{PV}(k-1)}{t(k) - t(k-1)}, \tag{4.5}$$

where $t(k)$ is the time at the k^{th} instant. Furthermore, the compensation ramp-rate can be used to determine the compensation power (P_{comp}) for the k^{th} instant as follows:

$$P_{comp}(k) = S \times [P_{comp}(k-1) + RR_{comp}(k) \times \{t(k) - t(k-1)\}], \tag{4.6}$$

where S is the switching function.

The desired ramp-rate of the inverter is determined by two different ramping stages. These stages include a primary ramping stage and a secondary post-ramping stage. The check for a primary or post-ramping stage is summarised by the following switching function:

$$S = \begin{cases} 1, \text{ if } |RR_{PV}| > RR_{des} \text{ (Primary)} \\ \begin{cases} 0, & \text{if } P_{comp}(k-1) < RR_{des} \\ 1, & \text{otherwise (Post)} \end{cases} \end{cases} \tag{4.7}$$

where $P_{comp}(k-1)$ refers to the compensation power, in Watts, of the previous time-step.

When the PV ramp-rate exceeds the desired inverter ramp-rate, a primary ramping stage is detected. If the PV ramp is within the limits, a check is done to determine if the previous compensation power is less than the desired ramp-rate. If this is the case, the compensation is turned off but if it is more a post-ramping event is triggered.

The desired inverter ramp-rate of a primary ramping stage is controlled by an inverse characteristic constant which provides more damping as the PV output fluctuations get higher. Adjusting the constant will adjust the degree of damping for a ramping stage [63]. The following expression shows this strategy:

$$RR_{des}(k) = \begin{cases} |RR_{PV}(k)|, & \text{if } |RR_{PV}(k)| < RR_{lim} \\ \dfrac{\gamma}{RR_{PV}(k)}, & \text{if } |RR_{PV}(k)| \geq RR_{lim}, \end{cases} \tag{4.8}$$

where RR_{lim} is the ramp-rate limit, in W/min, which determines whether or not compensation will be triggered for a given time-step and γ is the inverse characteristic constant. Figure 4.2 illustrates the inverse characteristic damping once a sudden power drop occurs.

Figure 4.3 illustrates when the primary ramping stage occurs. It can be seen that the primary ramping stage is triggered once the PV ramp-rate exceeds the ramp-rate limit. The desired ramp-rate is then determined by the inverse characteristic of the PV ramp-rate as shown in expression (4.8).

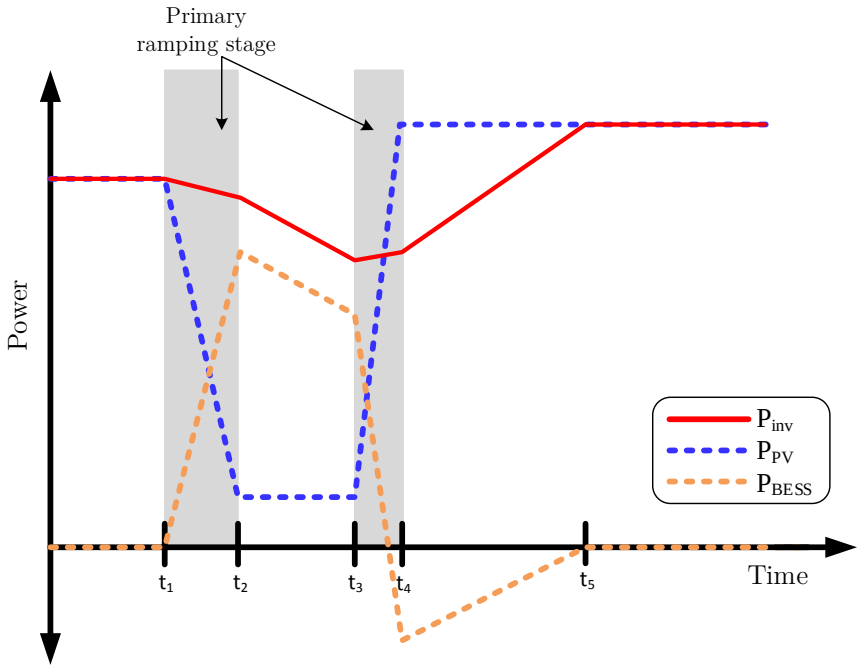

Figure 4.3: Primary ramping stage.

The post-ramping stage is triggered by the switching function in expression (4.7), when the previous compensation power ($P_{comp}(k-1)$) is not smaller than the desired ramp-rate. This means that the current PV output power level is not close enough to the inverter output level. The desired ramp-rate is determined using expression (4.9). This expression is used to check whether the current PV output is larger or smaller than the

inverter output and if the PV ramp-rate is positive or negative. This gives an indication of where the PV output power is relative to the inverter output power and is illustrated in Figure 4.4. If the PV output power and the inverter output power are both moving at positive or negative ramp-rates, the desired ramp-rate is set to zero so that the PV output can catch up to the inverter output. This is illustrated in Figures 4.4 (b) and (d). If the PV output power and inverter output power both have a different sign (meaning one is positive and the other negative), the desired ramp-rate is selected to a pre-defined adjustment ramp-rate (RR_{adj}). This is illustrated in Figure 4.4.

$$RR_{des} = \begin{cases} 0, & \text{if } P_{inv}(k) > P_{PV}(k) \textbf{ and } RR_{PV} > 0 \\ RR_{adj}(k), & \text{if } P_{inv}(k) > P_{PV}(k) \textbf{ and } RR_{PV} \leq 0 \\ RR_{adj}(k), & \text{if } P_{inv}(k) < P_{PV}(k) \textbf{ and } RR_{PV} > 0 \\ 0, & \text{if } P_{inv}(k) < P_{PV}(k) \textbf{ and } RR_{PV} \leq 0 \end{cases} \tag{4.9}$$

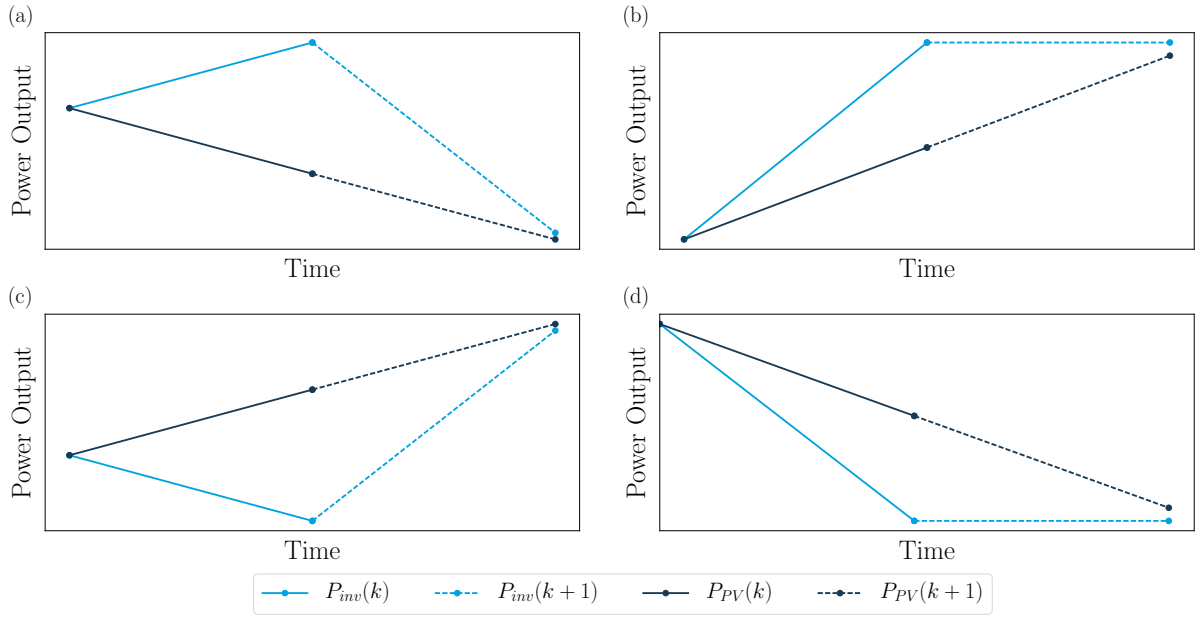

Figure 4.4: Fluctuation mitigation per case strategy.

Figure 4.5 illustrates when the post-ramping stage will occur and what it looks like in the context of a ramping event. It can be seen than that it occurs typically occurs right after a primary ramping event.

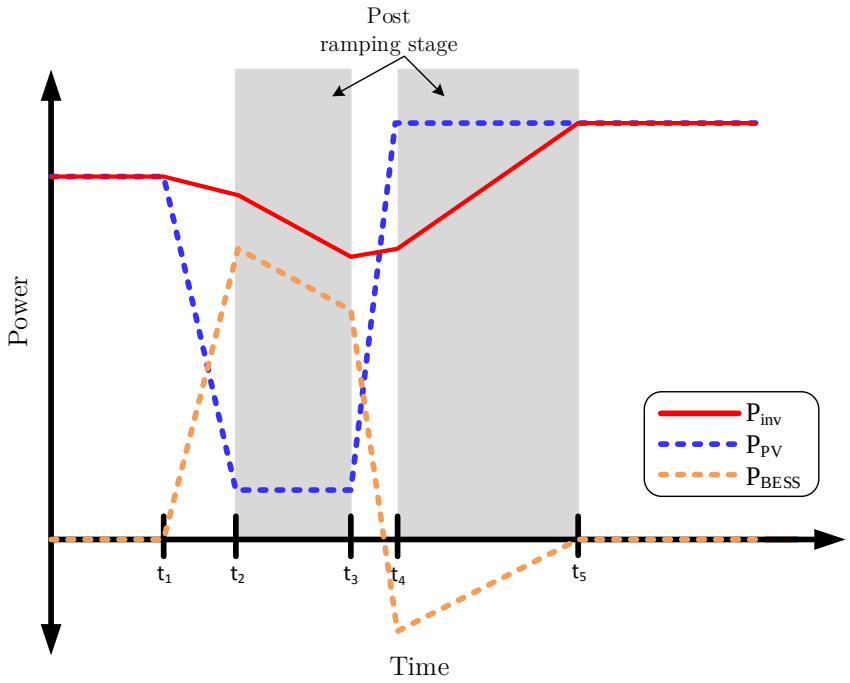

Figure 4.5: Post-ramping stage.

Once the compensation power is determined, the control does a check to determine whether or not the battery has a enough capacity for the charge or discharge action. To do this check, the battery determines an upper and a lower SOC limit which is required for the approval of a charge or discharge action. These limits are calculated using the following expressions:

$$SOC_{UL} = DOD_{max} + SOC_{buff} \tag{4.10}$$

$$SOC_{LL} = SOC_{max} + SOC_{buff} \tag{4.11}$$

where SOC_{UL} and SOC_{LL} are the SOC upper limit and SOC lower limit, respectively. DOD_{max} is the maximum DOD, SOC_{max} is the maximum SOC and SOC_{buff} is the SOC buffer. The SOC buffer is calculated using equation (2.1) as follows:

$$SOC_{buff}(k) = -\frac{1}{Q_{bat}} \cdot P_{comp}(k), \tag{4.12}$$

where Q_{bat} refers to the battery capacity in amp-hours. Because new limits are determined every time-step, with regards to the current required compensation power, the strategy ensures that the appropriate limits are set to check if a charge or discharge operation is possible. The check is done as follows:

$$Check = \begin{cases} \begin{cases} 1, & \text{if } P_{comp}(k) < 0 \textbf{ and } SOC(k-1) < SOC_{UL}(k) \\ 0, & \text{if } P_{comp}(k) < 0 \textbf{ and } SOC(k-1) \geq SOC_{UL}(k) \end{cases} \\ \begin{cases} 1, & \text{if } P_{comp}(k) \geq 0 \textbf{ and } SOC(k-1) > SOC_{LL}(k) \\ 0, & \text{if } P_{comp}(k) \geq 0 \textbf{ and } SOC(k-1) \leq SOC_{LL}(k) \end{cases} \end{cases} \tag{4.13}$$

From 4.13, an answer of one means the charge or discharge action is approved and an answer of zero means it is not approved. The limits are compared to the SOC from the previous time-step which is the latest battery SOC level.

Figure 4.6 is an example of the ramp-rate strategy applied to a PV output data set. It can be seen that the inverter output tracks the PV output until a sudden drop or rise in power occurs. The primary ramping event strategy is applied once the disturbance occurs. After the passing of the power disturbance, the post ramping event strategy is applied.

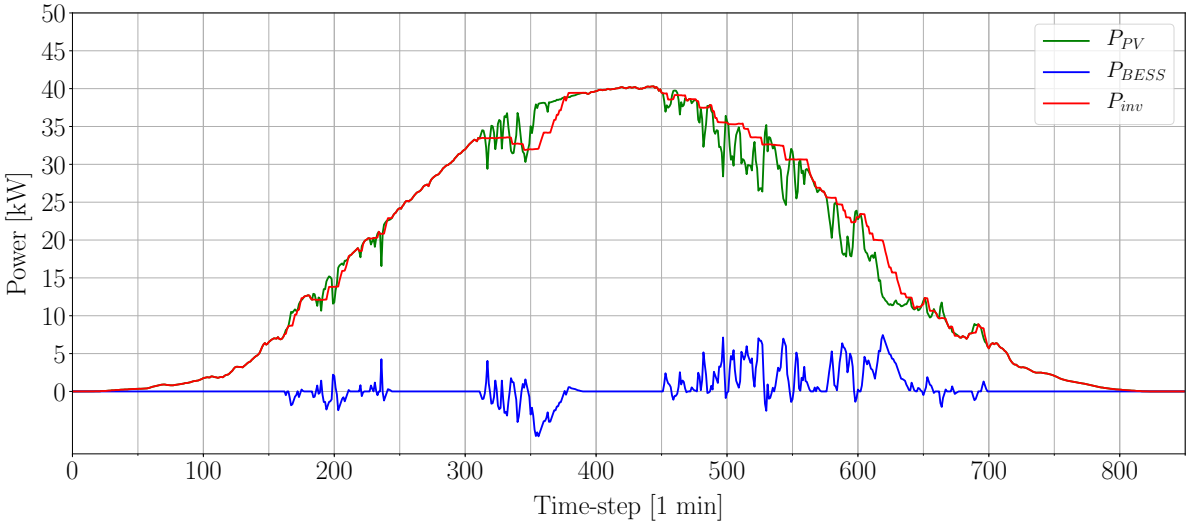

Figure 4.6: Applied ramp-rate strategy.

Figure 4.7 illustrates the output of a 50 kW PV installation on a very cloudy day. It can be seen in this figure that adjusting the RR_{adj} parameter of the model influences the damping performance. The higher degree of damping from the $RR_{adj} = 1\%/\text{min}$ causes a smoother output profile but with less tracking of the peak PV output. In this case, it reduces the resulting PV output power in exchange for a smoother output. Increasing the parameter to $4\%/\text{min}$, reduces the damping but results in better tracking of the PV output.

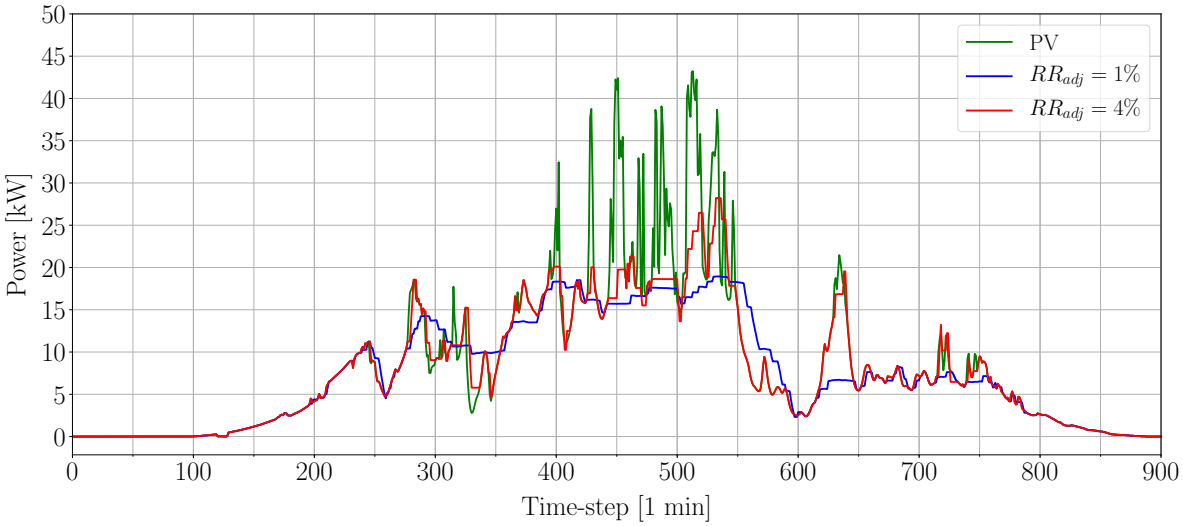

Figure 4.7: Difference in the degree of damping.

4.3 Fluctuation Mitigation Tool

The fluctuation mitigation tool is implemented in Python. Python is an object-oriented, high-level programming language, suited for rapid application development. A tool provides a great way to assess large amounts of data in an automated, time-saving way. The script is aimed at providing the resulting inverter and battery output curves. From the inverter output curve, one can determine whether or not the degree of fluctuation mitigation is sufficient when compared to the original PV output curve. The battery output curve is used to determine the specifications of the BESS and can be used in conjunction with the ageing model to determine how the fluctuation mitigation affects the SOH of the battery. The sequence of the tool is described by Figure 4.8.

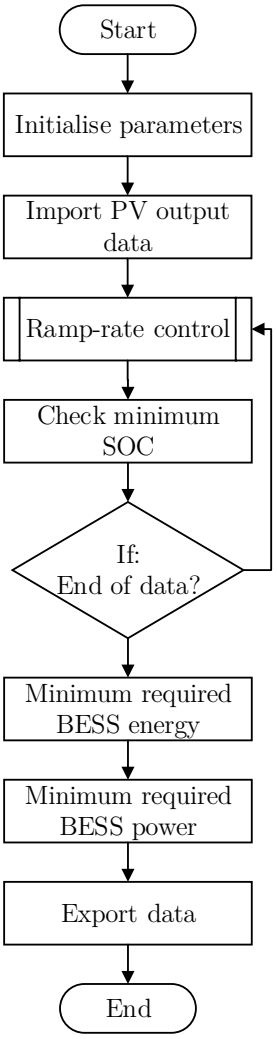

Figure 4.8: Fluctuation mitigation tool.

The tool starts by initialising the parameters as shown in Table 4.1. These are the parameters the user can set, in order to control the degree of damping, to initialise the tool. The tool can be utilised in two ways: to determine the damping capabilities of a specific battery size or to determine the inverter- and BESS output profile for a certain degree of damping. The latter requires the battery capacity (B_{cap}) to be specified and, to restrict the battery charge or discharge, the maximum c-rate (c_{max}) limit to be set . The RR_{lim} and RR_{adj} parameters are both represented as a percentage of the maximum PV output while the DOD_{max} and SOC_{max} parameters are both represented as a percentage of the maximum rated battery capacity. The inverter efficiency (η_{inv}) parameter is assumed to be a constant value based on the chosen inverter specifications. Inverters typically have a variable efficiency that depends on the inverter output power.

Table 4.1: Ramp-rate model parameters.

Parameter	Unit	Description
Q_{bat}	Ah	Battery capacity
RR_{lim}	%/min	Ramp-rate limit
RR_{adj}	%/min	Adjustment ramp-rate
DOD_{max}	%	Maximum depth-of-discharge
SOC_{max}	%	Maximum state-of-charge
η_{inv}	%	Inverter efficiency
γ	%	Inverse characteristic constant
c_{max}	-	Maximum allowed c-rate
t_{size}	s	Time-step size

Once the parameters are initialised, the power output data from a PV installation is imported. The data is required to be in the format as illustrated by Table 4.2. The time-step should be an integer value. If the difference between the time-steps is not in minutes, it must be specified to allow the tool to adjust to it. The data used in this thesis is minutely measured data and the fluctuation mitigation method is meant to be applied with a controller which takes hundreds of readings per second. Thus, the Python tool is written such that it reacts based on the next data point $(k+1)$ and as such it assumes no lag in the system.

Table 4.2: Input data format.

Time-step	Power [kW]
0001	7.5
0002	8.2
...	...

Once the data is imported, the tool steps through the data points and applies the ramp-rate strategy. Figure 4.9 illustrates the sequential flow of the ramp-rate model. It starts by calculating the PV ramp-rate of the current time step using equation (4.5). The PV ramp-rate is then used to determine the selection of the desired ramp-rate using expression (4.8). Next, a check is done to determine if the absolute value of the PV ramp-rate is larger than the desired ramp-rate. If it is larger, it indicate that a primary ramping stage should be initiated and, thus a compensation ramp-rate can be calculated. From the compensation ramp-rate, a compensation power is calculated. A check is done on the SOC of the battery to determine whether or not the BESS has enough capacity for a charge or discharge.

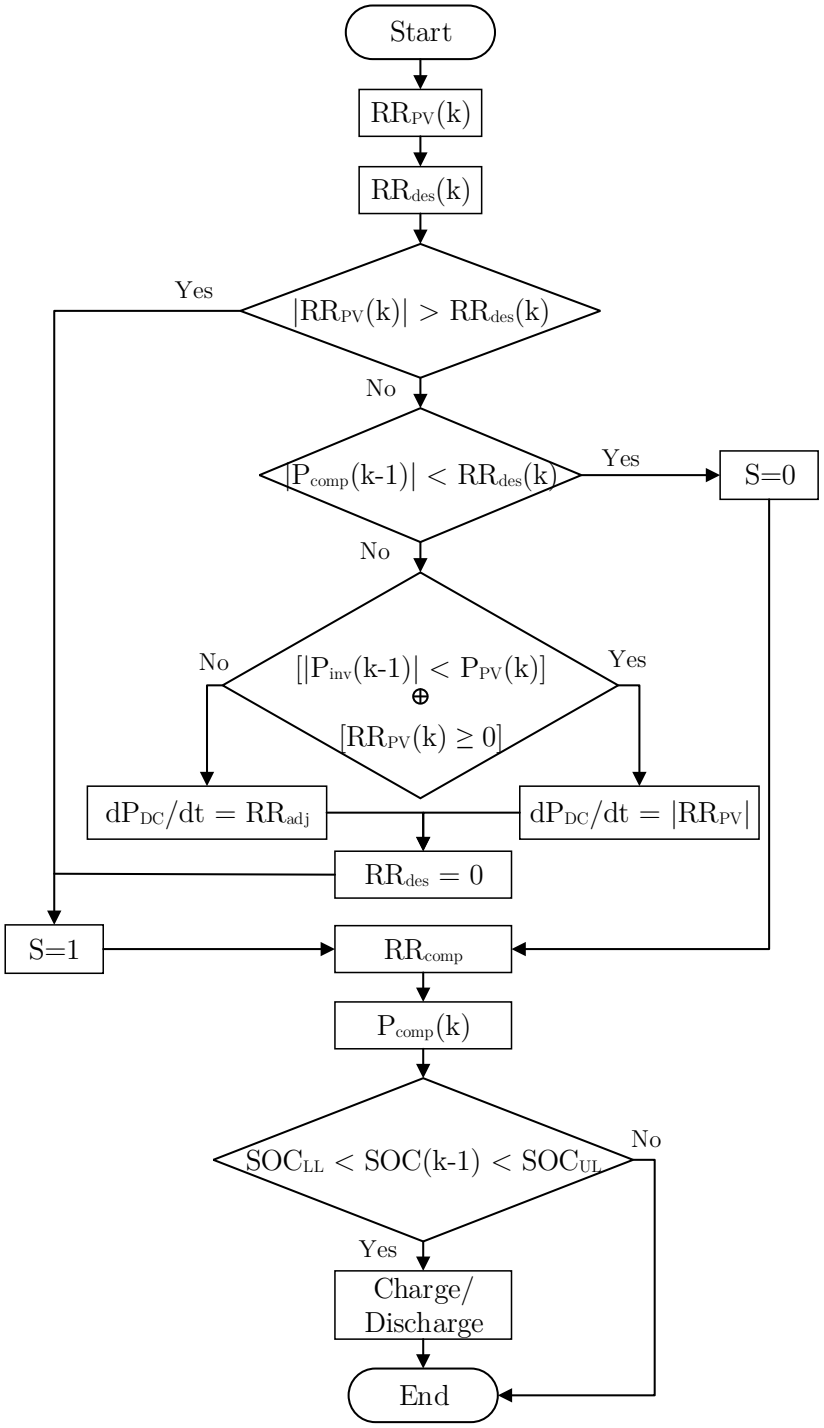

Figure 4.9: Inverter ramp-rate control strategy.

If the PV ramp-rate is not larger than the desired ramp-rate, it means that either no compensation is required or that the inverter output still has to catch up to the PV output. A check is done to determine whether or not the previous compensation power is smaller, if it exist at all, than the desired ramp-rate. If it is smaller, this means that the difference is negligible and that no compensation is required. If the compensation power is larger than the desired ramp-rate, it indicates that a post-ramping stage should be initiated. The compensation ramp-rate for this stage is calculated using certain values

which are selected based on the post-ramping situation. The value selection is summarised by expression (4.9).

Once the ramp-rate strategy is applied to the data, a profile for the battery and inverter output is available. The battery profile is used to size the BESS and is discussed in the next section.

4.3.1 Sizing of BESS

As previously stated, the battery profile generated by the fluctuation mitigation tool can be used to size the BESS. The minimum power requirement (P_{min}^{bat}) is calculated by iterating through the battery output data and selecting the highest value. This can be shown by the following expression:

$$P_{min}^{bat} = \max\left\{P_{bat}^{1}, P_{bat}^{2}, ..., P_{bat}^{n}\right\}. \tag{4.14}$$

The BESS power requirement (P_{BESS}) is determined by taking into account the losses in the power conversion unit (PCU):

$$P_{BESS} = \frac{P_{min}^{bat}}{\eta_{PCU}}, \tag{4.15}$$

where η_{PCU} is the PCU efficiency.

As the PV power output fluctuates during the course of a day, the battery system has to discharge and charge in an attempt to damp the output. The energy requirement of the battery can be determined by finding the point in the day when the battery is at maximum discharge. This essentially means determining the point where the area under the battery profile is at its maximum. Because it is assumed that the batteries will be recharged at the end of each day, the maximum required energy for each day of the year is determined to find the day which requires the most energy. The energy sizing can be expressed as follows:

$$E_{max}^{day} = \max\left\{\int_{0}^{t} P_{bat}(t)\ dt\right\} \tag{4.16}$$

$$E_{bat} = \max\left\{E_{max}^{1}, E_{max}^{2}, ..., E_{max}^{n}\right\} \tag{4.17}$$

where $P_{bat}(t)$ represents the battery profile, t represents the time, E_{max}^{day} represents the maximum required energy for the day and n is the number of days. E_{bat} represents the final battery energy requirement. The BESS energy requirement is determined by taking into account PCU losses and SOC restrictions. The equation is expressed as follows:

$$E_{BESS} = \frac{E_{bat}}{\eta_{PCU} \cdot (SOC_{max} - SOC_{min})}, \tag{4.18}$$

where SOC_{max} and SOC_{min} represent the maximum and minimum SOC, respectively.

4.4 Model Implementation and Results

The fluctuation mitigation tool shows that the intermittent nature of PV power plants can be treated using the ramp-rate control in combination with a BESS. However, this leaves users with questions about the performance and how it affects the battery sizing. To answer a few questions, how the ramp-rate limits, such as the inverse characteristic constant and the ramp-rate adjustment constant, influence the sizing of the batteries were investigated. How these constants influence the battery performance and which battery type should be considered were also investigated.

It is important to remember that the results in this section are based on a dataset from a single weather station in a certain location and that the SOH model used is also calibrated for two specific batteries. The results in this section are dependant on the weather conditions during the specific case study and thus it can not be assumed to be applicable to all cases studies. The tools merely give the user the ability to generate the results but the conclusions drawn from them will differ from one case study to the next.

4.4.1 Battery Sizing

Test data is used to showcase the functionality of the tool and to show what results can be obtained. For this example, the fluctuation mitigation tool is implemented using weather data from Stellenbosch University's Sonbesie weather station. The data of interest is the incident irradiance data and it is scaled and used as PV output data. This can be done because irradiance data is related directly to the fluctuating output of PV power plants [78–80]. The data is used as PV output power measured in watts and is scaled to represent a 5 kW PV installation. Scaling is done by using the PV area module efficiency

It was decided to vary the inverse characteristic constant (γ) and the ramp-rate adjustment constant (RR_{adj}) and determine how this affects the required battery size. In Figure 4.10, it can be seen that the energy requirement reduces with the increase in the RR_{adj} parameter. This is expected since the degree of damping reduces.

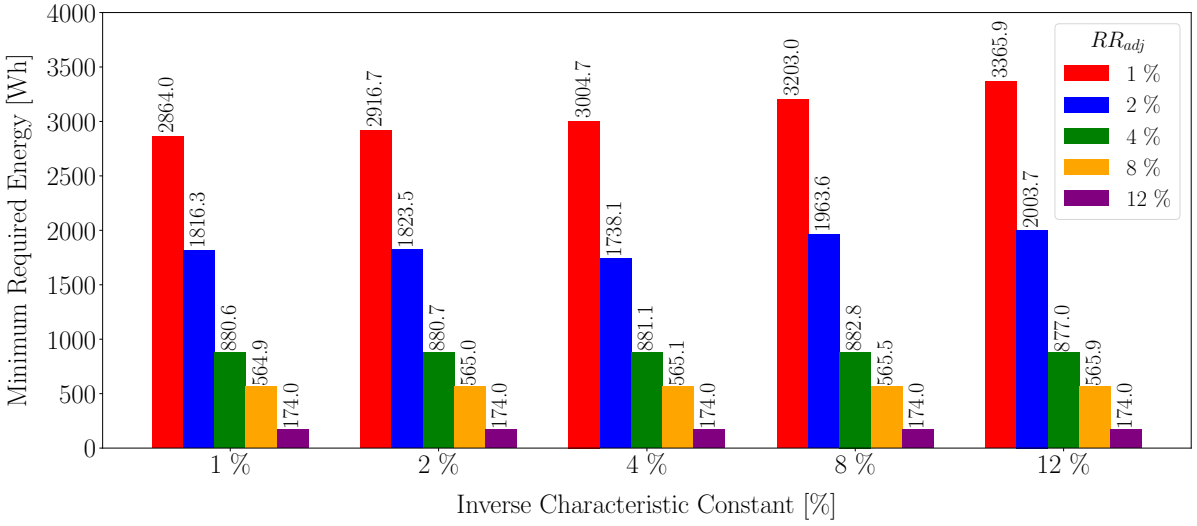

Figure 4.10: Maximum energy requirement.

Rearranging the data of Figure 4.10, it is seen that γ has no real effect on the required energy at the larger RR_{adj}. However, with the smaller RR_{adj} parameters, it is found that the required energy increases with γ.

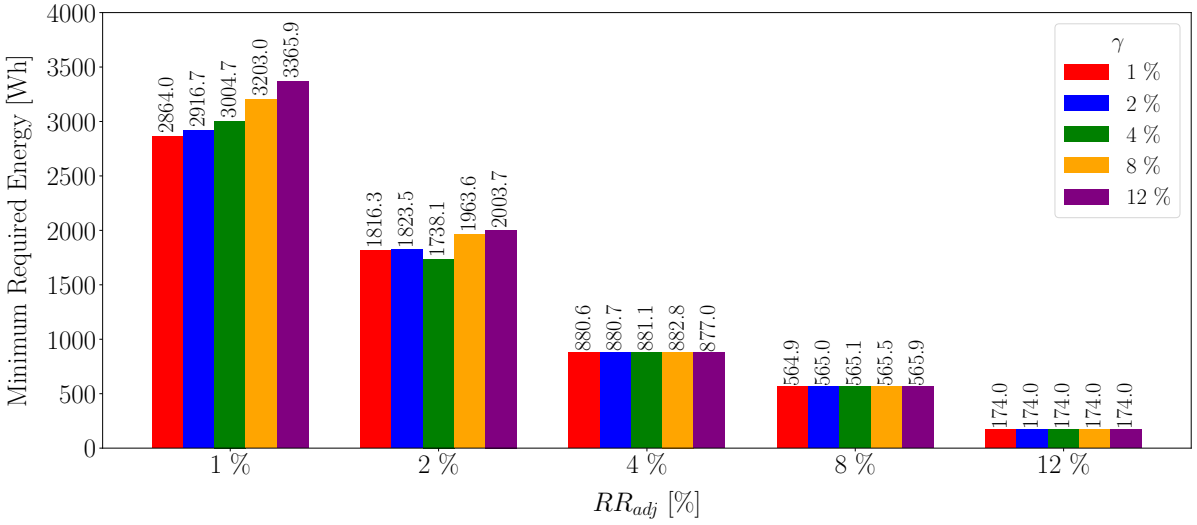

Figure 4.11: Minimum energy requirement.

Figure 4.12 shows the total energy-throughput required by the batteries at a given RR_{adj} value. It can be seen that the energy throughput reduces with higher values of RR_{adj}. This is to be expected since more damping occurs with lower RR_{adj} values. Higher energy-throughput will cause faster degradation of the SOH of the battery.

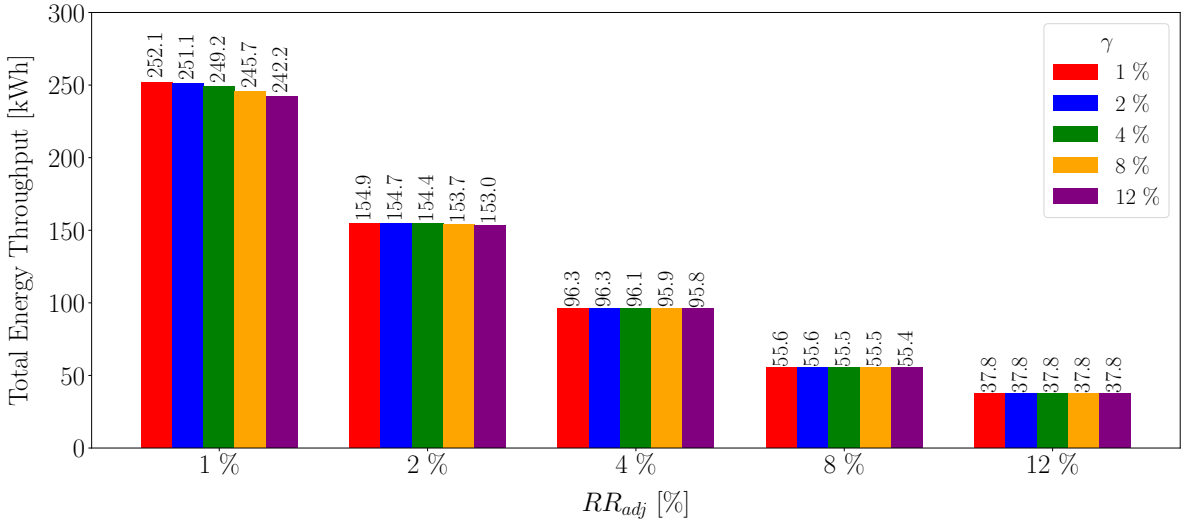

Figure 4.12: Total BESS energy throughput.

In Figure 4.13, there is no significant difference between the minimum power requirements of various γ constants and RR_{adj} constants. However, it can be seen that the power requirements starts to decline from the 12 %-mark. This is expected since the degree of

damping reduces. However, small variations between the 1 %- and 8 %-mark are noticed. This depends on the fluctuations of the PV output profile and should not be assumed as fact. Depending on the user-required ramp-rate limit, the minimum power requirements for the BESS can be specified accordingly.

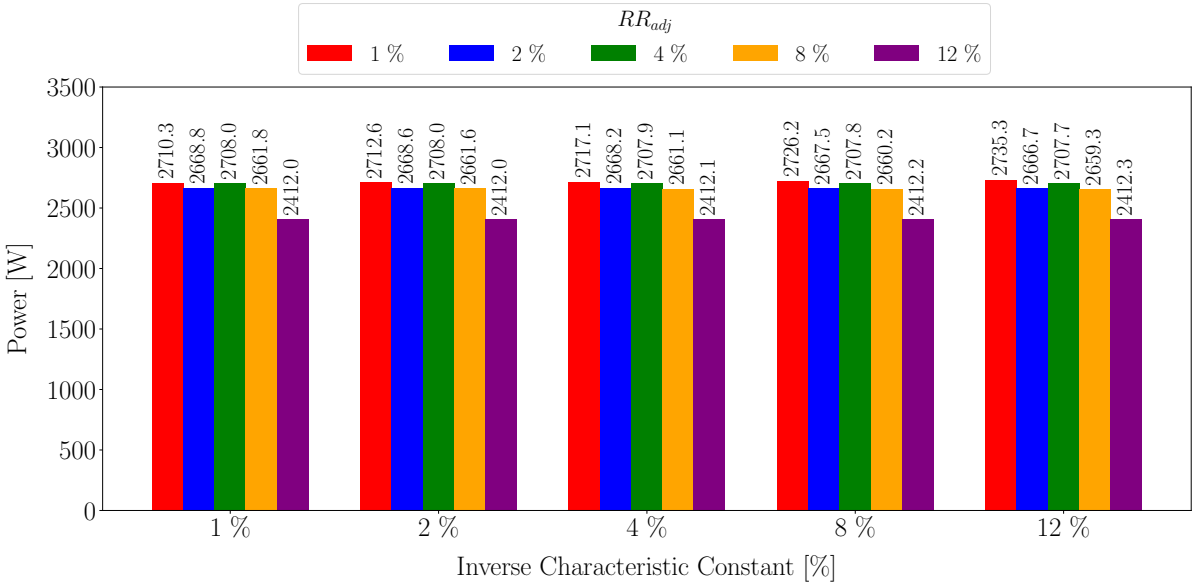

Figure 4.13: Maximum power requirement.

Since the PV installation is specified as a 5 kW system, the minimum BESS power requirement can be selected as a percentage of the peak PV installation size. Referring to the maximum power value in Figure 4.13 taken at the 1%-mark, and equation (4.14), the maximum BESS power requirement is calculated to be 3.04 kW. It is calculated using a PCU efficiency of 90%. This translates to a power requirement of 60% of the total PV installation. Similarly, the results from Figure 4.10 are compared to the maximum energy production of the PV installation, which is 29.5 kWh. This value is obtained by identifying the day in the year with the maximum energy production. This gives the required battery energy as a percentage of the maximum PV capacity installed and is illustrated in Figure 4.14.

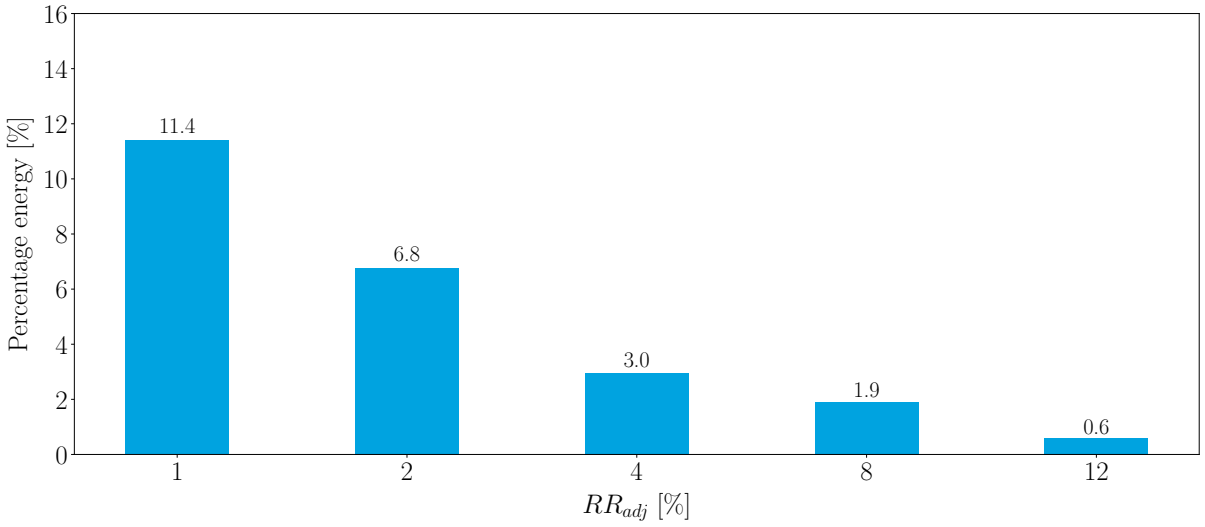

Figure 4.14: Battery energy requirement as a percentage of maximum installed PV capacity.

Again, a PCU efficiency of 90% is used for both the lithium and lead-acid systems. Lithium batteries are less affected by high DODs [18], thus the minimum SOC is set to 10%. For lead-acid batteries on the other hand, it is set to have a minimum SOC of 40% and both systems will be allowed a maximum SOC of 100%. Since γ did not affect the energy requirement as much as RR_{adj}, the maximum value from each of the RR_{adj} simulations is used as the representing minimum energy requirement. Since lithium and lead-acid chemistries operate under different optimal DODs, their required capacities differ for the same application.

Applying the system constraints using equation (4.16) on the requirements in Figure 4.14, the recommended BESS capacity for each of the battery chemistries can be examined in Figure 4.15. It is noticed that the required capacity for lead-acid is nearly double that of the energy required for the damping of the PV inverter output. The lithium system is specified between 17-26% higher than the required energy for smoothing. The lead-acid capacity requirement is also about 50 % higher than the lithium battery capacity. It is important to note that the resulting BESS requirements differ based on the PCU specifications and the manufacturer's recommended battery operating conditions.

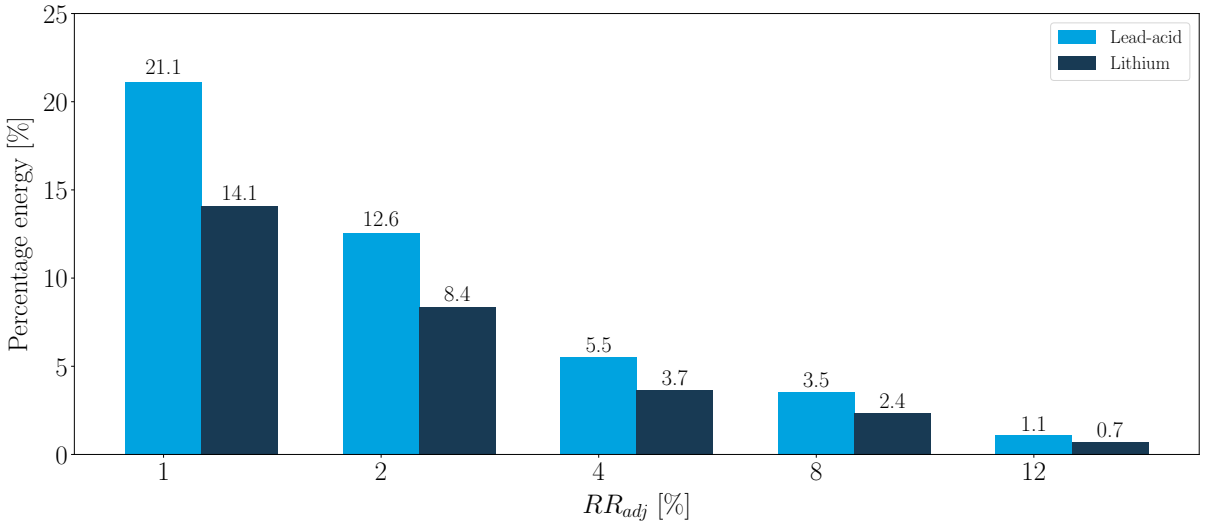

Figure 4.15: BESS energy requirements as a percentage of maximum installed PV capacity.

4.4.2 Battery Performance and Selection

Since the required BESS size is known, a choice must be made regarding which battery type to choose. Lithium-ion ($LiFePO_4$) and lead-acid ($PbSO_4$) batteries are being considered in this case. Using the SOH tool in Section 2.7, the performance of the two battery types can be compared. The performance of each battery is tested based on the recommended battery size in the previous section with its correlating RR_{adj} parameter.

Figure 4.16 illustrates the results of the SOH performance tests where both battery chemistries are operated at 25°C. It can be seen that the battery performance decreases with the increase in the RR_{adj} parameter. This can be explained by comparing Figures 4.11 and 4.12. The maximum required energy increases at a higher rate than the energy-throughput when RR_{adj} lowers; thus, the BESS has higher specifications at a lower RR_{adj} for the respective energy-throughput profiles.

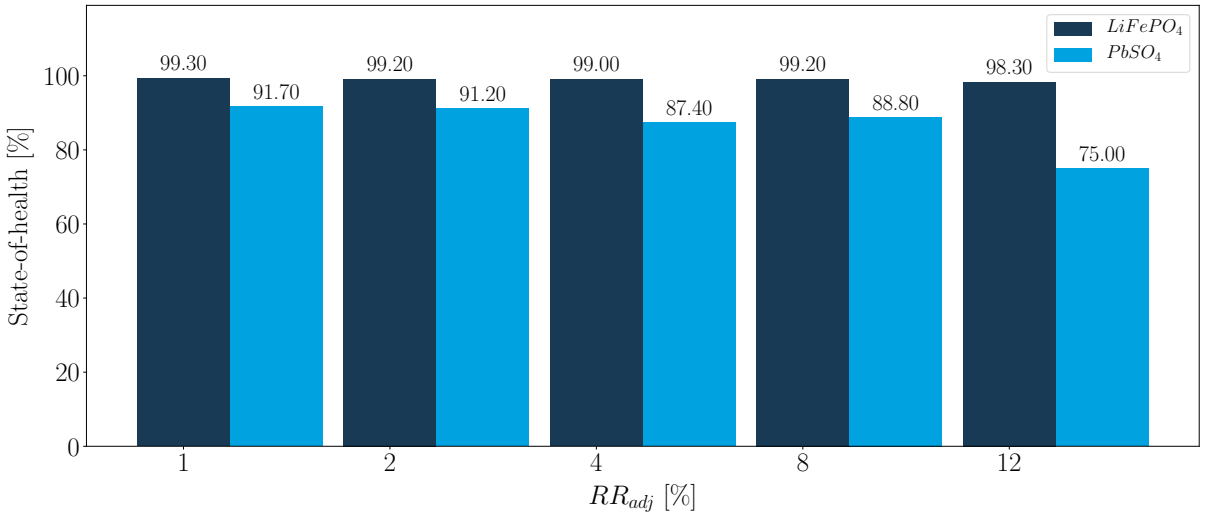

Figure 4.16: Estimated battery SOH after one year of fluctuation mitigation.

Choosing the battery type is not as simple as choosing the best battery technology. It is common knowledge that lithium has impressive characteristics such as its high energy density and low self-discharge. However, lithium technologies are more expensive.

From Figure 4.16, it is clear that the degradation on a lead-acid battery is much higher than that on the lithium battery. Looking at the application of the BESS in this case, one has to consider the costs and the required life time of the battery. The typical utility scale PV power plant is designed for a lifetime of approximately 20 years. Considering that lead-acid batteries have a calendar life of 3-6 years and lithium 5-10 years [18], one would have to consider the number of times that the batteries will need replacement during the lifetime of the plant. As discussed before, manufacturers usually recommend a lower DOD for lead-acid storage systems. This is done to prevent accelerated degradation but results in higher costs due to more batteries being required to deliver the same amount of energy as the lithium technology.

Based on recent studies such as Lizard's Levelised Cost of Storage in 2016 [81] and 2015 [82], the levelised cost of lithium batteries is considerably lower than lead acid for applications such as PV integration, transmission systems, distribution substations, distribution feeders and frequency regulation. Also, with recent news with regard to the joint effort of big companies like Tesla and Panasonic, the cost of lithium battery production will become even more competitive [83]. Therefore that lithium batteries, the $LiFePO_4$ battery in this case, will be the recommended choice.

4.5 Conclusion

The intermittent nature of PV power outputs is becoming an increasing concern as penetration on the grid increases. In this chapter, investigation of different PV fluctuation mitigation is described. The inverter ramp-rate approach is chosen for its superior battery utilisation and then implemented in the form of a Python script. The script uses the output profiles from the PV power plants as its input and applies the fluctuation mitigation method. It provides the inverter output profile and the battery profile as outputs for further analysis.

The method is tested at different degrees of damping and how this affects the sizing of batteries with regards to peak power and energy is investigated. It was found, with regards to the specific test case, that the peak power remained mostly unchanged for the various degrees of damping. However, higher degrees of damping, specifically the ramp-rate adjustment parameter, caused an increase in the energy requirement. At the lower ramp-rate adjust parameters, the energy requirement increases with an increased inverse characteristic constant. The overall energy-throughput was also investigated and it was found that higher damping causes higher energy-throughput.

Two battery systems are sized based on the peak power and energy requirements. Two different chemistries are used and the BESS is sized such that each chemistry is used optimally. Knowing that the energy-throughput causes battery degradation, the two systems are tested for each of the different degrees of damping. It was found that there is a decline in performance of the BESS as the damping decreases. This is because the battery requirements reduce more than the energy-throughput with decreased damping. The SOH performance test showed that the lithium chemistry is superior even when the lead-acid chemistry is sized for a lower DOD. Based on studies on the levelised cost of

storage, lithium batteries are the more cost-effective choice for fluctuation mitigation.

The tool proves very useful not only for determining the required BESS specifications but also to determine the characteristics of the ramp-rate model on certain data sets and how these influence the BESS.

Chapter 5

Network Strengthening

The world is pushing for the adoption of renewable energy sources to service the need for more energy [84–86]. Renewable technologies, like most new technologies, experience challenges. The intermittent nature of renewable energy sources is one of the main challenges that energy providers are faced with owing to renewable energy's dynamic nature being reflected in the electric network [87, 88], particularly in weaker networks.

Renewable energy sources bring a variety of challenges, however, the focus of this chapter is on the connectivity of photovoltaic (PV) power plants, to weak electrical networks whilst maintaining grid code compliance. PV power plants tend to be located in areas where irradiance is at its maximum. In South Africa, the majority of utility scale PV power plants are located at remote locations closer to small towns in the warm countryside of the Northern Cape [89]. A radial network layout with longer transmission lines characterises the power grids in these areas. The combination of industrial, commercial and residential loads in these networks leads to higher resistance to reactance ratios, which results in weaker networks [10].

The high impedance nature of weak networks can result in unstable voltage levels when a sudden loss in generation occurs. The loss can occur due to passing cloud cover or due to a fault condition. PV power producers cannot get approval, from the network service provider to connect to the electric grid if their proposal cannot guarantee grid operation under all conditions [90]. On-load tap changing (OLTC) transformers allow for the adjustment of voltages whilst under load. This allows the grid to operate within specified voltage limitations. The problem, however, is that OLTC transformers are set up to have an intentional delay before changing taps [91–93]. This delay avoids unnecessary tap changes when fluctuations of shorter durations occur. An example is the high start-up current of motors on the network.

A solution is proposed in which an energy storage system is used to provide support during the intentional delay of the OLTC transformer in order to maintain grid code compliance. Grid code compliance refers to the ability of power producers, connected to the public electric network, to remain within the technical specifications of the national grid code. This code defines the parameters and constraints which a connected facility needs to meet in order to ensure a safe and secure electrical grid. To maximise the RPP installation capacity on a weak grid, an battery energy storage system (BESS) is proposed to ensure grid code compliance. The latest grid connection code for RPPs [90] in South Africa (SA), version 2.9 at the time of writing, will be used in this thesis.

In this chapter, there is a description of the investigation into the modelling of a weak

electric network. The characteristics that define a network are identified and explained as well as the roles of the active and reactive power in the network. The renewable energy grid codes relevant to this study are discussed. A brief overview is given of transformers as well as the software tool used to simulate the problem. The network problem is evaluated and followed by a solution where the various applied controllers are discussed.

5.1 AC Network Fundamentals

The AC network is characterised by its resistance, inductance and capacitance. In this section these components and what they mean for the network, are discussed.

5.1.1 AC Resistance

Figure 5.1 represents a pure resistive circuit and the closing of switch S causes the voltage to be applied over R. The current starts to flow through the resistor in a sinusoidal waveform following the rise and fall of the voltage in perfect phase as illustrated by Figure 5.2. However, the higher this resistance; the lower the amount of current which can flow through it. [94]

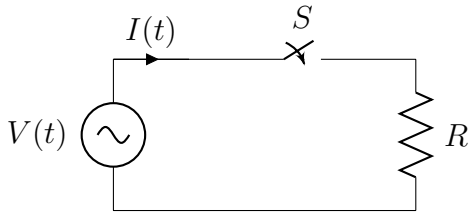

Figure 5.1: Pure resistance representation.

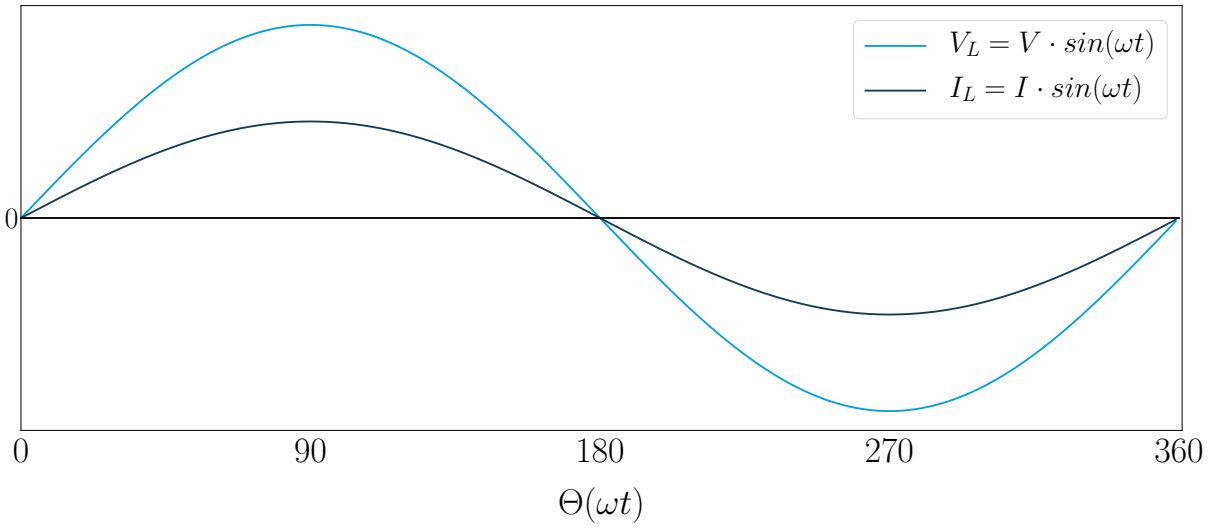

Figure 5.2: Voltage and current representation for pure resistance.

5.1.2 AC Inductance

Figure 5.3 represents a pure inductive circuit and the change in current causes a magnetic field to be induced in the coil of the inductor (labelled L). Since the voltage source is AC, the polarity of the voltage changes which causes the current to change direction before it can reach its maximum possible value. The change in direction gets delayed by the self-induced back electromotive force in the coil. Thus the current gets delayed by 90° as illustrated by Figure 5.4. [94] As the inductance increases, the rate of change in current decreases; leading to decreased amplitude of the current. This can be in equations 5.1 and 5.2 as below:

$$V = L\frac{dI}{dt} \tag{5.1}$$

Rewriting equation (5.1) in terms if I:

$$I = \frac{1}{L}\int V_L(t)\,dt \tag{5.2}$$

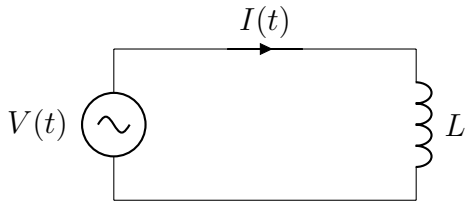

Figure 5.3: Pure inductance representation.

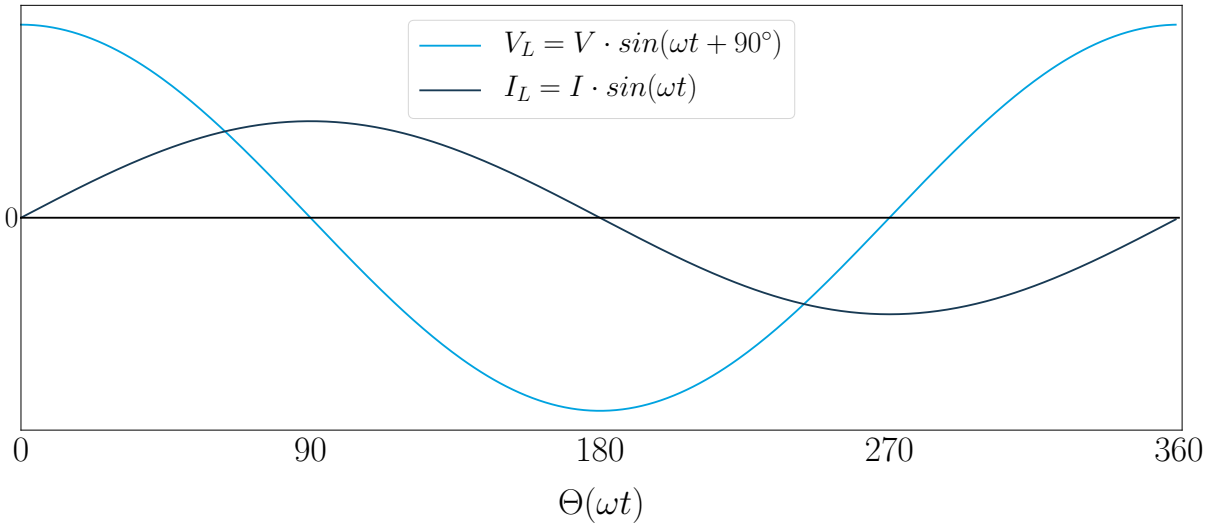

Figure 5.4: Voltage and current representation for pure inductance.

5.1.3 AC Capacitance

Figure 5.5 represents a pure capacitive circuit. The closing of switch S causes a high current to flow when the voltage is at its maximum rate of change, at zero crossing, as illustrated by Figure 5.6. High current occurs because there is no charge on the plates. The change in voltage slows down as it approaches its maximum value at 90°. At this moment, the current flow stops briefly and, passing this point, the current discharges in the opposite direction in an effort to maintain a constant voltage. This occurs since the voltage is reducing and the change in voltage is increasing. This is all illustrated in Figure 5.6. It can be examined how the voltage reaches its maximum a quarter of a cycle after the current reaches its maximum; thus voltage applied to a purely capacitive circuit lags the current by 90°. [94] An increase in the capacitance causes an increase in the amplitude of the current. This can be examined from equation 5.3.

$$I = C\frac{dV}{dt} \tag{5.3}$$

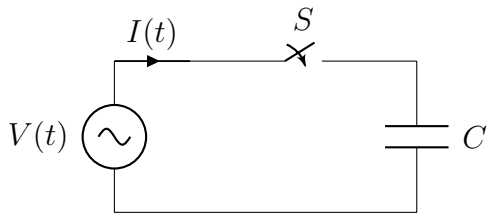

Figure 5.5: Pure capacitance representation

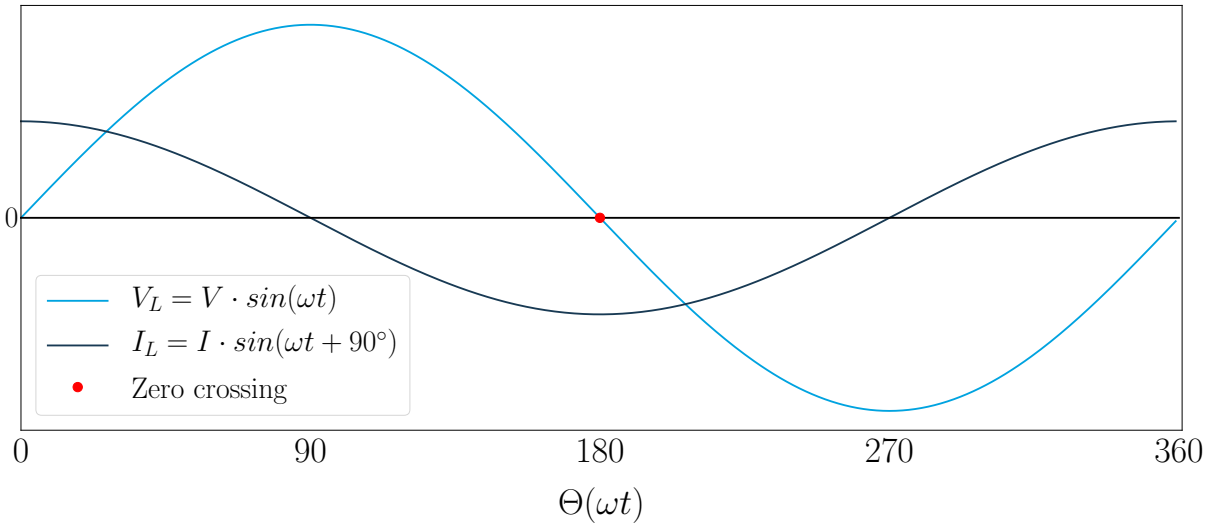

Figure 5.6: Voltage and current representation for pure capacitance.

In summary, a higher resistance in an electric network restricts current, a higher inductance causes a delayed and lower current and higher capacitance causes a delayed voltage and higher currents. Typically, all these characteristics should be kept at a minimum.

5.2 Network Modelling

A network model is created to serve as a foundation on which the solution can be built. Since the transmission network will be simulated in DIgSILENT PowerFactory (DPF), it is important to study how the various networks can be represented to simplify the modelling process even further. Duncan *et al.* [94] show that transmission networks of different sizes can be conveniently approximated by equivalent circuit models. These transmission networks are typically divided into short, medium and long transmission lines and are represented as a two-port network as illustrated by Figure 5.7.

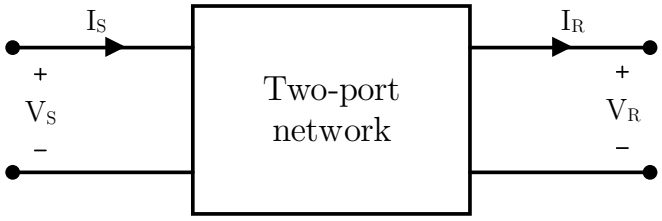

Figure 5.7: Two-port network.

V_S and I_S are the sending-end voltage and current and V_R and I_R the receiving end voltage and current. The relationship between these voltages and currents can be expressing by the following equations:

$$V_S = A \cdot V_R + B \cdot I_R \quad [\text{V}] \tag{5.4}$$

$$I_S = C \cdot V_R + D \cdot I_R \quad [\text{A}] \tag{5.5}$$

This can also be represented in matrix format:

$$\begin{bmatrix} V_S \\ I_S \end{bmatrix} = \begin{bmatrix} A & B \\ C & D \end{bmatrix} \begin{bmatrix} V_R \\ I_R \end{bmatrix} \tag{5.6}$$

where A, B, C and D are parameters which represent the transmission line characteristics. These characteristics depend on transmission line constants such as resistance (R), inductance (L), capacitance (C) and shunt conductance (G) and will be discussed in the sections to follow.

5.2.1 Short Line Approximation

Short transmission lines typically have a length, ℓ, below 80 km for an overhead lines and the shunt admittance is neglected [95]. These assumptions can be applied to single phase lines as well as three-phase lines which operate under balanced conditions. The equivalent circuit for a short transmission line is illustrated by Figure 5.8. [94]. Applying Kirchhoff's voltage and current laws, the equations of this model are:

$$V_S = V_R + Z \cdot I_R \tag{5.7}$$

$$I_S = I_R \tag{5.8}$$

or in matrix format:

$$\begin{bmatrix} V_S \\ I_S \end{bmatrix} = \begin{bmatrix} 1 & Z \\ 0 & 1 \end{bmatrix} \begin{bmatrix} V_R \\ I_R \end{bmatrix} \tag{5.9}$$

where $Z = (R + j\omega L)\ell$ is the series impedance for the length of transmission line.

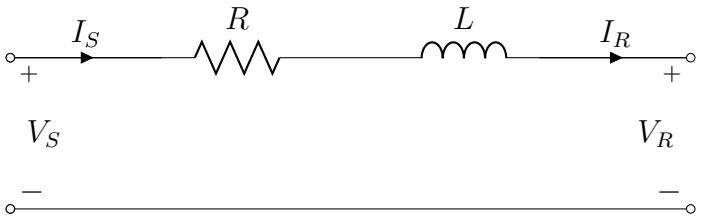

Figure 5.8: Short transmission line model.

5.2.2 Medium Line Approximation

Medium transmission lines are typically between 80 to 250 km in length [95]. The transmission lines are modelled such that the total shunt admittance is lumped and split in half with a half at each end of the line. This model is called the *nominal* π *circuit* and is illustrated in Figure 5.9. Applying Kirchhoff's voltage and current laws, the equations for this model are:

$$V_S = \left(1 + \frac{YZ}{2}\right) V_R + Z I_R \tag{5.10}$$

$$I_S = Y\left(1 + \frac{YZ}{4}\right) V_R + \left(1 + \frac{YZ}{2}\right) I_R \tag{5.11}$$

or in matrix format:

$$\begin{bmatrix} V_S \\ I_S \end{bmatrix} = \begin{bmatrix} \left(1 + \frac{YZ}{2}\right) & Z \\ Y\left(1 + \frac{YZ}{4}\right) & \left(1 + \frac{YZ}{2}\right) \end{bmatrix} \begin{bmatrix} V_R \\ I_R \end{bmatrix} \tag{5.12}$$

where $Y = (G + j\omega C)\ell$ is the shunt admittance for the length of transmission line.

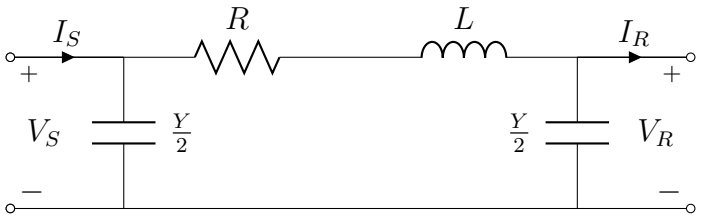

Figure 5.9: Nominal π circuit.

5.3 Grid Characteristics

The strength of the grid is its ability to maintain voltage stability [96]. A model is required that represents a weak electric grid; a grid with voltage instability. It is important to understand how a weak grid is defined in order to understand and model the problem. This model will represent the problem statement and serve as a platform on which the solution can be built.

Figure 5.10 is a simple representation of a PV power plant connected to an electric grid. The connection between the two is characterised by the impedance (Z) and total shunt admittance (Y) between them. The impedance consists of two respective parts: the resistive (R) component and the inductive (X) component. The magnitude of and the ratio between these components inevitably define the characteristic strength of the grid. The magnitude and ratio are represented by the short-circuit ratio (SCR) and the X/R-ratio, respectively [96–99]. The shunt admittance is composed of a capacitive (C) and conductive (G) component. The conductive component is usually neglected since it is a very small component of the shunt admittance [94].

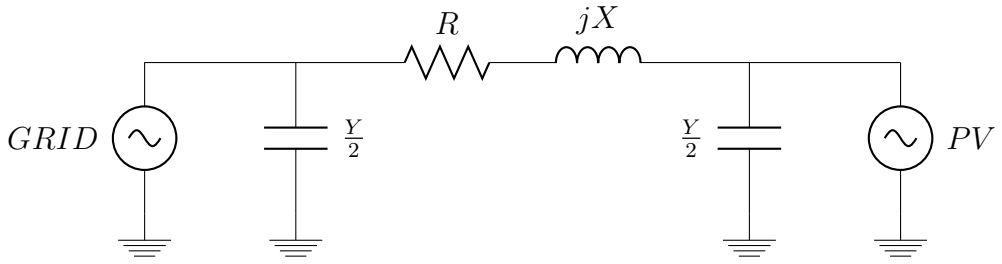

Figure 5.10: Simple grid connected PV example.

5.3.1 Short-Circuit Ratio

The SCR can be defined as the AC system admittance expressed in per unit of the DC power. Gavrilovic states that the SCR can be accepted as an approximation of the grid strength [96]. According to Etxegarai *et al.* [99], a weak grid is characterised by its low short-circuit power, high grid impedance, low mechanical inertia and lack of spinning reserves. Typically, there is a point of common coupling (PCC) where the power plant connects into the national grid and when viewing the grid from this point, it can be evaluated by its short-circuit power. The short-circuit power can be represented by what is called the grid stiffness index; also known as the short-circuit ratio.

According to Etxegarai *et al.* and Grunau *et al.*, a grid is typically considered strong when the SCR is above 20 to 25 and it is considered weak when the SCR is below 6 to 10 [97–99]. The short circuit ratio is expressed by the following expression:

$$SCR = \frac{S_{SC}}{S_{PV}} \tag{5.13}$$

where S_{SC} is the full short-circuit power to ground as seen by the PCC and S_{PV} is the rated PV power from the installed capacity. Since the electric grid is being modelled using a Thevenin equivalent circuit, the parameters of the grid need to be determined theoretically. The short circuit power is calculated as follows:

$$S_{SC} = \frac{U_{PCC}^2}{Z_{weak}} \tag{5.14}$$

where U_{PCC} is the voltage at the point of common coupling and Z_{weak} is the grid impedance but in this case, a weak grid. Combining equation 5.13 and 5.14, the short-circuit ratio can be represented by the following expression:

$$SCR = \frac{U_{PCC}^2}{Z_{weak} \cdot S_{PV}} \tag{5.15}$$

5.3.2 X/R-Ratio

In the context of an electrical grid, the AC circuit representing the grid consists of an inductive and a resistive part as illustrated by Figure 5.10. The X/R-ratio is the ratio between the inductive component and the resistive component. It is considered weak when it is of ohmic character (i.e. when it has an X/R-ratio of less than 1) [97]. The X/R-ratio is represented by the following equation:

$$ratio = \frac{X}{R} \tag{5.16}$$

For the purpose of this thesis, Z_{grid} will represent the grid impedance as seen from the PCC. The two above-mentioned components make up the grid impedance as follows:

$$Z_{grid} = R + jX \tag{5.17}$$

From the grid X/R-ratio (xrr) and the grid impedance, one can calculate the respective inductive and resistive parts using the following equations:

$$X = \frac{|Z|}{\sqrt{1 + (\frac{1}{xrr})^2}} \tag{5.18}$$

$$R = \frac{|Z|}{\sqrt{1 + xrr^2}} \tag{5.19}$$

5.4 Active and Reactive Power

The AC network consists of two kinds of power: active power (P) and reactive power (Q). Active power is measured in Watts (W) whilst reactive power is measured in volt-ampere reactive (VAr). The two types of power form part of a triangle and together make the apparent power (S), measured in volt-ampere (VA), as illustrated in Figure 5.11.

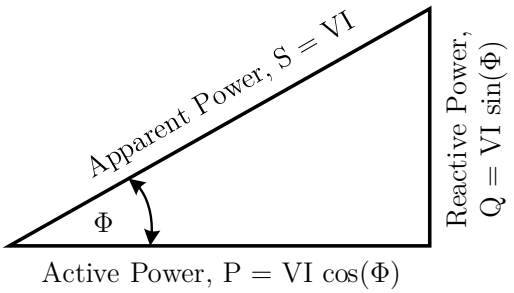

Figure 5.11: Power Triangle.

The relationship between the different types of power can be represented, through the use of Pythagoras, by the following expression:

$$S = \sqrt{P^2 + Q^2}, \tag{5.20}$$

or by the power angle (Φ) and power factor as follows:

$$\text{Power Factor (PF)} = \frac{\text{Active Power (P)}}{\text{Apparent Power (S)}} = \cos(\Phi) \tag{5.21}$$

Active power is produced by PV in this thesis and consumed by the resistive parts in circuits. Appliances such as heaters, irons, kettles and filament bulbs, where the reactance is practically zero, consume only active power. In these types of circuits, the voltage and current are in-phase.

Reactive power is the part of electricity that helps establish and sustain the electric and magnetic fields required by AC equipment such as motors, generators and transformers. Reactive power consumes capacity on transmission lines but it can be applied such that it assists in regulating the voltage levels which helps with the transportation of power through the network. Reactive power is usually used to lift voltage levels in cases where there is not enough active power available.

The national grid code constrains large power producers and consumers by a power factor in an effort to reduce the capacity that the reactive power consumes on the network and increase system efficiency. Power producers can also be asked to assist with reactive power control. Industrial customers typically use large 3-phase motors with widely different power factors which can lead to reactive power charges. These charges can be avoided by installing power factor correction capacitors or a static-var compensator. For the purpose of this thesis, active power support will be considered, by means of a battery storage system, because reactive power consumes network capacity and is limited by the network service provider.

5.5 National Renewable Grid Codes

The aim of the researcher is to use and size batteries to provide active power support at the PCC such that stable voltages are maintained. The national renewable grid codes stipulates these voltage constraints under normal and abnormal operating conditions [90].

To ensure stable gird operations the BESS needs to be applied in such a way that the PCC adheres to the voltage constraints.

5.5.1 Categorisation of Renewable Power Plants

Section 3 of the grid code divides renewable power plants (RPP) into three categories for installation: category A, category B and category C installations. Category A is divided into three sub categories:

- Category A1: 0 - 13.8 kVA
- Category A2: 13.8 kVA - 100 kVA
- Catagory A3: 100 kVA - 1 MVA

Category B ranges from a 1 MVA to a 20 MVA installation and Category C installations are 20 MVA and larger installations. For the purpose of this thesis, the Category C RPP installations will be considered.

5.5.2 Normal Operating Conditions

According to the grid code, a Category C RPP should be designed to operate continuously within the PCC voltage range as specified by *Umin* and *Umax* in Table 5.1. The grid code also states that the actual operating voltages can differ from location to location and that the network service provider will consult with affected customers.

Table 5.1: Minimum and maximum operating voltages at PCC. [90]

Nominal (U_n) [kV]	U_{min}	U_{max}
132	0.90	1.0985
88	0.90	1.0985
66	0.90	1.0985
44	0.90	1.08
33	0.90	1.08
22	0.90	1.08
11	0.90	1.08

5.5.3 Abnormal Operating Conditions

According to Section 5.2 of the grid code under abnormal operating conditions, the RPP should be designed to withstand sudden phase jumps of up to 20° at the PCC without disconnecting or reducing its output. Under fault conditions, the renewable energy power plant should be capable of the voltage ride-through as shown in Figure 5.12. It should withstand voltage peaks up to 120 % of the nominal voltage for a maximum period of 2 seconds and it should also withstand voltage dips up to 0 % for a maximum of 0.15 seconds.

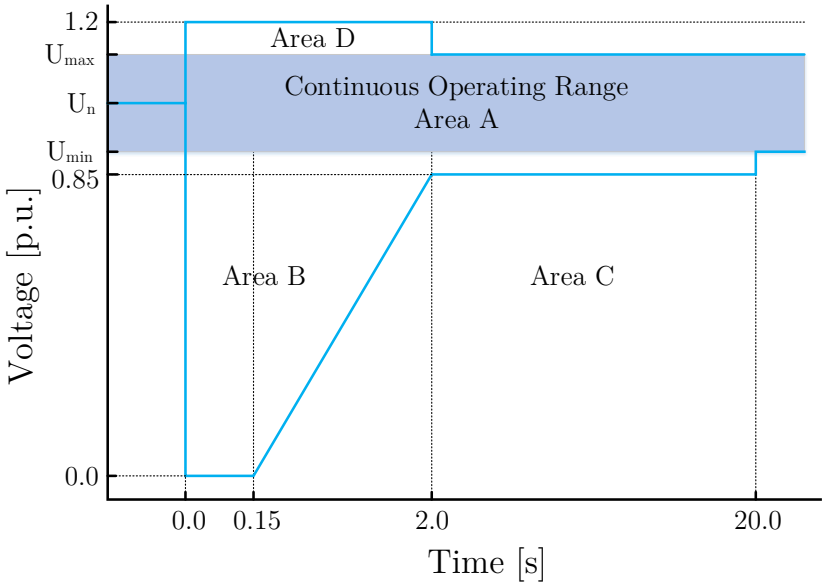

Figure 5.12: Voltage Ride through Capability for the RPPs. [90]

As can be seen in Figure 5.12, there are various operating areas that range from area A to D that apply to abnormal operating conditions. Section 5.2.1 in the grid code describes the operational instructions for these areas as follows:

- **Area A:** RPPs should stay connected and uphold normal operating conditions.
- **Area B:** RPPs should provide maximum voltage support by providing controlled amounts of reactive current in order to assist in stabilising the voltage. Also, inverter-driven RPPs must be able to disable reactive current support at the request of the system or network operators.
- **Area C:** When the PCC voltage transitions into this area, RPPs are allowed to disconnect.
- **Area D:** RPPs should stay connected and provide maximum voltage support by absorbing controlled amounts of reactive current to help stabilise the voltage.

5.5.4 Active Power Curtailment

Active power curtailment refers to the reduction of power at the demand of the network service provider. According to Section 6.1 of the grid code, RPPs will provide mandatory active power reduction during high frequency operations in order to stabilise the frequency. Section 11 of the grid code states that the network service provider will curtail the active power of RPPs if necessary. Section 11 of the grid code also states that the generators of RPPs should be capable of operating at reduced power levels if the command for curtailment is given.

A sudden loss of generation on a weak network can cause a voltage drop on the PCC bus which in turn causes a voltage drop across the grid bus. Consequently, the fault conditions on a PV power plant can lead to unstable network operation. The addition of a BESS could ensure compliant network operation.

5.6 On-Load Tap Changing Transformers

A transformer is a power system device that connects different voltage levels with one another. It serves as a link between the power generators and the transmission lines and a link between lines of different voltage levels. Transmission lines usually operate at higher voltages of up to 765 kV line-to-line. Generators, on the other hand, usually operate in the range of 18 to 24 kV. Transformers are also used to step the voltage down to residential levels of 240 V.

The on-load tap changer is an internal mechanism that allows transformers to select between different turn ratios by adding to or subtracting from the primary or secondary windings. Tap changers are found especially in high-voltage transformers and the different ratios are selected in discrete steps [100]. The changing of taps is based on the "make before break" contact concept because the momentary loss of load is unacceptable. This change occurs by connecting the tap winding to a fixed potential by a fixed ohmic resistor during the changeover operation.

There are several different tap winding connections and Figure 5.13 illustrates some basic examples. Linear sectors are typically used in power transformers which have moderate regulating ranges of up to 20 %. The changed taps are added or subtracted in series with the main windings. [101]

The single reversing change-over selector adds/subtracts tap windings to/from the main winding. This configuration is used to double the regulating range or to reduce the number of taps. During the change-over operation, the tap windings have to disconnect from the main windings which can cause recovering voltages to reach critical levels. This causes inadmissible discharges in the change-over selector. Also, the copper losses for the selector are at their highest with the minimum number of effective turns. [101]

In order to avoid disconnection during tap changes, the double reversing change-over selector uses an advance-retard switch (ARS). The coarse change-over selector suffers from the same recovering voltage problem during its coarse selector operation but its copper losses are at a minimum with the lowest number of effective turns. [101]

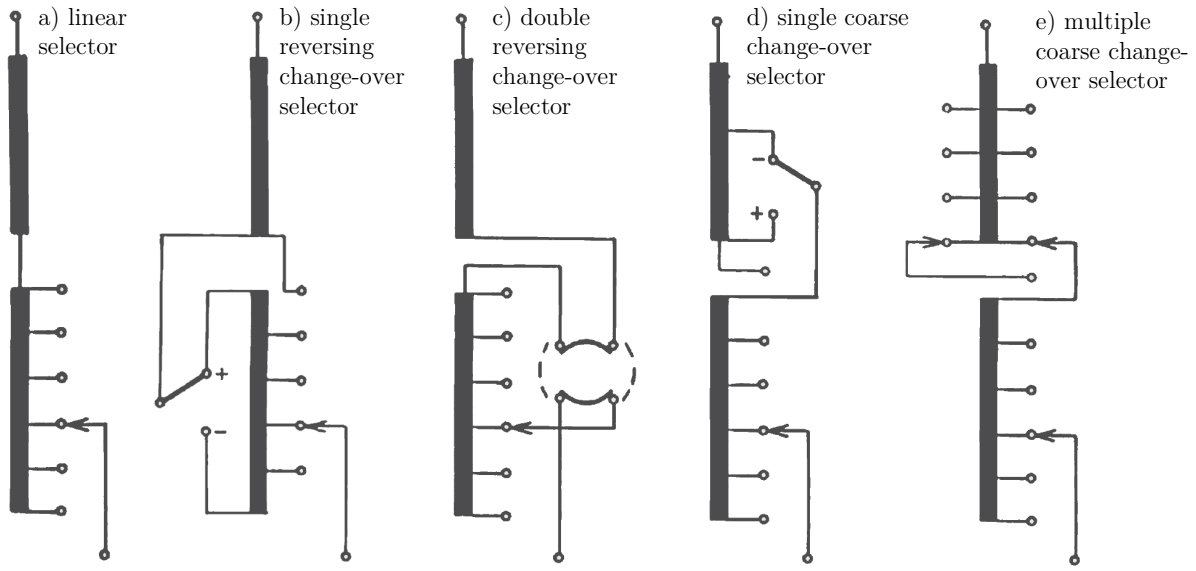

Figure 5.13: Tap winding connections. [101]

The different tap-changer implementations have various tap chaning times and voltage step sizes. The type of tap-changer used influences the BESS size because it will determine how much energy the BESS will need to discharge while the transformers restores stable operating voltages. Thus, if possible, the transformer should be selected to compliment the BESS.

5.7 DIgSILENT PowerFactory

DPF is a software simulation tool with great modelling and data handling capabilities that caters for most of the needs required for power system analysis. This software package is considered to be an industry standard simulation tool. The software package consists of a comprehensive library of model and power system components. It also allows users to create customised models and control systems. This can all be done within a graphic user interface which allows for the creation of powerful network diagrams and the plotting of dynamic time-based results. The Stability Analysis Functions (RMS) simulations paired with the software's graphing capabilities allow for a very powerful simulation tool that satisfies the needs of simulating weak networks for this thesis. The RMS simulation is typically used for the voltage stability analysis when considering the effects of load variations, tap-changer control and reactive power limits.

5.8 Network Evaluation

Currently, the Renewable Energy Independent Power Producer Procurement Programme (REIPPPP) determines that utility scale PV power plants in South Africa may not exceed the capacity of 75 MW. Commercial power producers tend to install larger capacities in order to reduce the cost per kWh generated. It is; thus, necessary to evaluate how weak network characteristics can restrict the installation capacity. It is important to note that the specifications of the networks and the power plants involved change based on location

and design. The evaluation described in this chapter is for a single case only. The purpose is to demonstrate the process.

5.8.1 Network Model

A network model is required to represent the case of a PV power plant connected to a weak grid. The model that is implemented is based on a DPF model used by a company which designs and commissions PV power plants and it is illustrated in Figure 5.14. The grid is modelled using an AC voltage source and a network impedance block that connects to the grid bus through an OLTC transformer. The grid bus is connected to the PCC through a transmission line. The transmission line is modelled using a simple network impedance block. The PCC represents the substation where the PV power plant is connected. The PV power plant is also connected to the PCC through an OLTC transformer.

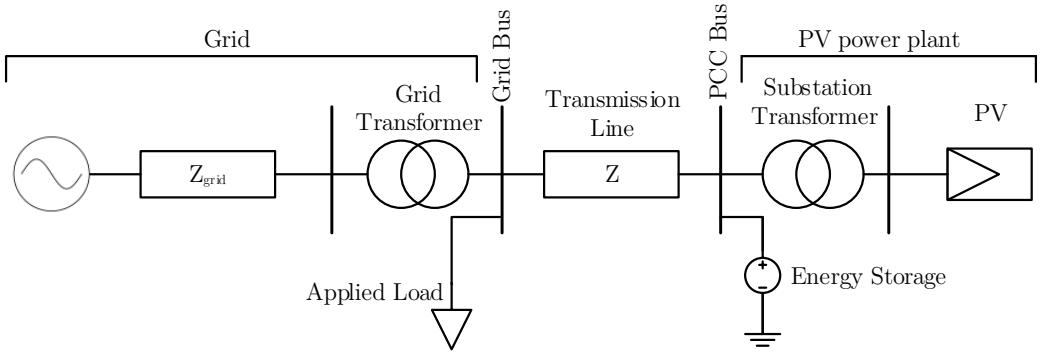

Figure 5.14: PowerFactory implemented network model.

5.8.2 PV Power Plant Model

The PV power plant model is illustrated in Figure 5.15. Starting from the right the total PV array is represented by the DPF PV system module and it is connected to a 22/0.36 kV step-up transformer. An internal cable from the PV power plant connects the PV step-up transformer to the substation transformer at the PCC. Capacitor banks are located at the substation as specified by ESKOM. These capacitor banks are disabled for this test case. The substation transformer steps the voltage up from 22 kV to 132 kV where it connects with the transmission line.

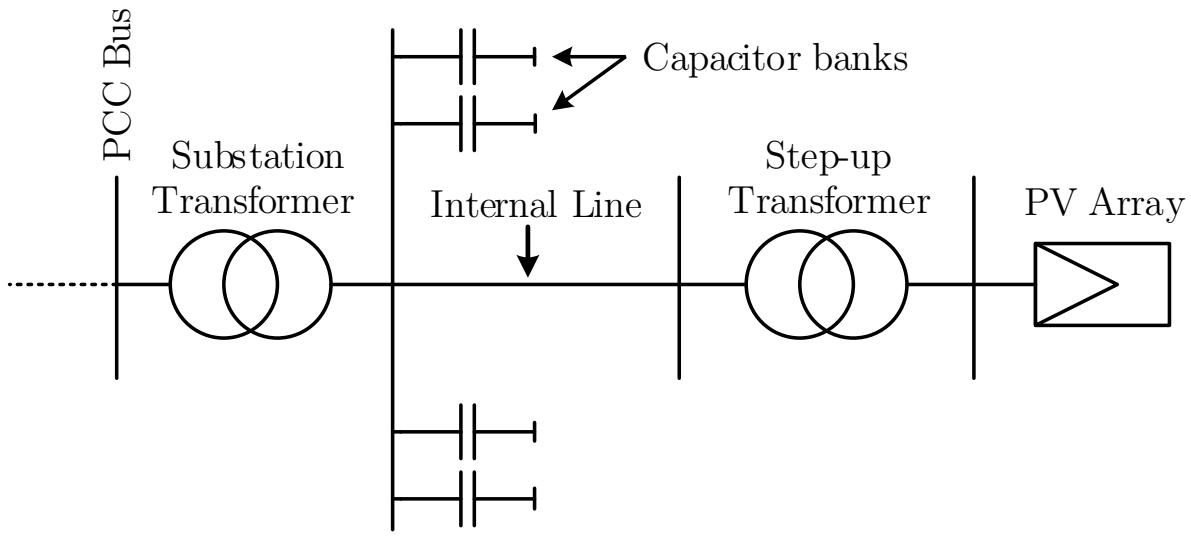

Figure 5.15: PV power plant model.

A control system is developed for the PV module in DPF to control the output power of the PV array to simulate a dynamic power output as illustrated by Figure 5.16. The control system can be set up to have certain number of power targets. The example in Figure 5.16 has three power targets, and a ramp-time can be set for each of these power targets. These ramp-times are the time it takes to linearly ramp the power up and down from the previous power target to the target power point.

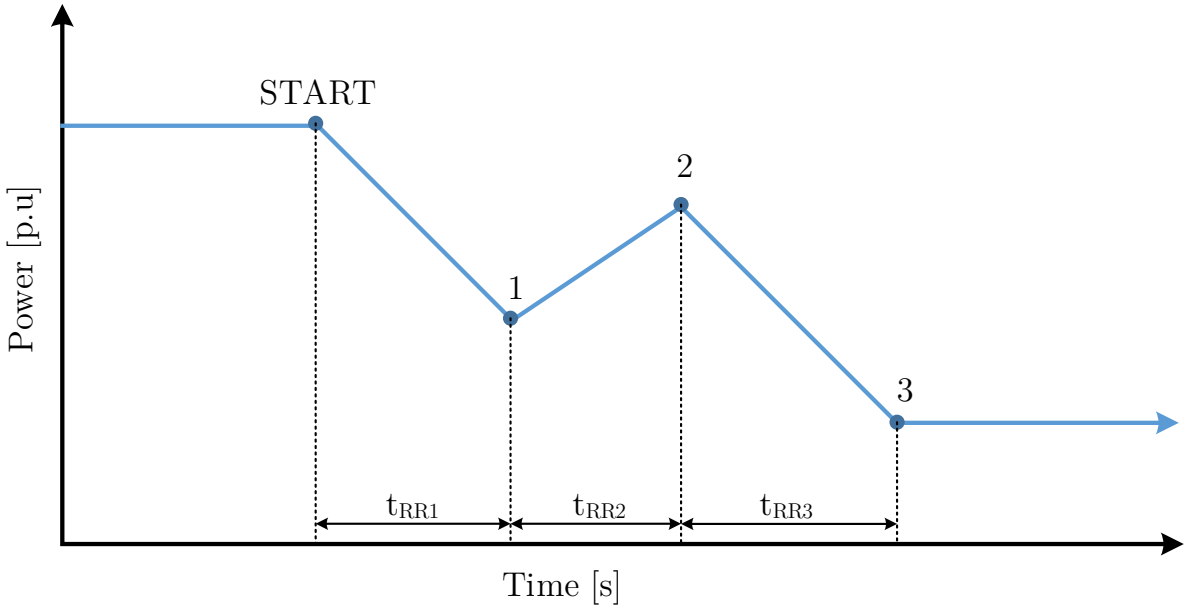

Figure 5.16: PV output control example.

Table 5.2 illustrates the user adjustable parameters for the control system in DPF. This specific case has three power targets but users are free to edit the control to add or remove power targets as required.

Table 5.2: Example of DPF PV power output controller parameters.

Parameter	Value	Unit
Ramp time - 1	30	s
Ramp time - 2	25	s
Ramp time - 3	35	s
Power target - 1	0.50	p.u.
Power target - 2	0.75	p.u.
Power target - 3	0.30	p.u.

5.8.3 Grid OLTC Transformer

An on-load tap changer is an internal mechanism which enables a transformer to change the ratio of its windings in order to achieve a range of different voltage ratios. The adding or subtracting of turns can be either on the high- or low-voltage side. OLTCs can take between 3 - 10 seconds, depending on the transformer design, to change taps [101].

The grid OLTC transformer is the transformer of importance for this case study since it will work in conjunction with the BESS to solve the problem of voltage instability. The PCC transformer also has an OLTC that can further improve the range of voltage support. For simplicity in this case study, its OLTC is fixed at a certain tap.

A standard 2-winding transformer module from the DPF library is used and is combined with an OLTC transformer controller provided in the DPF forums. The transformer has nine tap positions and has a linear selector. The controller has one input and one output and it is modified to include the intentional delay. Figure 5.17 is a diagram illustrating the OLTC control. The input reads the voltage level at a particular bus and checks whether it is within the allowed voltage range. Once the voltage is outside the dead-band, the intentional delay timer is initiated while the monitoring of the voltage continues. If the voltage is restored to stable levels, the delay timer resets. If the delay timer's value is reached, the controller signals the transformer for a tap increase or decrease. The function which signals the BESS (represented by the dotted block) will be discussed in Section 5.9.1.1 because it is part of the solution. A representation of the controller in action can be seen in Figure 5.18 where load is added to and subtracted from a bus.

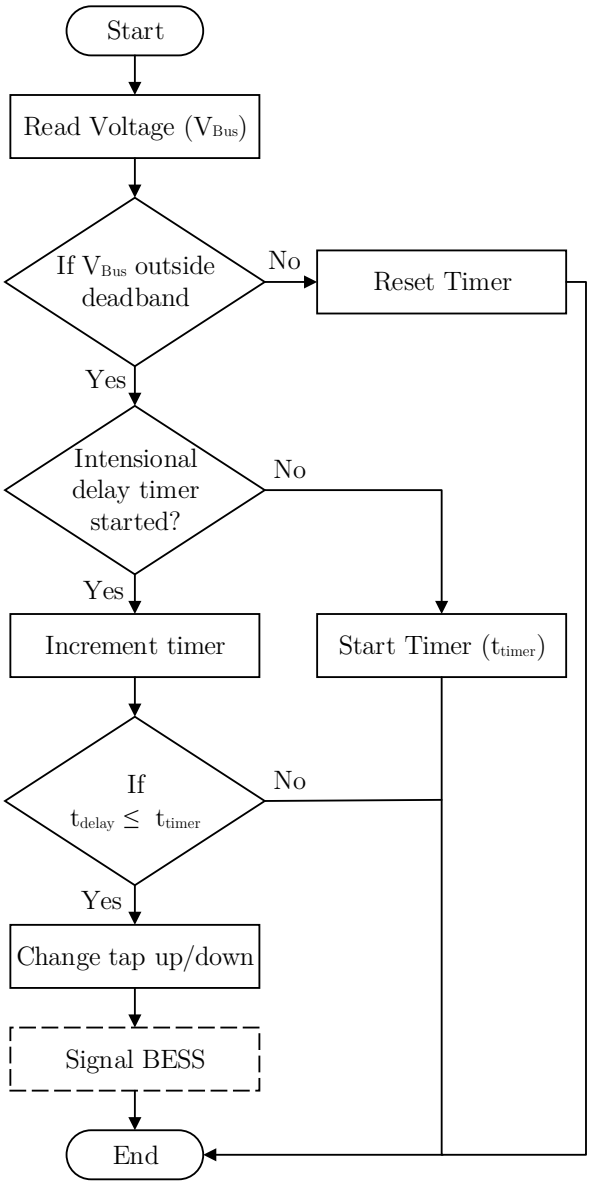

Figure 5.17: OLTC Controller.

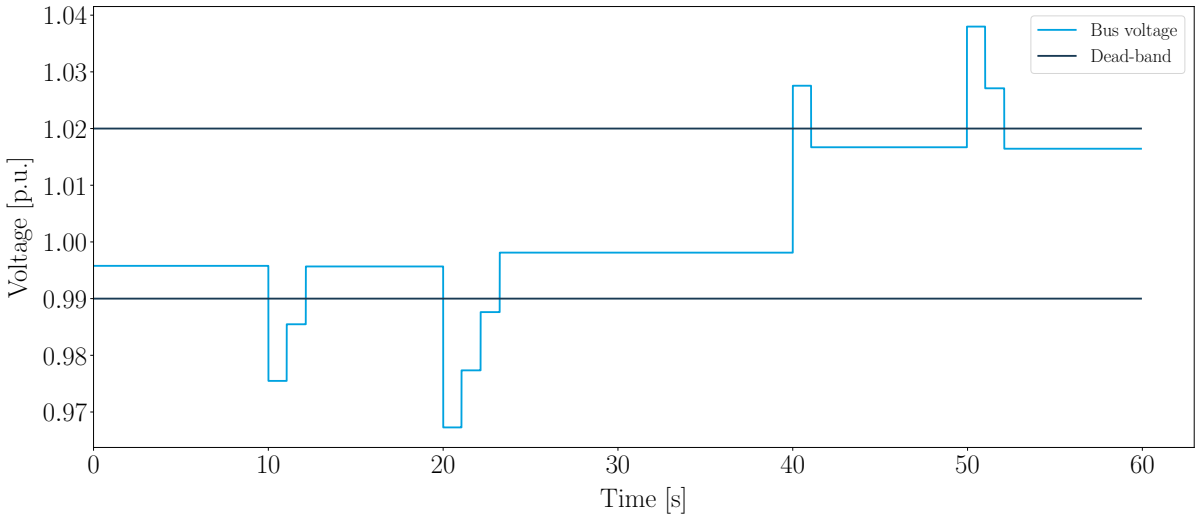

Figure 5.18: OLTC controller in action.

5.8.4 Weak Grid Characteristics

With the network model set up, the parameters defining the characteristics of the weak grid need to be determined in order to implement them in DPF. The magnitudes of these parameters will differ on a case to case basis. In this section, how the parameters for this case are calculated will be demonstrated.

The case currently being looked at has the following characteristics:

- SCR of 4.5 as seen from the PCC (less than 6 to 10 is considered weak)
- X/R-ratio for Z_{grid} of 0.5 (less than 1 is considered weak)
- Grid frequency: 50 Hz

The SCR and X/R-ratio are chosen such that the grid is strong enough to allow for the power loss condition of a 50 MW PV power plant but not for larger installed capacities. Using the information mentioned above, the grid parameters are calculated in the subsections that follow.

5.8.4.1 Per Unit Transmission Line Parameters

The cable parameters vary based on the cable used at a particular location. For this network model, the cable specification from a thesis by A. Gelieva [96] is used and can be examined in Table 5.3. The per unit values are calculated based on the method used by P. Kundur [95].

Table 5.3: Transmission line specifications.

Type	I_{max}, A	R, Ω/km	X, Ω/km	C, μF/km	ℓ, km
132 kV land cable, Al	600	0.02	0.2	0.25	50

As explained in Section 5.2.1, in the case of a short transmission line, shunt admittance can be neglected; thus, it is not calculated. Following the sequence of calculations below, the transmission line impedance can be calculated as follows:

Base impedance:

$$Z_{base} = \frac{V_{rated}}{I_{rated}} = 220\Omega$$

Per unit values:

$$X_{L.pu} = \frac{X_L \cdot \ell}{Z_{base}} = 0.0455 \text{ p.u.}$$

$$R_{pu} = \frac{R \cdot \ell}{Z_{base}} = 0.0045 \text{ p.u.}$$

Transmission line impedance:

$$Z_{TL} = \sqrt{R_{pu}^2 + X_{L.pu}^2} = 0.0457 \text{ p.u.}$$

5.8.4.2 Per Unit Grid Parameters

The SCR, as seen by the PCC looking into the grid, is 4.5. This determines the total impedance at the PCC looking into the grid. In order to determine the grid impedance parameters, the transmission line impedance needs to be deduced as it makes up part of the total impedance as seen by the PCC looking into the grid. The grid impedance is then divided into its respective parameters using the X/R-ratio of 0.5. One could just use the total impedance but separating the grid parameters from the transmission line parameter allows for more customisable simulations.

Impedance as seen by PCC looking into the grid:
Rewriting equation (5.15), the impedance seen by the PCC looking into the grid can be calculated as follows:

$$Z_{PCC} = \frac{U_{PCC}^2}{SCR \cdot S_{PV}} = 0.2 \text{ p.u.}$$

Deduct transmission line impedance:

$$Z_{grid} = Z_{PCC} - Z_{TL} = 0.1765 \text{ p.u.}$$

Inductive and ohmic parameters:
From equation (5.18) and (5.19):

$$X = \frac{|Z|}{\sqrt{1+(\frac{1}{xrr})^2}} = 0.079 \text{ p.u.}$$

$$R = \frac{|Z|}{\sqrt{1+xrr^2}} = 0.158 \text{ p.u.}$$

5.8.5 Grid Code Compliant 50 MW Case

The network parameters are chosen such that a case is created where a 50 MW PV installation can maintain voltage compliance at the PCC during a fault condition such as a short-circuit. During this fault condition, a sudden power loss occurs. A 49 MW load is introduced onto the grid bus to simulate a real world power draw from the PV power plant. The load and PV power production are kept at constant maximum values. This is done to simulate a worst case scenario for a sudden power or load loss. During these operating conditions, the OLTC transformer is operating at its rated tap position (position 0).

DPF is set to do an RMS simulation for a duration of 150 seconds. During this time, the PV power plant is operated at a steady-state power level of 50 MW. A power loss event is set to trigger at the 20-second mark. The simulation is set to a maximum time-step of 0.01 seconds. Figure 5.19 illustrates the simulation where gradual power loss occurs due to an event such as passing cloud cover. The passing cloud cover causes a change in irradiance which causes a fluctuating power output. A gradual decline in power occurs as the clouds move over the PV array. A sudden spike in the power output can be observed that typically represents a sudden increase in irradiance caused by light passing through spaces between the clouds. The figure also illustrates how the OLTC transformer waits as it assesses the voltage level and then adjusts it towards a preferred dead-band voltage level. The PV power output is represented as a per unit value of the maximum 50MW output. This simulation illustrates the OLTC transformer control.

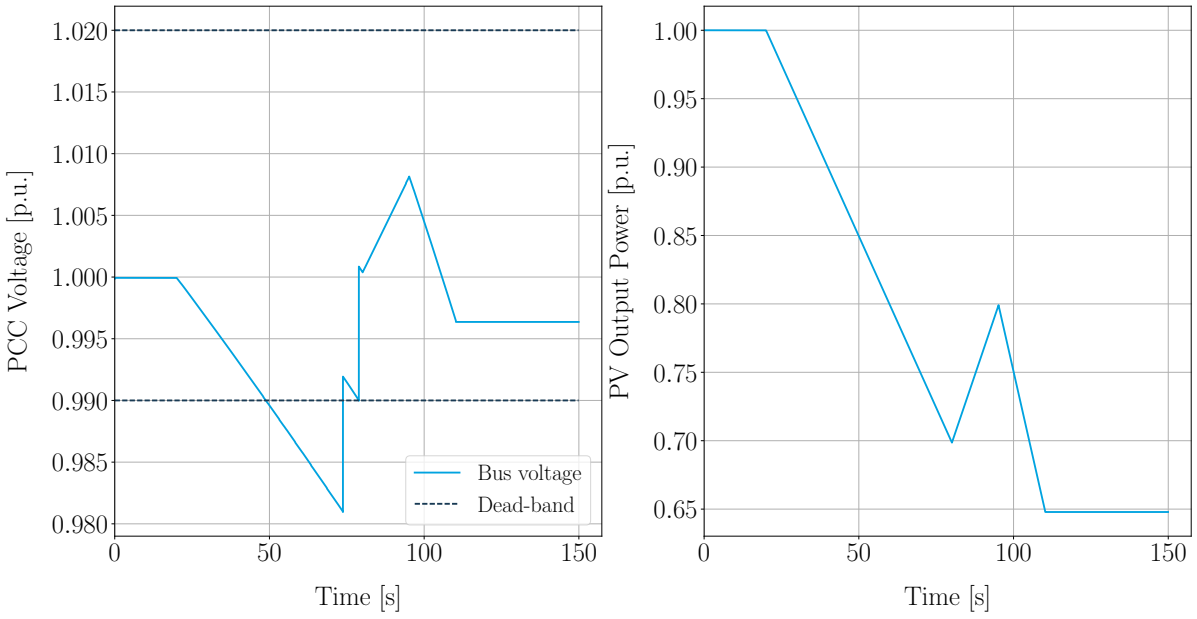

Figure 5.19: PCC bus voltage control using OLTC transformer.

Figure 5.20 illustrates a simulation where a sudden power loss occurs at the PV power plant. At the 20-second mark, one can see that the bus voltage does not drop below the minimum allowed limit of 0.9 p.u. After 30 seconds of assessment time, the OLTC transformer adjusts its taps to improve the voltage levels. On this particular weak network and based on these results, utility power producers will only be allowed about 50 MW of PV installation.

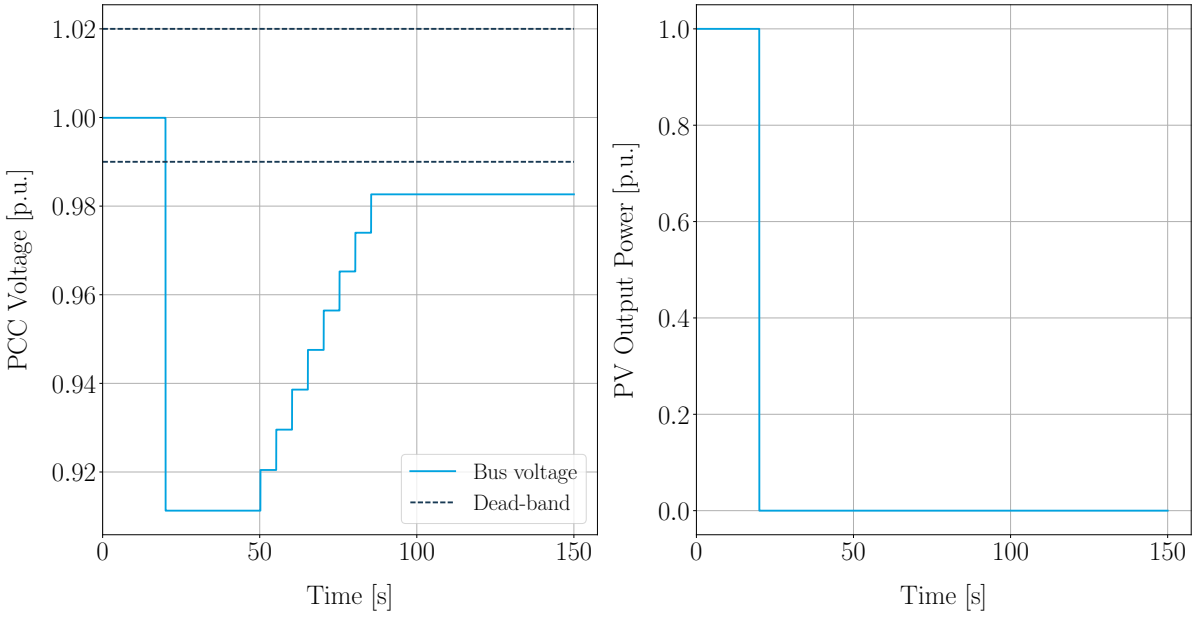

Figure 5.20: PCC bus voltage during sudden generation loss.

It is important to note that an immediate drop in voltage, as shown above, is not always to be expected since PV power plants can be connected at points on the network where generators with inertia exist. The inertia usually slows down the rate at which voltage drop occurs but the representation of the voltage level is still accurate.

5.8.6 Unstable 75 MW Case

The PV installation is increased to 75 MW with an increased load of 74 MW. 1 MW is assumed as losses for the system and network. The network parameters are kept the same. Figure 5.21 illustrates this sudden loss of generation and it is noticed that the voltage levels drop below the required operating voltages of 0.9 p.u. After the 30-second intentional transformer delay, the first tap change occurs. The OLTC is capable of completely restoring the voltage to an acceptable level but not quickly enough to prevent operating conditions outside those specified in the grid code. Furthermore, the capacitor banks installed at the substation can provide further voltage support if required. These are not used in this study as the aim is to provide all the required support with the BESS because it provides a return on investment in terms of energy delivered.

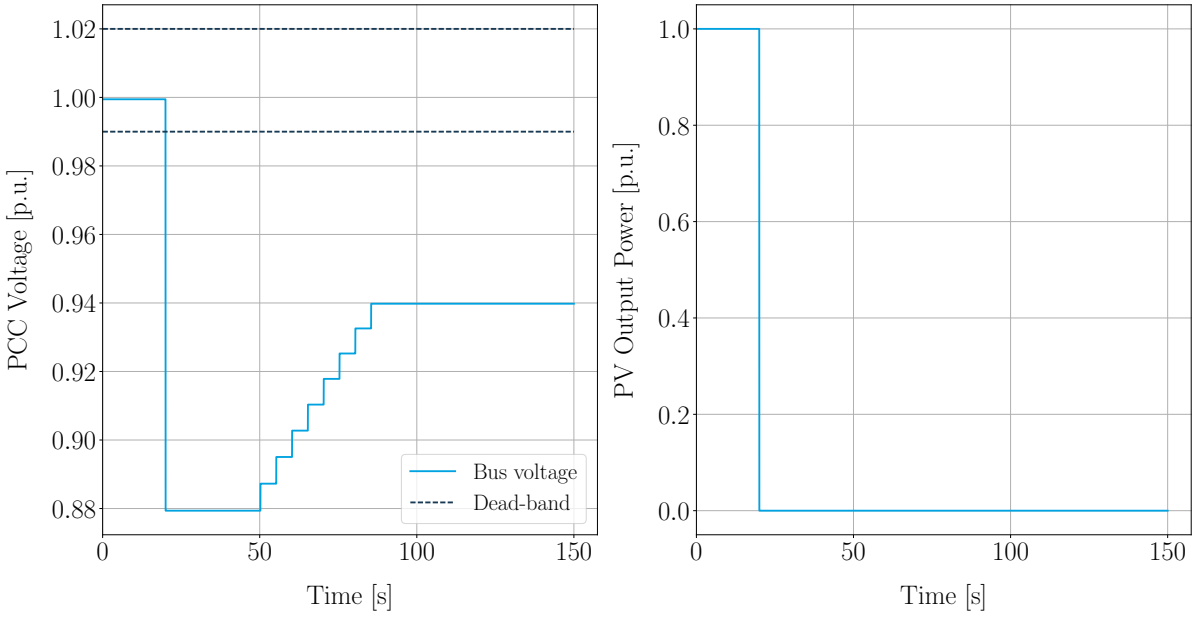

Figure 5.21: PCC bus voltage during sudden generation loss.

RPPs have agreements with the network service provider, ESKOM, according to which they are remunerated for each unit of energy delivered. Sometimes unstable network operations can occur which are out of the RPP's control such as the sudden loss of load on a weak network. In a case such as this, a sudden voltage rise can occur leading to unstable operating conditions. RPPs in the PV industry tend to operate inverters near the rated specifications; thus there is no spare capacity in the inverters to absorb the required reactive power to lower the voltage levels. RPPs are required to curtail the active power delivery in order to assist in stabilising the grid. The inverters will have to curtail the PV power within the required time of two seconds in order to restore the voltage within the

normal operating range of 1.0985 p.u. Figure 5.22 illustrates the simulation of a sudden load loss on this particular network representation.

Installing a BESS can allow the RPP to absorb some, if not all, of the active power which needs to be curtailed. Since RPPs are compensated for the energy lost during curtailment, the BESS energy can be discharged at a later stage to provide even more energy.

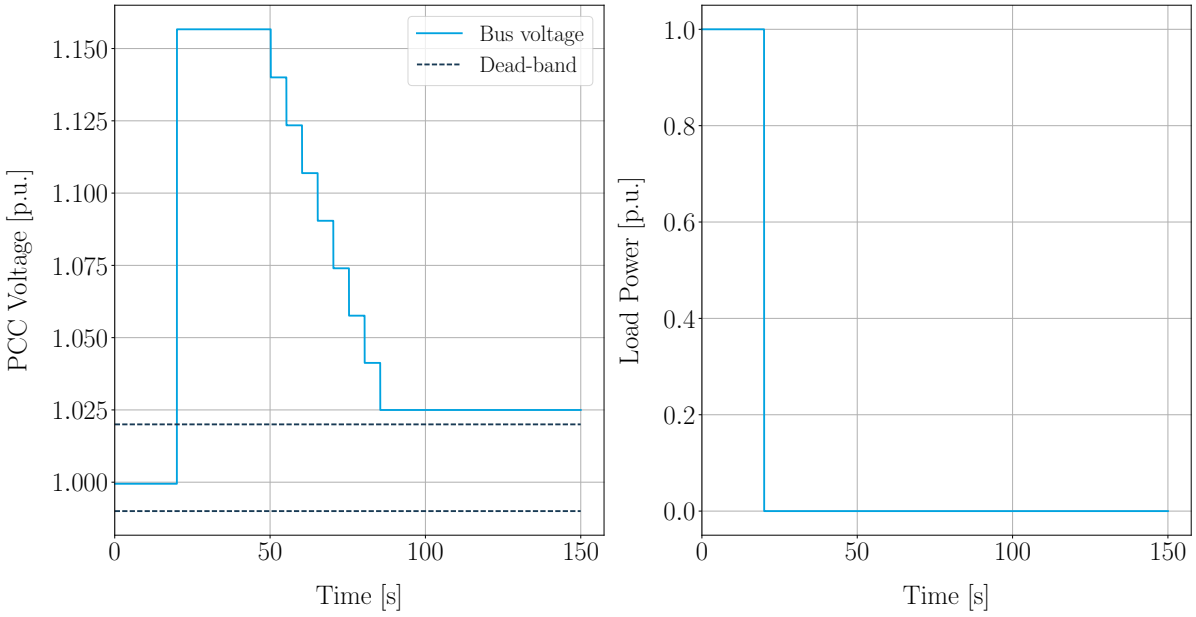

Figure 5.22: PCC bus voltage during sudden load loss on weak network.

5.9 Network Solution

A solution is proposed where a BESS provides the needed active power to address the voltage jumps when a sudden loss of generation is experienced. The solution includes battery storage paired with an OLTC transformer. During a power loss event, the intentional delay in the OLTC transformer prevents the transformer from rectifying the voltage fast enough to return to normal operating conditions. The intention with the solution is to provide active power during the intentional delay of the OLTC, maintaining the voltage at the PCC within the normal operating condition specified in the grid code. As the OLTC transformer restores the voltage to a more appropriate value, the BESS ramps down, withdrawing active power support.

5.9.1 System Control Model

The control system illustrated in Figure 5.23 describes the interaction between the controllers and the network components. The voltage of the grid bus is monitored by the OLTC transformer controller whilst the BESS controller monitors the PCC for abnormal voltage conditions. The BESS is placed at the PCC because, according to the constraints in the renewable grid code, utilities need to concern themselves with the required the voltage levels at the PCC.

If a voltage drop or rise occurs, the OLTC controller will assess the voltage levels before instructing the transformer to adjust its taps. In the case of an extreme voltage drop, where the voltage levels reach abnormal operating conditions, the BESS controller will initialise the BESS. The BESS supplies energy as long as it possibly can or until the OLTC controller signals the BESS controller that acceptable voltage levels have been reached. At this point the BESS will start ramping down.

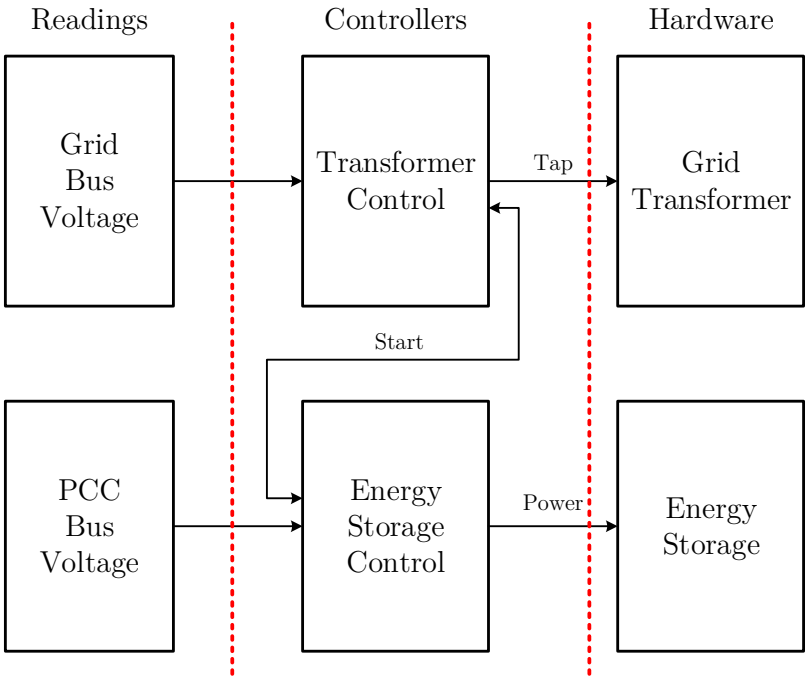

Figure 5.23: Control system interaction with grid components.

5.9.1.1 OLTC Transformer Controller

The standard OLTC transformer controller is modified to have a second output. The second output is the communication line between the OLTC controller and the BESS controller. The OLTC controller has to signal the BESS controller to indicate when the ramp-down sequence can be initiated. The BESS controller responds with a reset signal once the ramping sequence has ended.

The OLTC controller has 6 adjustable parameters and can be seen in Table 5.4. These parameters are the actual parameters used for the simulation cases. In a study by Sichwart *et al.* [100] it is suggested that the first tap change take 30 seconds to complete due to an intentional delay. The tap change delay can be anything between 3 - 10 seconds based on the transformer design. For this test case, a 5-second delay is chosen based on the study by Sichwart [100]. The assessment delay parameter refers to the intentional delay which the OLTC uses to determine whether the adjustment of taps will be required [91, 92, 101]. The maximum and minimum allowed voltages refers to the range in which the OLTC will not change taps. If the voltage deviates outside these limits, the controller will commence its assessment of the voltage for possible tap changes. The OLTC controller also has a ramp-down trigger voltage. At this voltage point or higher, the controller waits for its next upward tap-change before signalling the BESS controller to initialise its ramp-down sequence.

Table 5.4: Transformer controller parameters

Parameter	Value	Unit
Tap changer delay	5	s
Assessment delay	30	s
Max allowed voltage	1.02	p.u.
Min allowed voltage	0.99	p.u.
Ramp-down trigger voltage	0.91	p.u.
Max tap position	8	-
Min tap position	-8	-

5.9.1.2 BESS Controller

The BESS controller is designed to receive two input signals: one with the voltage level from the PCC and the other with a signal to initiate the ramp-down sequence. The ramp-down sequence is based on an integrator block which can be adjusted to ramp down the power based on the user's requirements. The BESS controller signals the OLTC controller once the ramping sequence is completed. The BESS controller has 5 parameters which can be adjusted as seen in Table 5.5. The ramp-down time is the time it will take the BESS to ramp down from its maximum output power to its minimum output power. The voltage trigger level determines when the BESS will activate in order to provide the emergency backup power. The start-up delay is a parameter introduced to simulate the small delay after the power loss occurs when the BESS initialises. This delay typically includes the battery response time (in the order of 20 milliseconds according to Carnegie *et al.* [17]), controller delays and communication delays. Since there is no generic time, the value is selected with confidence to be 500 milliseconds.

Table 5.5: Energy storage controller parameters

Parameter	Value	Unit
Ramp-down time	30	s
Start-up delay	0.5	s
Maximum power	1.0	p.u.
Minimum power	0.0	p.u.
Start-up trigger voltage	0.91	p.u.

5.9.2 Compliant 75 MW Case

Figure 5.24 shows the PCC voltage of a 75 MW PV installation with a 20 MW BESS to support it. The figure also illustrates the BESS output power profile as the power loss event occurs. It can be seen that the transformer and the BESS controller work together to mitigate the voltage drop by injecting active power into the network during the transformer's assessment delay. The implemented parameters of these controllers can be examined in Tables 5.4 and 5.5 in the previous sections. There is a small delay after the

power loss occurs when the BESS initialises. The BESS provides nearly 0.04 p.u. voltage support until a tap change occurs above the ramp-down trigger voltage. The OLTC is able to bring the voltage up to a stable 0.94 p.u level whilst the BESS keeps the whole process within normal operating conditions.

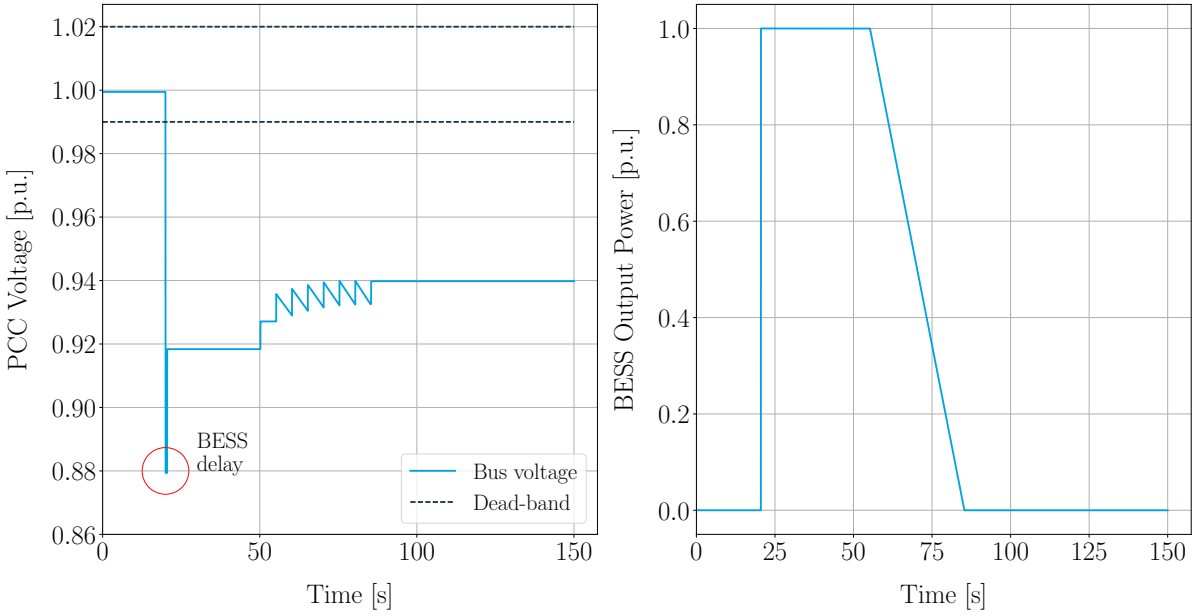

Figure 5.24: Compliant bus voltage during sudden generation loss.

Figure 5.25 illustrates a solution to this case where sudden load loss occurs during maximum power generation. It is seen that the active power is curtailed at the 20-second mark in order to stabilise the voltage at the PCC bus. The curtailment can happen in one of two ways: curtailment by the PV inverters or active power absorption via the BESS. From this case, it can be seen that the PV power output has to be curtailed by 50% in order to stabilise the voltage below the required 1.0985 p.u. However, the BESS and its power system equipment are rated at 20 MW (when no efficiencies have been taken into account); thus, the PV inverters will have to assist in curtailing the majority of the power. Furthermore, Reddy *et al.* [18] show that batteries can only be charged at a fraction of their discharge rates. Based on the current SOC of the battery, the charge rate can be higher, but given that the batteries should be on standby for a sudden power loss situation, the SOC will typically be high. From the figure it is evident that RPPs can compensate for sudden load losses.

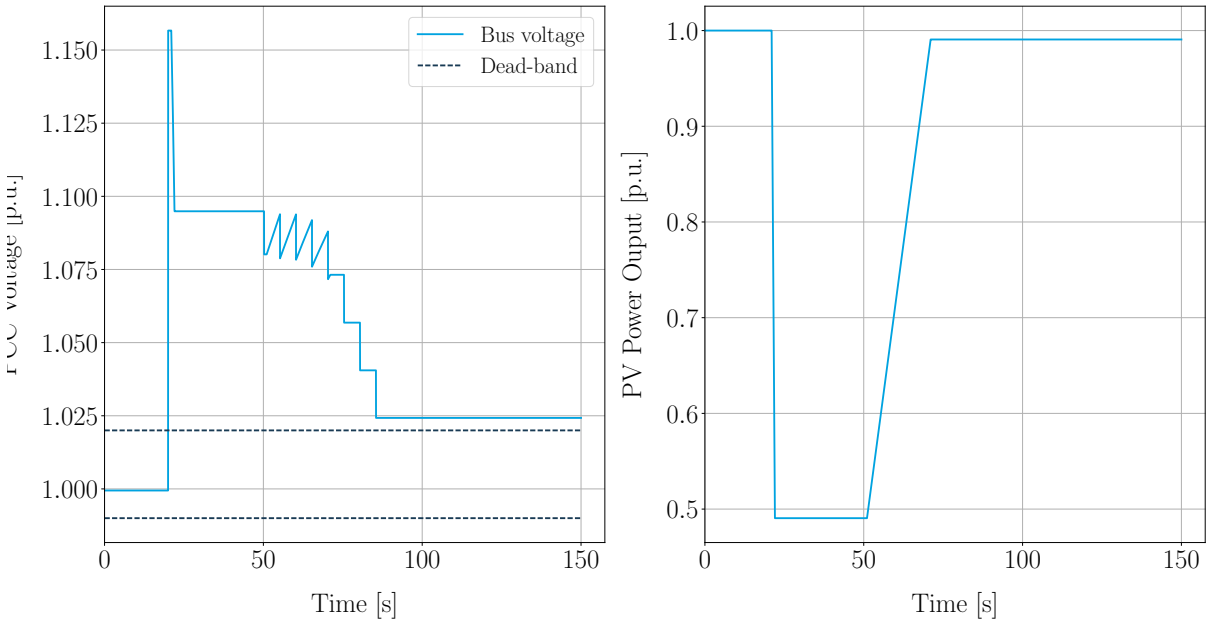

Figure 5.25: Compliant bus voltage during sudden load loss.

5.9.3 Sizing of BESS

As seen from the study case, there are many different variables such as the grid characteristics, the renewable energy grid code, transmission line specifications and the power system equipment specifications that can influence the resulting BESS specifications.

The peak power requirement is determined by inspecting the resulting voltage gain at the PCC when active power is delivered by the energy storage module. Since the voltage at the PCC varies as the connected load and PV power output varies, the problem can be simplified by setting these variables to constant values. The constants are determined by setting up the worst case scenario where the PV power plant output and the load are both at a maximum. In a case like this the maximum power loss occurs while servicing a maximum load. Sizing the peak power specification for such a case will provide ample power for other potential power loss situations. From the test case, the required battery power output (P_{bat}) is found to be 20 MW. Considering the inefficiencies of the power conversion unit (PCU), the BESS power requirement (P_{BESS}) can be determined by the following expression:

$$P_{BESS} = \frac{P_{bat}}{\eta_{PCU}}, \tag{5.22}$$

where η_{PCU} represents the PCU efficiency. Using a PCU efficiency of 90%, the peak power results in 22.2 MW.

When knowing the peak power, one requires the output profile from the battery storage in DPF to determine the required energy specification. The profile; however, varies based on many different factors such as the ever-changing voltage at the PCC, the parameters of the OLTC transformer- and the BESS controller. Furthermore, the voltage at the PCC is dependent on the varying power output from the PV power plant and the varying load

connected to it. By fixing the power output and the load to constant values, as mentioned before, a worst case scenario is created for which it is easy to determine the BESS energy requirement. The battery output profile for the compliant 75 MW case is illustrated in Figure 5.26.

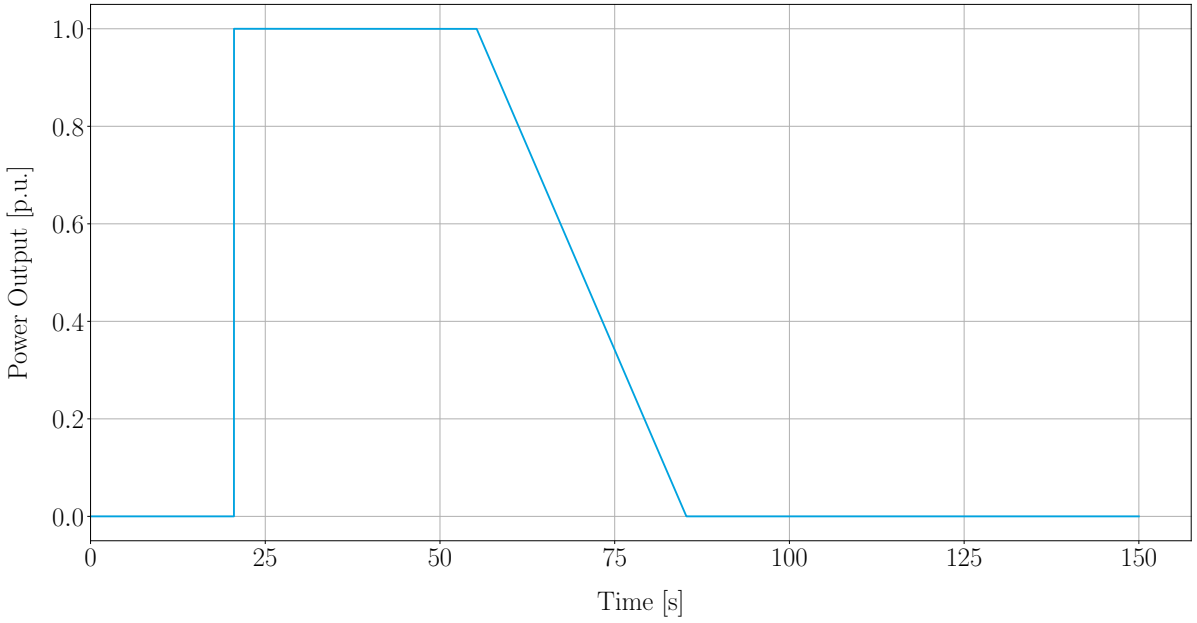

Figure 5.26: Battery power output profile.

Using Figure 5.26, the required battery energy (E_{bat}) can be determined by integrating the battery power output profile (P_{output}):

$$E_{bat} = \int_0^t P_{bat}(t)\ dt,\ P_{bat} \geq 0. \tag{5.23}$$

The BESS energy specification (E_{BESS}) is determined by taking into account the losses such as PCU efficiency and applying minimum and maximum SOC constraints. E_{BESS} can be determined using the following expression:

$$E_{BESS} = \frac{E_{bat}}{\eta_{PCU} \cdot (SOC_{max} - SOC_{min})} \tag{5.24}$$

Using expressions (5.23) and (5.24) with $SOC_{max} = 100\%$ and $SOC_{min} = 20\%$, the required BESS energy is determined to be 385 kWh.

5.9.4 Battery Recommendation

Based on the required operation of the BESS in this solution; a lithium technology, such as a $LiFePO_4$/graphite cell, is recommended. This chemistry is the most thermally stable of all the lithium cells that use graphite as negative electrode and it is capable of high rates of discharge. In Formula 1, A123 Systems helped to introduce hybrid power to the

racetrack by developing a $LiFePO_4$ cell, called AHR18700M1*Ultra* which is designed for extremely high-power applications. [18]

5.10 Conclusion

In this chapter, the installation of larger PV systems on weak networks is investigated. Weak network parameters are determined and simulated in DIgSILENT PowerFactory and it is found that these networks restrict the installation size of PV power plants since voltage compliance at the PCC cannot be maintained as stipulated in the grid code. OLTC transformers allow the voltages to be restored to an acceptable level but not within the required response times given in the grid code.

A BESS is proposed to assist the transformer in achieving grid code compliance. The idea is that batteries will deliver the missing active power during the transformer's intentional assessment delay. A controller is developed for the BESS as well as the on-load tap changer of the transformer. The controllers work in conjunction with each other to mitigate abnormal voltage conditions at the PCC within the specified response times as listed in the grid code. Although it is not the focus of this thesis, sudden load loss conditions are also examined to see if grid compliance can be maintained and to show that batteries can assist in this area as well.

It is found that stable voltage conditions are possible using a BESS if the system is sized such that it can accommodate the worst case scenario. It is important to remember that there are many variables when it comes to simulations such as network parameters, specifications and controllers of power system equipment, and power plant specifications and controllers. These variables can determine whether ot not BESS should be considered. How a BESS can be sized from the battery storage output profile to provide sufficient energy is also discussed.

In Chapter 7 the costs of this solution will be discussed which will be a determining factor for utilities when considering a BESS as a solution.

Chapter 6

Peak Load Shaving

The network service provider (NSP) has identified developed neighbourhoods in which distribution feeders are operating near or above the rated maximum specifications. Upgrading the distribution substations is very expensive particularly since no further expansion will occur in these neighbourhoods. Batteries are applicable in this situation since they have the ability to store energy for use during peak hours.

Over the past few years battery energy storage system (BESS) costs have declined and will continue to do so [102]. Battery systems can serve as an ancillary service by assisting with stability in terms of frequency [103, 104], peak load shaving [6, 11, 12, 14] and power shifting [105, 106]. The service of interest in this chapter is peak load shaving. The BESS charges during off-peak hours and provides peak load shaving by discharging the energy as required during peak hours. This ensures that the deployed distribution hardware is operating within its rated specifications.

The sizing of the BESS for peak load shaving requires optimisation. In a study by Venu *et al.* [14] and Telaretti *et al.* [13], the BESS is sized such that target peak power is never exceeded. This is a sufficient sizing strategy in which the BESS is sized to include the outliers; one sizes for the worst case scenario. However, this strategy can result in a very costly, oversized BESS.

A more economical sizing strategy is required in which anomalous power requirements are excluded from the sizing of the BESS. This strategy is based on the assumption that the distribution feeder can withstand the occasional peak or is allowed to disconnect at extreme peak conditions. Statistical tools exist that are capable of identifying outliers but it can become a tedious process to condition the data and determine the BESS specifications. It is proposed that a tool be created that conveniently implements a sizing strategy using the statistical tools. A tool such as this can also prove useful to business owners trying to reduce their high peak power consumption in an attempt to reduce their feeding tariffs.

In this chapter, a sizing strategy, based on a worst case scenario approach, is investigated and applied to actual feeder data. A statistical tool called Cook's distance that identifies influential outliers is investigated. This tool is integrated into the investigated sizing strategy and the results are compared to those ofthe original strategy. A tool is created in Python which automates the process of analysing feeder profiles and the sizing of the BESS.

6.1 Peak Load Shaving Using BESS

6.1.1 Feeder Load Characteristics

The NSP is currently experiencing problems where developed neighbourhoods have peak loads exceeding the feeder specifications. The solution being considered includes the sizing of a BESS to provide the required energy to reduce the peaking of the distribution feeders. Peak loads are not unique to distribution feeders but are also a concern for larger businesses. Businesses could benefit from a BESS by reducing the energy consumed within a certain feeding tariff. The BESS can also serve as an uninterrupted power supply for critical operations.

The idea is to create a tool that uses the load profiles of a feeder or the connection of business premises, to estimate the required BESS size. The strategy discussed in this section is that of Venu *et al.* [14]. To explain the process of sizing the batteries, actual feeder data from 2014 is used. The data consists of hourly readings spread over 24-hour days for 365 days. Figure 6.1 illustrates the feeder profile for an entire year where the highest peaks are during the winter season. A target peak power line that represents the aimed peak power for the feeder is illustrated.

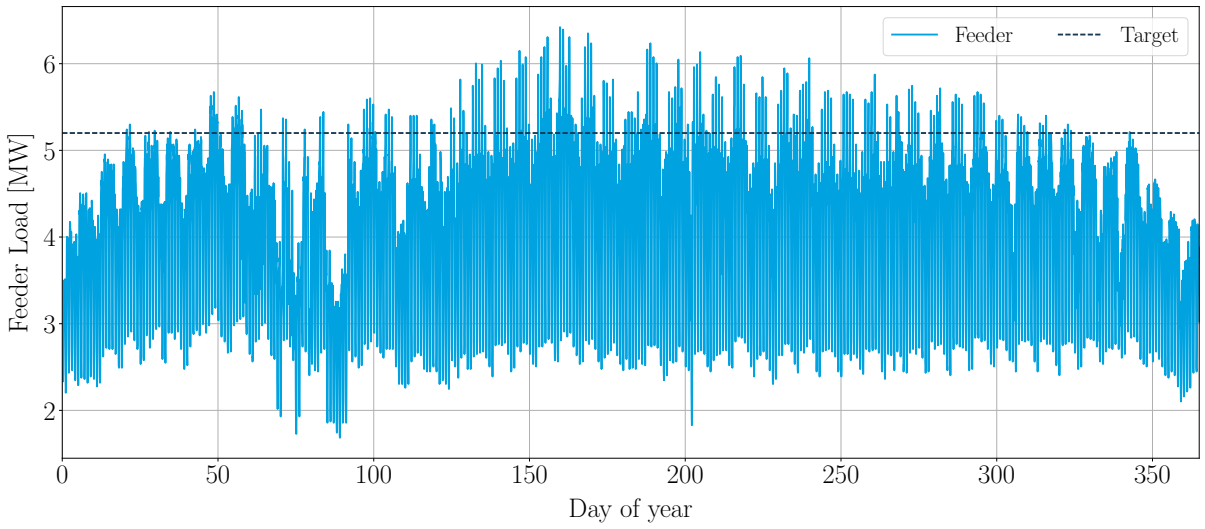

Figure 6.1: Feeder load data for 2014.

Figure 6.2 is the corresponding load distribution curve of the feeder profile before the BESS is applied. In this figure 100% represents a total of 8760 hours (365 days). It can be seen that the peaks exceeding the target power only do so 6.61% of the time. When taking a closer look at the daily feeder profiles, it is found that the target power is typically exceeded between 17:00 and 20:00.

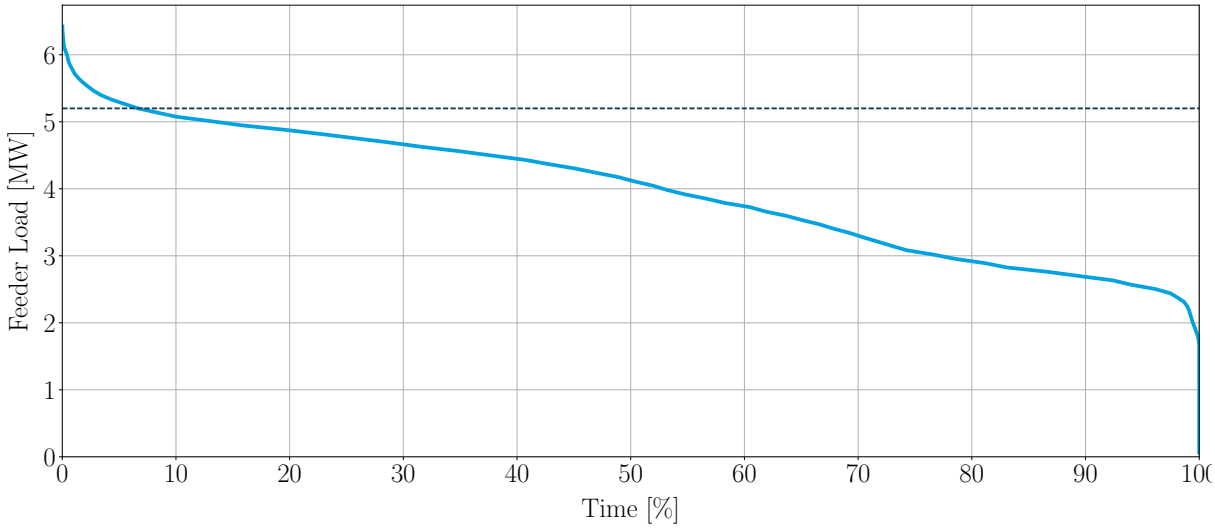

Figure 6.2: Load distribution curve for feeder profile.

6.1.2 Battery Storage Sizing

The size of the BESS is determined mainly by two parameters: peak power and maximum energy. The values of these parameters depend primarily on the desired peak power of the feeder. This can be specified either as a percentage reduction (σ_{red}) or as a desired power level (P_{des}). Applying the desired power level to the feeder, the required battery power output (P_{bat}) can be determined using expressions (6.1) and (6.2). P_{peak} represents the peak power that the feeder experiences.

$$P_{bat} = \sigma_{red} \cdot P_{peak} \tag{6.1}$$

$$P_{bat} = P_{peak} - P_{des} \tag{6.2}$$

Losses with regard to power and energy occur when batteries charge or discharge through the power conversion unit (PCU). Taking these losses into account, the required BESS power (P_{BESS}) can be represented by expression (6.3), and the losses are represented by an overall efficiency (η_{PCU}).

$$P_{BESS} = \frac{P_{bat}}{\eta_{PCU}}. \tag{6.3}$$

As can be seen in Figure 6.1, a peak power of 6.42 MW was experienced on the 9th of June 2014. The desired power level for the feeder is chosen to be 5.2 MW and is represented by the dotted line; thus, the feeder peak power should not exceed the 5.2 MW-mark. From expression (6.2), the required power is $P_{bat} = 1.22\ MW$. Taking into account an assumed discharge efficiency of $\eta_{PCU} = 90\%$ and using expression (6.3), the required BESS power is calculated at $P_{BESS} = 1.36\ MW$.

The battery energy requirement is determined from the daily energy requirement in order to keep the distribution feeder from reaching its peak level. The energy requirement

is determined by calculating the area above the target power line in Figure 6.1. This calculation is represented by the following expression:

$$E_{bat}^{i} = \int_{0}^{24} (P_{load}^{i} - P_{des})dt,\ P_{load}^{i} \geq P_{des}, \tag{6.4}$$

where P_{load} is the power at a certain hour of the day and i is the number of the day in the dataset. Venu *et al.* [14] suggest that the required battery energy is the maximum required energy of any day and is expressed by the following:

$$E_{bat}^{max} = \max\left\{E_{bat}^{1}, E_{bat}^{2}, ..., E_{bat}^{n}\right\} \tag{6.5}$$

where n is the number of days in the data set. When the maximum required energy output for the batteries is known, the energy specification for the BESS (E_{BESS}) is obtained using the following expression:

$$E_{BESS} = \frac{E_{bat}^{max}}{\eta_{PCU} \cdot (SOC_{max} - SOC_{min})} \tag{6.6}$$

where SOC_{min} and SOC_{max} represent the minimum and maximum state-of-charge respectively. These two parameters are included because energy storage systems are operated within these parameters to extend battery service time.

Referring to the example case, when applying expression (6.4) to the feeder profile, the required battery profile is produced and is illustrated in Figure 6.3. Using expression (6.5), the required battery output energy is determined as $E_{bat} = 8.54\ MWh$. Applying a PCU efficiency of 90%, a maximum SOC of 100% and a minimum SOC of 20%, the required BESS energy can be determined from expression (6.6) as $E_{BESS} = 9.49\ MWh$.

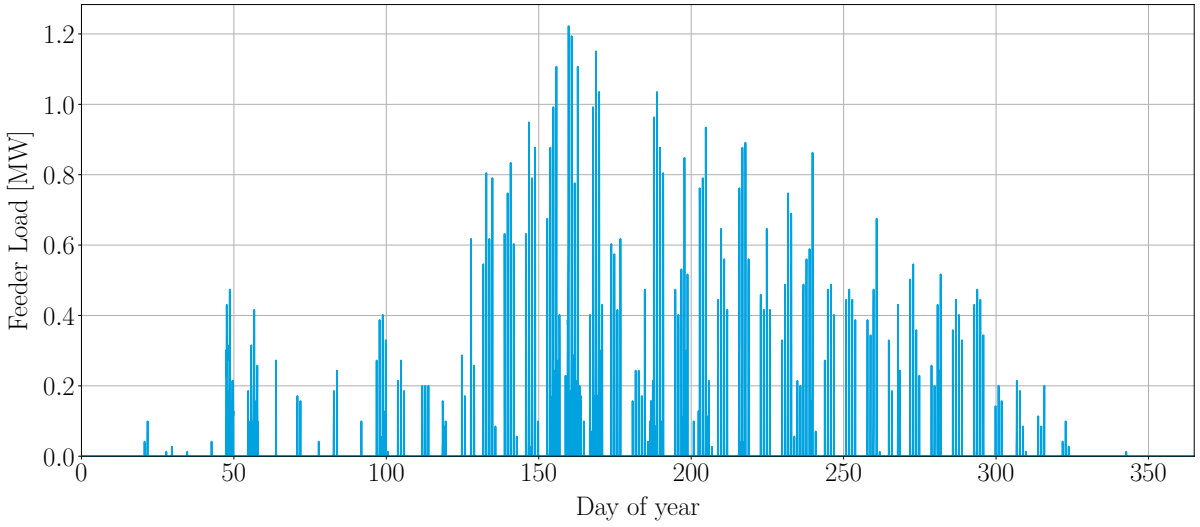

Figure 6.3: Required battery profile.

Applying the battery profile as illustrated above, the load distribution curve can be re-calculated in order to see if the BESS support will be sufficient. Figure 6.4 illustrates the new load distribution curve and after examination, one can see that the peak power has been restricted to stay below the 5.2 MW-mark.

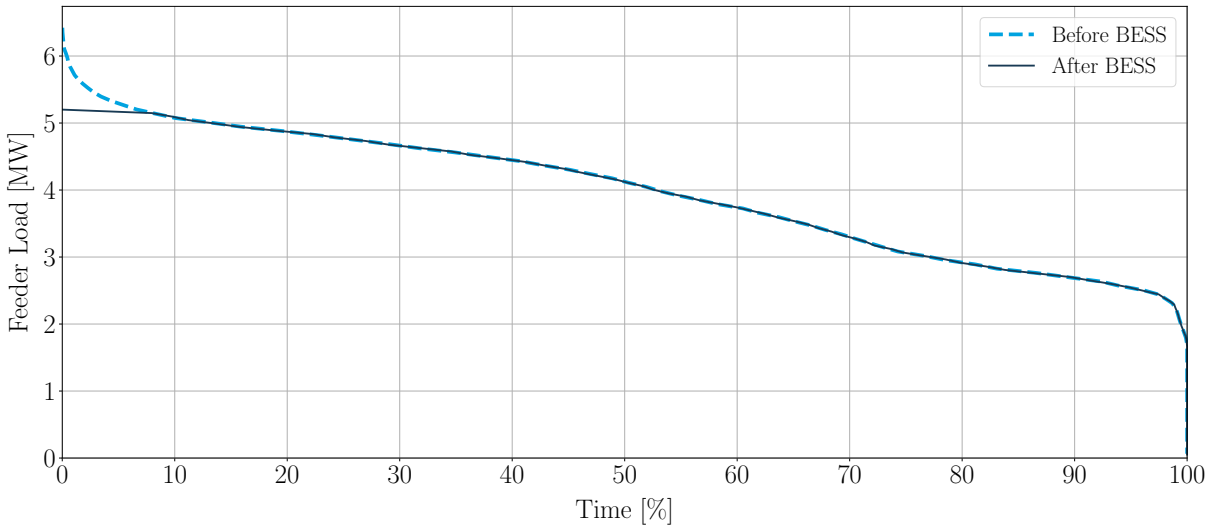

Figure 6.4: Load distribution curve after the BESS is applied.

6.2 Optimal Battery Sizing

In literature, BESSs are typically considered for peak load shaving to postpone expensive upgrades [6, 11, 12, 14]. If these feeders are operating close to the rated specifications, are the battery systems optimally sized to ensure a good price to performance comparison? In other words: if the feeder can afford to peak or operate near its rated specification a few times per year, can the battery system size be reduced considerably?

A statistical tool called Cook's distance [107] is used to identify anomalous data that has a great influence on the resulting regression fits. The idea is to identify abnormal days of energy consumption or peak power levels in an attempt to reduce the BESS requirements.

6.2.1 Cook's Distance

Cook's distance is a means with which one can assess the influence individual observations have on the estimated coefficients in a linear regression analysis [107, 108]. It is used to assess outlying observations because these outliers can cause one to misinterpret data and fail to capture important characteristics of the data. When considering separated data points, it is important to notice that these points can have a strong influence on the statistical model. For example: deleting outliers from the regression model can yield very different results. These unusual cases sometimes consist of both outliers and high leverage points which influence both the slope and intercept of the model [109]. Cook's distance, D_i, of the i^{th} observation is represented by the following expression:

$$D_i = \frac{r_i^2}{k+1} \times \frac{h_i}{1-h_i} \tag{6.7}$$

where h_i is the hat-value for each observation, r_i is the studentised residual and k is the number of predictors. In the expression, the first fraction measures the discrepancy (or distance) and the second fraction measures the leverage.

M. Lovric [108] states that it is important to remember that Cook's distance is not a test statistic and should not be used by itself to accept or reject cases. It merely serves as a indication of anomalous cases that are extramural to the experimental protocol. It could also point to an important case in the analysis. Cook's distance does not distinguish between these different possibilities.

6.2.1.1 Relevant Terminology

Outliers

Univariate outliers are observations that are unconditionally unusual with regards to their X- or Y-values and are not necessarily regression outliers. A regression outlier, refers to an observation that has an unusual Y-variable conditional on its dependent X-variable. [109]

Leverage

Leverage is an observation that has an unusual X-value causing it to have leverage on the regression line. An example is when the X-value is far from the mean of X. The further away it is from the mean of X, the more influence it has. However, high leverage does not necessarily mean high influence. [109]

Influence

An observation will only strongly influence the regression line when it has an outlier in terms of the Y-value and has high leverage. In other words, it must have an unusual X-value with an unusual Y-value for the given X-value. [109]

Hat-values

The hat matrix is defined by M. Lovric [108] as the matrix that is used to convert values from the observed variable into estimations obtained using the least square method. The diagonal elements of the hat-matrix are called the leverage or hat-values (h_i) and these elements describe the influence each of the observed values has.

According to M. Lovric [108] and W.G. Jacoby [109], hat-values are a common way of measuring the potential leverage the Y-value has on the estimated values. In a simple regression, the hat-value measures the distance from the mean of X. In a multiple regression, they measure the distance from the centroid of all the X-values.

Studentised Residuals

The strategy behind the studentised residual includes deleting the observations one at a time whilst refitting the regression model each time on the remaining observations. The fitted values and observed response values are compared based on the models with the ith observation deleted. From the comparison, deleted residuals are produced which, through

standardisation, produce residuals. The studentised residual is simply a deleted residual, d_i, divided by its estimated standard deviation, $s(d_i)$, and is illustrated by equation (6.8).

$$r_i = \frac{d_i}{s(d_i)} = \frac{e_i}{\sqrt{MSE_i(1-h_i)}}. \tag{6.8}$$

Equation (6.8) also shows an equivalent expression where the ordinary residual, e_i, is divided by a factor. This factor is based on the mean square error, MSE, of the estimated model with its i^{th} observation deleted, and the leverage, h_i. [110]

6.2.1.2 Examples of Influence and Leverage

Figure 6.5 illustrates an outlier with an unusual Y-value. The example shows that the outlier has little influence on the regression line since its X-value is in the middle of the X-range.

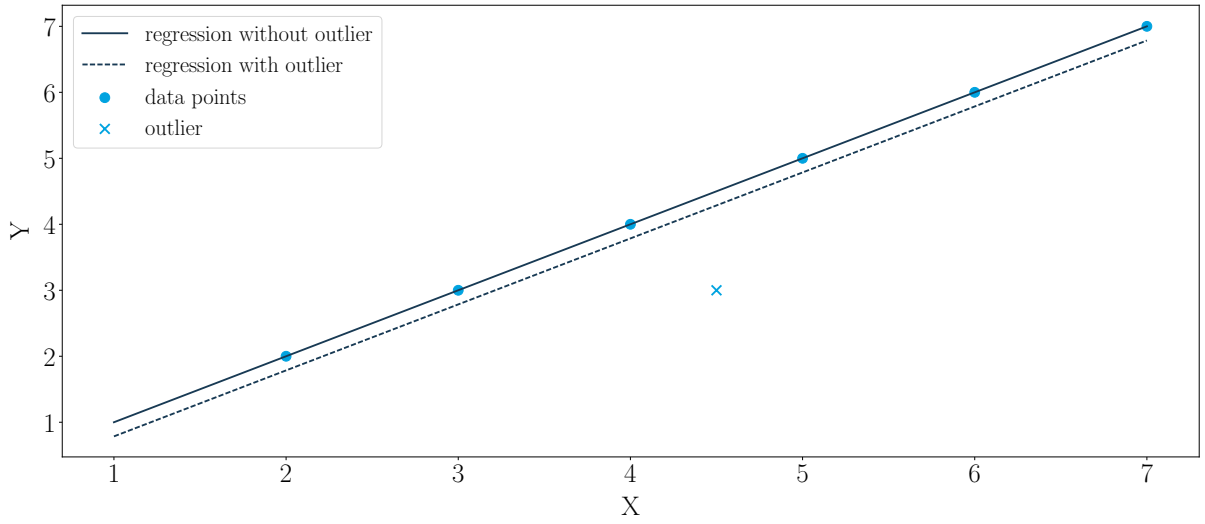

Figure 6.5: Outlier with little influence.

Figure 6.6 illustrates an outlier with an unusual X-value but its Y-value is in line with the general pattern. The example shows a case of high leverage which has little influence on the regression line.

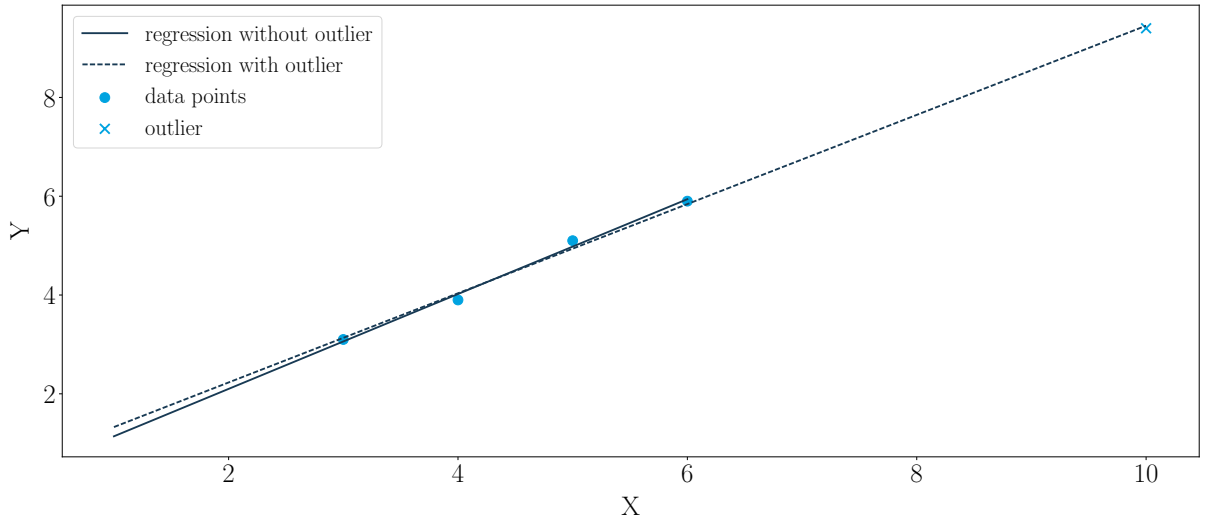

Figure 6.6: Outlier with strong leverage and little influence.

Figure 6.7 illustrates an outlier with an unusual X- and Y-value. The example shows that when this outlier is deleted, both the slope and intercept of the regression line will change dramatically.

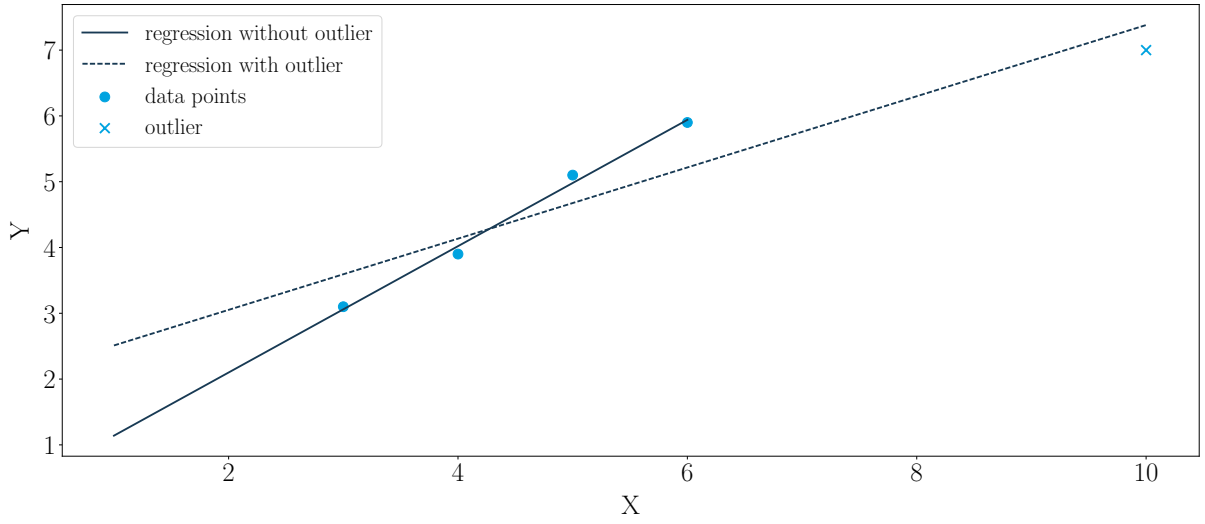

Figure 6.7: Outlier with strong influence and leverage.

6.2.2 Applying Cook's Distance

The Python library named *statmodels.api* provides the functionality to apply Cook's distance to large data sets. Referring to the example from Figure 6.1 and its dataset, expressions (6.4) and (6.5) are used to create a new dataset that consists of the maximum daily energy. Another dataset is created consisting of the daily peak power levels. Each of these datasets are stripped of their zero values since these values have a great influence on the regression and are not required. The first step of the statistical tool is to fit an ordinary least squares (OLS) regression model to the data as illustrated by Figure 6.8.

From this scatter plot, it can be examined that some data points are separate from the rest, which indicates that these points will most likely be influential data.

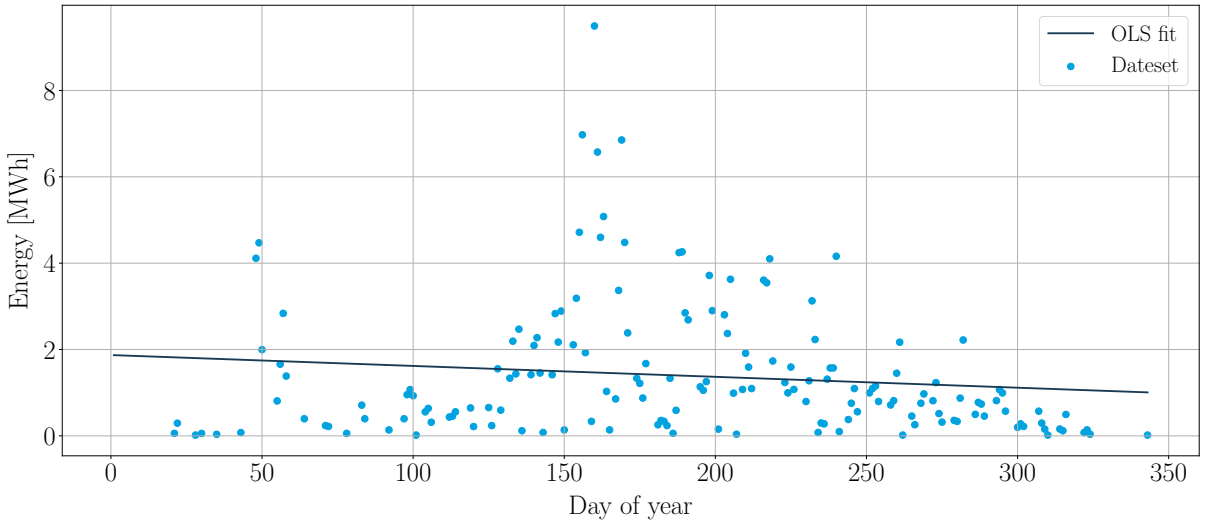

Figure 6.8: Regression of daily energy dataset.

Next, the influence of each data point is calculated using Cook's distance. This is illustrated by a stem diagram in Figure 6.9. Based on the rule of thumb, a Cook's distance value of between 0.5 and 1 is considered influential and more than 1 is considered very influential [108, 111]. Like all rules of thumb, it should be applied judiciously. The best practice is to inspect the diagram and examine what the influences of the values are with respect to one another. Circled in red are four influential data points that are identified by difference in magnitude compared to the rest of the data points.

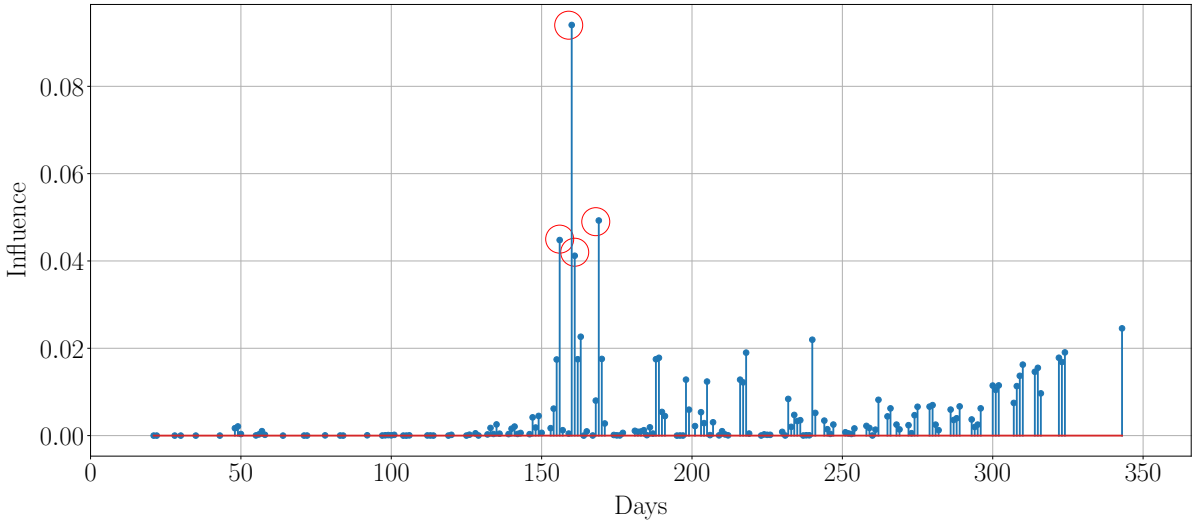

Figure 6.9: Cook's Distance for maximum energy dataset.

After identifying the influential data points, they are removed from the dataset and a new regression model is fitted to illustrate the effect of the removed data as seen in Figure 6.10. From this figure it is clear that the removed data points do not have a great influence on the fitted regression model. This is expected since the influence values are not close to 0.5. The values that are removed are circled in red.

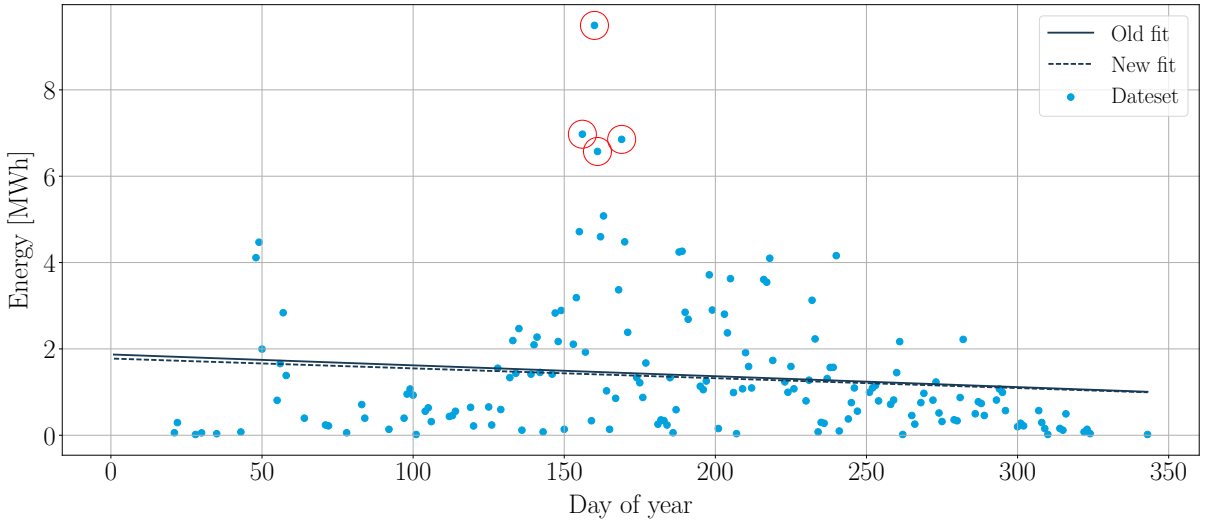

Figure 6.10: Regression of new daily energy dataset.

The process of sizing the battery is repeated with the new dataset and the results are summarised in Figure 6.11. The removal of the anomalous data points reduced the required BESS energy by 46.5% and the required maximum power by 9.5%. The reduction in power is due to excluding the same days that the maximum energy is excluded. However, it is important to remember that power and energy are not dependent on each other; the maximum peak power does not necessarily occur when maximum energy occurs, thus these two components should be looked at separately. Excluding anomalous feeder peaks can reduce the BESS requirement substantially. Based on how critical the situation at the feeder is, the assessor can determine whether or not to proceed with the optimised sizing strategy. Businesses, on the other hand, might be in a better position to consider this strategy for peak power reduction.

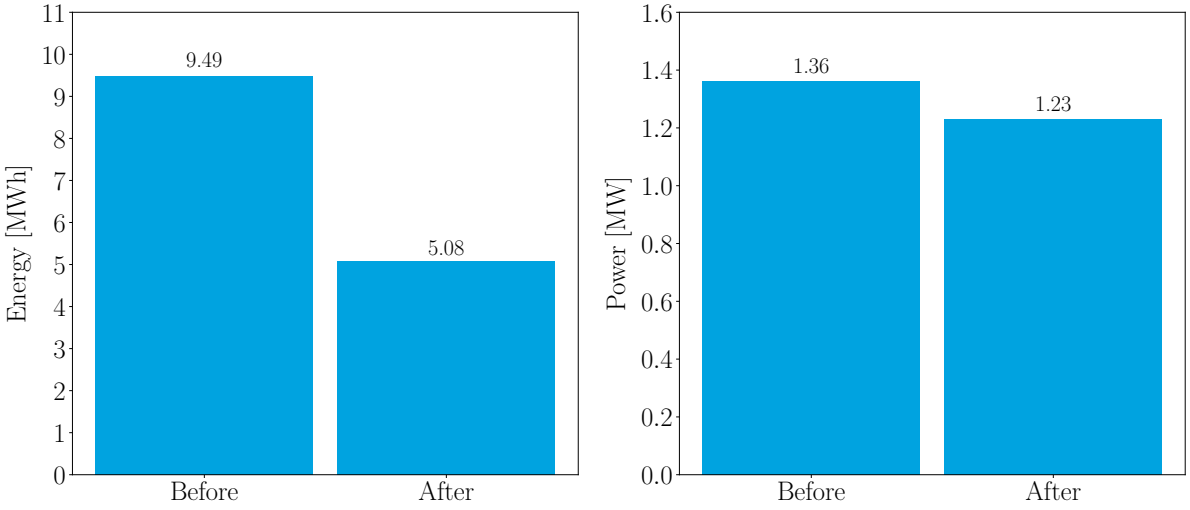

Figure 6.11: Comparison between BESS power and energy specifications before and after applying Cook's Distance.

The daily peak power data is also relevant using the sizing strategy but in this case it did not have any outliers with significant influence, as seen in Figure 6.12. The last value has the most influence but it is a value which lowers the mean. It is better in this case to optimise the maximum required energy. This is because the peak power data has no real outliers which could reduce the required power when excluded.

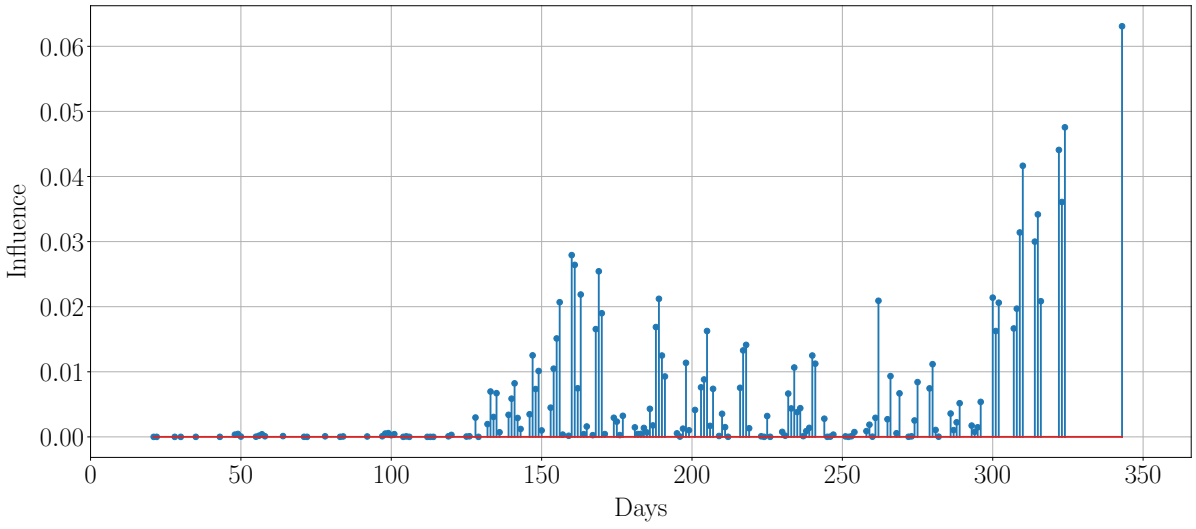

Figure 6.12: Cook's Distance for peak power dataset.

6.2.3 Impact of PV on the Load Distribution Curve

With the push for higher adoption of renewables, photovoltaics is one of the most popular technologies to be considered by utilities to provide more energy. This high adoption rate in the utility sector is reducing the capital cost of these systems, making it more affordable for businesses and residential customers. At the moment, there are only a

handful of customers who have roof-mounted PV installations but municipalities could provide these at subsidised cost in an attempt to reduce peak loads on feeders.

Considering PV installations for a business or an area serviced by a specific overloaded feeder not only reduces the peak load but also reduces the required BESS specifications. To illustrate this: a 0.5 MW, 1 MW and 2 MW PV installation is applied to the example data and shown in Figure 6.13. From this load distribution curve, it can be seen that the PV installation capacity assists with the peak load shaving but not where the highest peaks occur. This is due to these peaks being typically after sunset. However, during the day when the power levels are below the peak level, the PV capacity scales well.

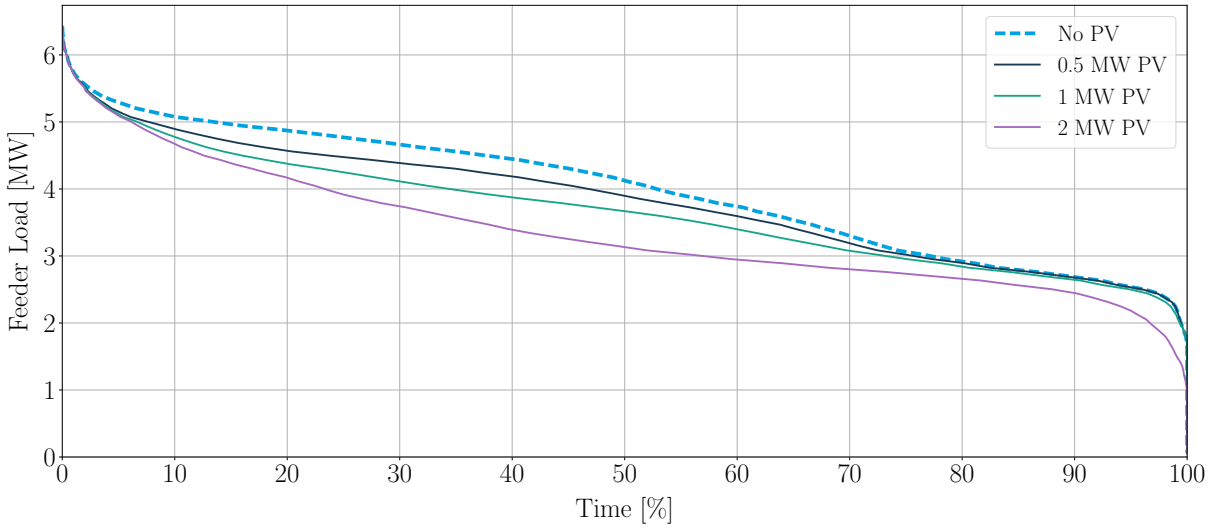

Figure 6.13: Load distribution for various PV installation capacities on a feeder.

Another consideration is the direction in which the PV panels face. It can allow the peak power of the PV system to be shifted in an attempt to improve peak load shaving. Figure 6.14 illustrates how changing the facing of the 1 MW PV installation affects the load distribution. It can be seen that the west-facing installation provides slightly better peak load shaving because it is facing the sun during sunset, which provides higher power closer to the time of the peak loads.

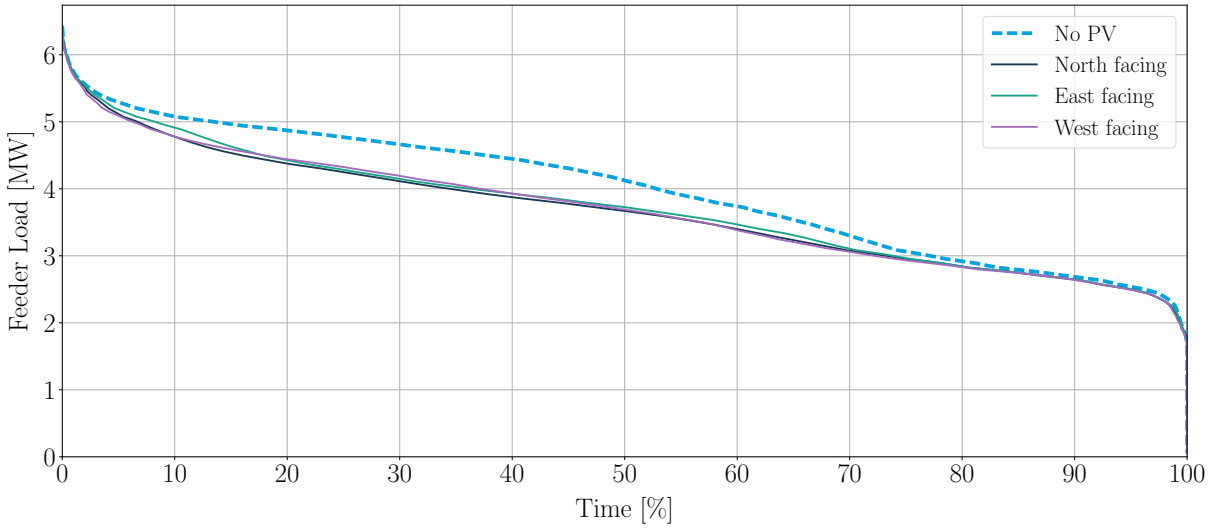

Figure 6.14: Load distribution for different facing PV installations on a feeder.

6.2.4 Test Cases

Using data provided by the NSP, BESS sizing is done for five different peaking distribution feeders, which can be seen in Figure 6.15. The data consists of hourly power readings for an entire year. A PCU efficiency of 90% is chosen and a minimum SOC of 20% is applied. Peak power targets are set for each case and the results of each sizing strategy are compared. The results can be examined in Table 6.1. The table describes the specifications of the feeder which include its current peak power and the desired target power. This is followed by the BESS requirements, based on the unoptimised sizing strategy, and the optimised BESS requirements.

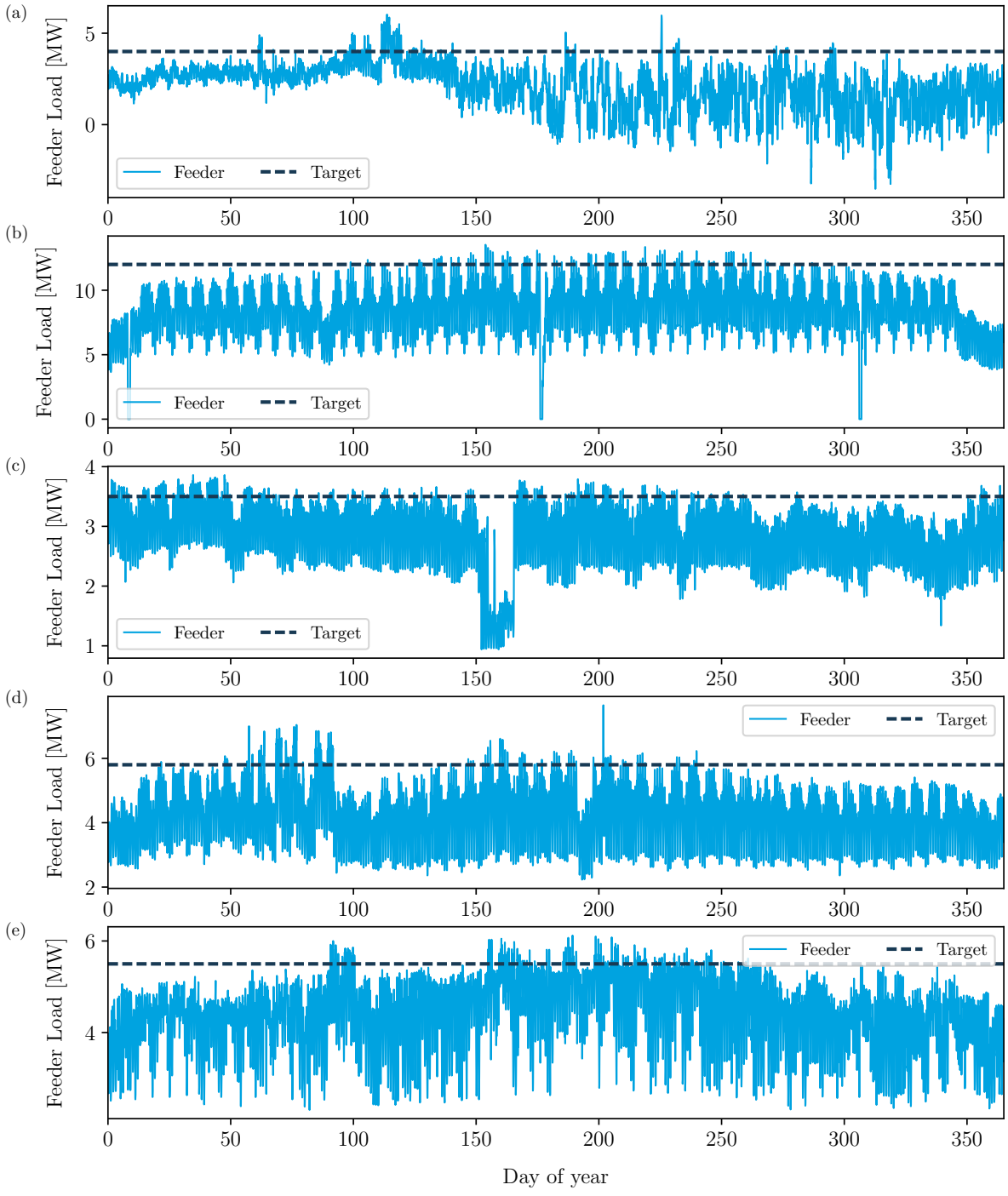

Figure 6.15: Peaking distribution feeders. (a) Case 1. (b) Case 2. (c) Case 3. (d) Case 4. (e) Case 5.

Table 6.1: BESS sizing for 5 test cases.

Cases		1	2	3	4	5
Feeder description						
Peak	[MW]	6.025	13.53	3.86	7.65	6.12
Target	[MW]	4	12	3.5	5.8	5.5
BESS requirements						
Power	[MW]	2.25	1.7	0.4	2.06	0.69
Energy	[MWh]	31.13	4.24	4.19	13.21	5.31
Optimised requirements						
Power	[MW]	2.25	1.7	0.4	1.38	0.69
Energy	[MWh]	24.95	3.58	4.19	13.21	3.49
Coverage	[%]	95.7	96.2	100	98.6	97.6

Cases 1, 2 and 5 have optimised energy requirements and case 4 has an optimised power requirement. Case 3; however, presents no outliers for which it can be optimised; thus the results remain unoptimised. The coverage indicates what percentage of the required days the optimised BESS can cover in full. From these test cases, one can see that either power or energy can be optimised substantially. However, this optimisation is only possible if the feeder can be allowed to exceed the target restriction on the odd occasion.

6.3 Peak Load Shaving Tool

The peak load shaving tool is set up to be a simple and easy to use Python script that enables users to receive a good estimation of the energy storage system size required. The tool implements Venu *et al.* [14]'s worst case scenario sizing strategy as well as the optimised sizing strategy. The results of both strategies are presented for comparison. The tool's sequence is illustrated in Figure 6.16.

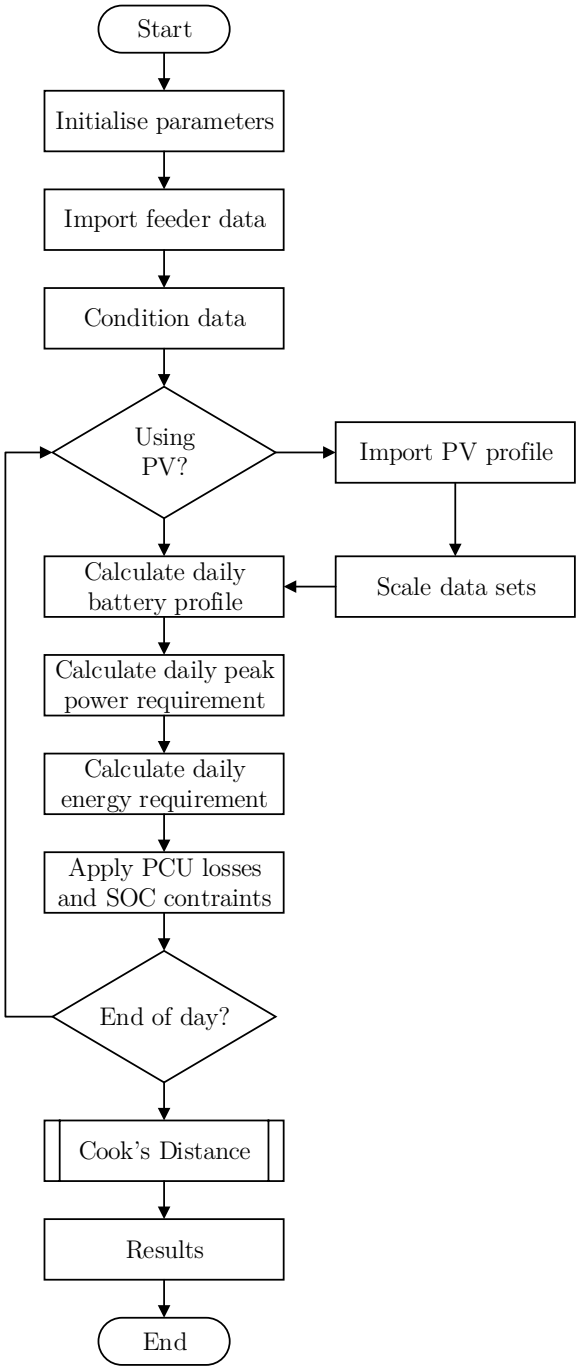

Figure 6.16: PLS tool flow diagram.

The tool starts by initialising the required parameters and applying the user-defined parameters. These parameters are summarised in Table 6.2 and determine what results will be presented to the user.

Table 6.2: Peak load shaving tool parameters.

Parameter	Unit	Description
TS_{feed}	hr, min, s	Time-step for feeder data
TS_{PV}	hr, min, s	Time-step for PV data
L_{data}	Days	Length of input data
PV_{status}	Boolean	Choose to include PV profile
CD_P	Boolean	Determine Cook's Distance for power
CD_E	Boolean	Determine Cook's Distance for energy
P_{target}	MW, kW	Feeder power target
η_{PCU}	%	Power conversion unit efficiency
SOC_{min}	%	Battery minimum SOC constraint
SOC_{max}	%	Battery maximum SOC constraint

Once the parameters are set, the tool imports the feeder data. The data must be in a simple, two column, comma delimited, format. Table 6.3 provides an illustration of what the dataset should typically look like. This format is also relevant to the PV input profile. Input data such as these profiles are typically provided in a yearly, monthly or weekly format; thus the model groups the data into separate days for the purpose of determining the daily BESS requirements.

Table 6.3: Feeder and PV import data format.

Time [hr, min ,s]	Power [MW, kW]
1	2.2
2	2.4
3	1.8
...	...

If the user decides to use a PV installation, the datasets from the feeder and PV profiles are scaled such that their time-steps match. Next, the daily energy-throughput profile for the battery is determined using expression (6.4). The tool temporarily stores the profile so that the user can choose to export it for further analyses. The maximum battery energy requirement is determined using expression (6.5). During the process of calculating the maximum energy, the tool stores the battery profile which the user can choose to export for further analysis. The peak power is calculated by iterating through the battery energy-throughput profile and selecting the maximum power value. Next expressions (6.3) and (6.6) are used to determine the BESS requirements. Depending on which part, power or energy, the user wants to optimise for, Cook's Distance is determined for that dataset.

The results are expressed by the screen capture in Figure 6.17. It can be seen that the first set of results are provided by the original sizing strategy before the data is conditioned using Cook's Distance. These are the specifications that the BESS requires

in order to provide support for the feeder for all of the relevant days. The second set of results are provided by the optimised sizing strategy which uses Cook's Distance to identify anomalous power and energy usage. The outliers are removed and the new BESS specifications are determined. The battery usage results indicate how many days the BESS will be required during the course of the year and it also indicates that if the sizing is optimised in terms of energy or power, how many days the BESS will be used. This gives the user an indication of how many days are not completely serviceable using the optimised specification.

```
PRE-DATA CONDITIONING:
=======================================================
Max battery energy:                 9.49 MWh on day 160
Max battery power:                  1.36 MW on day 160
Total Energy:                       231.11 MWh

POST-DATA CONDITIONING:
=======================================================
Max battery energy:                 5.08 MWh on day 163
Max battery power:                  1.36 MW on day 160
Total Energy:                       201.22 MWh

BATTER USE:
=======================================================
Before optimisation:                166 days
Optimised for power:                166 days
Optimised for energy:               162 days
```

Figure 6.17: Screen capture of tool results.

6.4 Conclusion

In this chapter Venu *et al.* [14]'s the battery sizing strategy for peak load shaving is optimised. The original strategy is based on the worst case scenario where the BESS is sized such that it can provide the maximum required energy and power for any given day which previously exceeded the feeder specifications. This is sufficient to determine the required BESS specifications. However, it is seen that feeder profiles consist of days with outlying power and energy usage that can cause unnecessary over-sizing of the BESS.

A statistical tool called Cook's Distance is used to identify influential data points. The tool does this by identifying outliers through discrepancy and leverage. Using Cook's Distance, the anomalous data points are removed and the original sizing strategy is repeated providing optimised specifications for the BESS. The BESS is able to provide support to the feeder during all of the days with common peaking power levels but not during outlying days. The optimised strategy is applied to five feeder profiles to test it. Four of the five cases provided substantial battery reductions with regards to energy and power. One case did not provide any improvement since no outlying data was found.

The effect of PV installations at the feeders was also investigated. It was found that PV installations lack the required power support during peak power usage which usually occurs during sunset. Changing the facing of the PV installation to a west-facing orientation can provide slightly more power during the peak power usage but not enough to justify the extra cost. However, PV could be used to charge the BESS during the daytime.

The original and optimised sizing strategies are implemented in Python as part of a tool that users can use to conveniently determine the required BESS size. The tool also allows the user to add a PV output profile to assess how its support can influence the sizing of the BESS. The input parameters and sequence of the tool are explained as well as the format of the data which it imports. The tool aims to automate the process of identifying anomalous power usage data and exclude these data points for the purpose of sizing the BESS.

The optimised sizing strategy is good to consider when there are regular cases where the feeder is operating near or above its rated conditions and one is not concerned about the outlying cases. If the feeder is never allowed to operate near or above its rated specifications, the original sizing strategy would be a better option since it would cover the extreme cases as well. The optimised strategy aims to size the BESS in a more cost-effective way.

Chapter 7

Cost Analysis

The utilities and the network service providers (NSP) experience various problems on the network and, in recent years, with renewable energy generator installations as well. Only a few problems are discussed in this thesis. However, the involved parties are aware of some of the solutions that are available but the costs of these solutions are a big concern. The purpose of this chapter is to put the levelised cost of energy (LCOE) of the solutions into perspective and show how variations in these solutions can affect the cost.

Firstly, one has to investigate the costs of large scale battery energy storage systems (BESS) and utility scale PV installations. These systems can be divided into two cost sections: the installed systems costs and the operation and maintenance costs. The financing costs, tax credits and incentives are left out of the calculations because they apply to both the PV installation and the battery system at presumably equal rates and they take away from the actual impact which the respective systems have on the cost. It is not just current costs that are of interest but also the predicted future costs of these respective systems. The idea is to provide utilities and the NSP with information with which they can determine when, if not right now, BESS can be a viable solution to these problems.

Since BESS sizing is done during all three solutions discussed in Chapters 3, 4 and 5, how changes in these solutions affect the BESS specifications and the costs is investigated. The predicted costs are also investigated. The purpose during this chapter is not to provide detailed costs on these systems but merely to look at how the BESS cost compares with the PV installation cost and how changes in the solutions can affect the overall LCOE.

7.1 System Costs Calculations

The costs of the systems are calculated using the LCOE. The LCOE for a power plant can be defined as the ratio of the lifetime cost of the installation to the lifetime energy production [112] and can be expressed as follows:

$$LCOE = \frac{\text{Total life cycle cost}}{\text{Total liftime energy production}} \tag{7.1}$$

The LCOE is chosen because it is one of the most commonly used metrics and because it translates the costs of all the components to the cost of producing energy per kWh. With this method, other energy production systems can be compared to each other by

the same metric and the LCOE also gives a broader picture of the costs involved because it incorporates more than just the hardware-related costs.

In this section, the LCOE calculations, for each of the systems used throughout the thesis, are discussed. It is also explained how the results of each chapter are presented.

7.1.1 LCOE for Centralised PV and Separate Centralised BESS

The configuration of centralised PV and a separate centralised BESS is used to describe the system configuration that is used in Chapter 5 for weak network strengthening. It is a system where the complete PV array is installed at a centralised location and the complete BESS is installed at a separate location, thus the BESS cannot share any equipment such as inverters with the PV power plant. In this section, the levelised cost calculations for this configuration are discussed.

7.1.1.1 Total PV Yield

The total PV yield refers to the total amount of energy produced by a PV power plant in its expected lifetime. One cannot know exactly how much this will be, however it can be estimated based on the system size and the climate of the location. Another factor to take into account is the degradation of PV panels during the course of the installation's lifetime. The energy yield per year can be calculated using the following expression:

$$E_i = E_{per.MW} \times P_{PV}(1 - \eta_{loss}(i-1)) \tag{7.2}$$

where E_i is the total yield for year i. $E_{per.MW}$ refers to the yield, in MWh/MWp, that can be expected per year from a megawatt size installation at a certain location and P_{PV} is the peak power specification of the PV installation in MW. For the purpose of this thesis, a location called De Aar, in the Northern Cape, is considered, thus the energy yield of a 75 MWp solar PV power plant is used to determine the yield per installed MW for the area. η_{loss} is the percentage degradation per year of the PV panel and is usually specified on the data sheet. Having added up the yearly yield for the PV installation, the total yield (E_{total}) can be expressed as follows:

$$E_{total} = \sum_{n=1}^{n} E_i = E_1 + E_2 + ... + E_n \tag{7.3}$$

7.1.1.2 LCOE for the PV Installation

The LCOE for a PV installation is calculated based on equation (7.1) and is expressed as follows [112]:

$$LCOE_{PV} = \frac{C_{inst} + \sum_{n=1}^{i} C_{O\&M.i}}{E_{total}}, \tag{7.4}$$

where C_{inst} is the installed cost of the PV power plant, $C_{O\&M.i}$ is the operation and maintenance cost of the PV power plant for i amount of years and E_{total} is the total energy yielded for the lifetime of the power plant.

7.1.1.3 LCOE for the BESS

The levelised cost of the energy for the BESS ($LCOE_{BESS}$) is calculated for the PV yield to express the cost of the BESS as part of the cost of production of energy. This is done because the BESS now serves as a requirement for the installation of a larger PV plant to be connected to the electric network. Because the BESS is separate from the PV installation, it cannot use the inverters and other hardware from the PV system. The levelised cost of the the BESS is calculated in the same way as the levelised cost of PV:

$$LCOE_{BESS} = \frac{C_{inst} + \sum_{n=1}^{i} C_{O\&M.i}}{E_{total}}, \tag{7.5}$$

where C_{inst} is the installed cost of the PV power plant, $C_{O\&M.i}$ is the operation and maintenance cost of the BESS for i amount of years and E_{total} is the total energy yield for the lifetime of the power plant. The installed cost of the BESS consists of various components and for the purpose of the thesis these are: the battery costs ($C_{batteries}$) and the balance of system costs (C_{BOS}). These can be expressed by the following equation:

$$C_{inst} = C_{batteries} + C_{BOS}. \tag{7.6}$$

7.1.1.4 Cost Presentation

The LCOE contribution from BESS is presented as a percentage of the LCOE of the PV installation as follows:

$$\%LCOE_{BESS} = \frac{LCOE_{BESS}}{LCOE_{PV}} \times 100. \tag{7.7}$$

This is done to give utilities a perspective of what the extra costs would entail compared to the current budgeted cost of the PV installation.

7.1.2 LCOE for Centralised PV and BESS

The centralised PV and BESS represents the system configuration of Chapter 4 on fluctuation mitigation. It is a system where the complete PV array and BESS are installed at the same centralised location which means the BESS is installed behind the inverters of the PV array. A report by L. Ortiz [113] shows the breakdown of the BOS costs of BESSs to consist of inverter costs, containerisation costs and controller costs. Since the BESS and the PV array utilise the same inverters, the cost of the inverters are neglected from the BOS costs for the BESS. The levelised cost of energy for PV is calculated using equation (7.4) and the levelised cost of energy for the BESS is calculated similarly in equation (7.5) with the only difference being that the inverter costs are neglected. The results of this system are presented in the same way as described in the previous section.

7.1.3 Levelised Cost of Energy for Peak Load Shaving

In Chapter 6, how a BESS sizing strategy for peak load shaving can be optimised is investigated. The BESS for peak load shaving does not generate energy but is used to store energy for later use. The amount of energy that is discharged from the BESS

for peak load shaving serves as the total lifetime energy for the LCOE calculation, thus the equation (7.5) is used. In the equation, E_{total} is replaced by the discharged energy ($E_{discharged}$) over the life time of the BESS installation as follows:

$$LCOE_{BESS} = \frac{C_{inst} + \sum_{n=1}^{i} C_{O\&M.i}}{E_{discharged}} \tag{7.8}$$

7.1.4 Cost Representation

In the chapter on BESS sizing for peak load shaving, two sizing strategies: the original, worst case scenario strategy and the optimised strategy are discussed. To illustrate the improvements achieved by the optimised strategy; the LCOE saving is presented as a percentage of the LCOE of the original sizing strategy. The improvement can be expressed by the following equation:

$$\%\text{Improvment} = \frac{LCOE_{ori} - LCOE_{opt}}{LCOE_{ori}} \times 100, \tag{7.9}$$

where $LCOE_{ori}$ is the levelised cost of energy of the original sizing strategy and $LCOE_{opt}$ is the levelised cost of energy of the optimised sizing strategy.

7.2 System Cost Data

7.2.1 PV System Costs

A study by the International Renewable Energy Agency [114] includes the historical prices of utility scale PV installations from 2009. It also includes predicted prices up until 2025. These prices are globally weighted averages and represent the installed PV costs used in this study. The prices are illustrated in Figure 7.1. The operating and maintenance cost for a PV power plant is reported to be 16 USD/kW-yr by NREL [115].

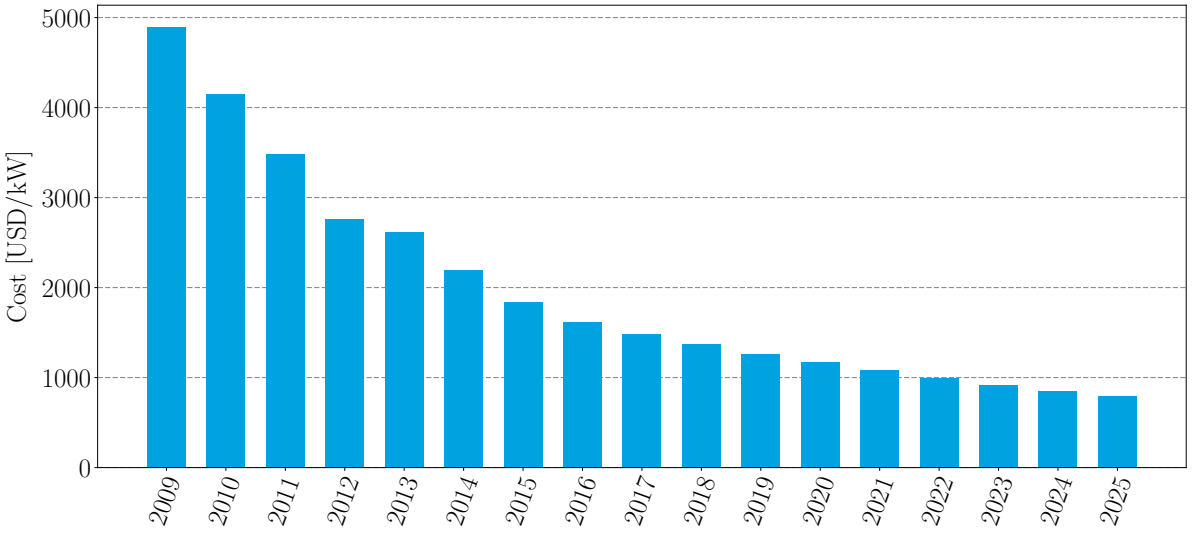

Figure 7.1: Utility scale PV installation cost per KW.

7.2.2 BESS Costs

The BESS system costs consist of three parts: the battery costs, the BOS costs and the operation and maintenance cost. The cost of the battery packs is obtained from a report published by McKinsey & Company [102]. The report shows the historical cost of battery packs from 2010 to 2015 and it also estimates a costs of $100 per kWh between 2025 and 2030. Tesla already claimed a $190/kWh price in 2016 and hinted that the cost will be at $100/kWh by 2020 [7, 116]. Tesla plans to achieve this target with the Gigafactory programme. General Motors (GM) however reported a $145/kWh cell cost and expects their battery cells to reach $100/kWh (+ 20%) for battery pack price according to David Snydacker (a battery expert at Dosima Research) by 2022 [7].

All the battery prices are represented in Figure 7.2. The historical data can be followed up to 2016 and the prices which follow are estimated by a second order polynomial trend line to provide values for the missing years. These prices represent the battery costs.

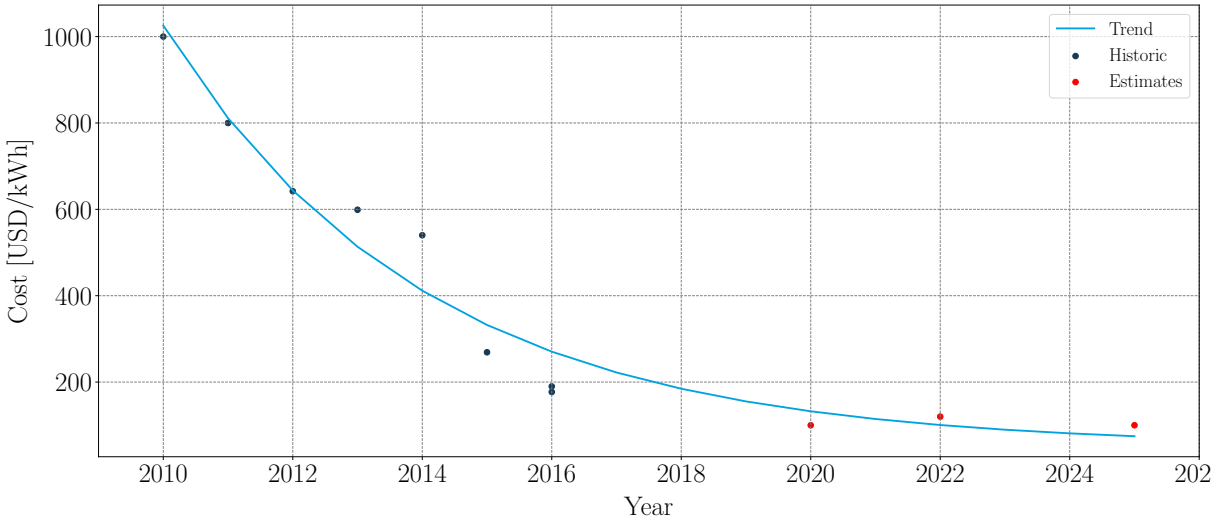

Figure 7.2: Utility scale lithium storage costs.

A report by L. Ortiz [113] estimates the energy storage BOS prices to drop to below $400/kW by the year 2020. Figure 7.3 illustrates the complete price estimation. Zakeri *et al.* [117] reported operation and maintenance cost in the range of 8.22 USD/kW-yr for lithium batteries.

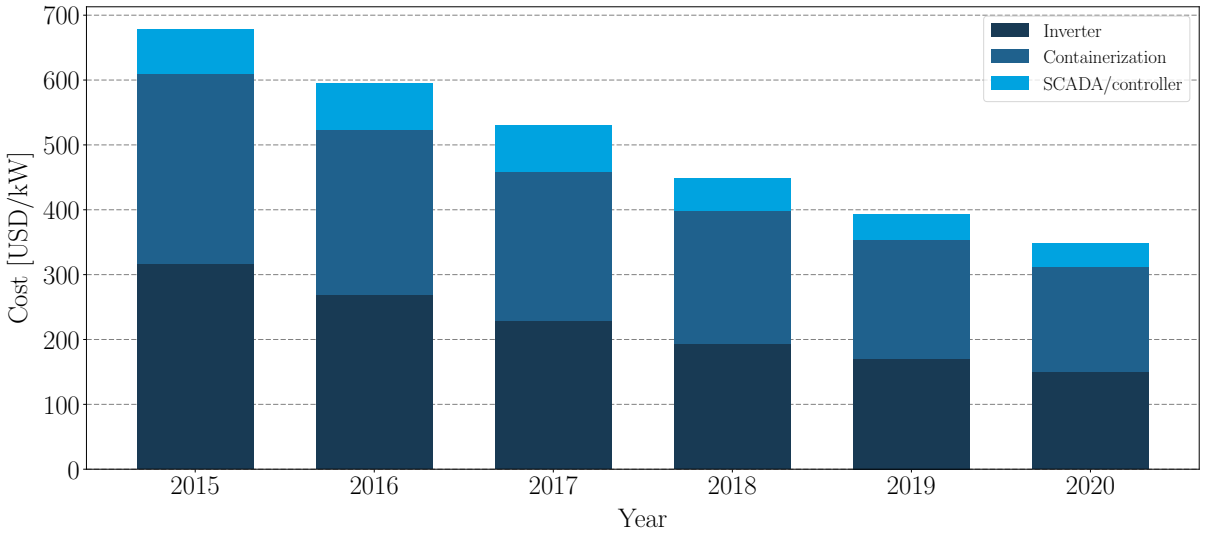

Figure 7.3: Utility scale energy storage BOS costs.

For the purpose of this thesis, the price estimates up to 2024 are required. It is assumed that the BOS cost will keep on following the trend predicted in the report by L. Ortiz [113]. Using this assumption, a second order polynomial fit is done to the data to estimate future costs. However, it is important to note that these BOS costs can be less than the trend is estimating if the prices reach their minimums sooner. Figure 7.4 illustrates the fit and the predicted costs.

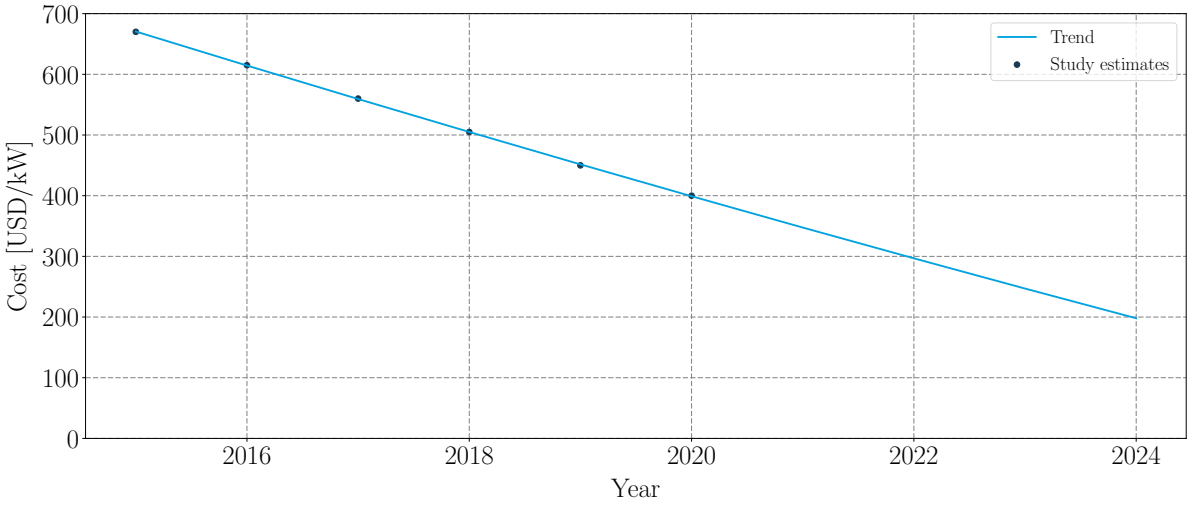

Figure 7.4: Utility scale energy storage BOS costs.

7.3 Cost Assessment

In this study, grid assistance using batteries is investigated and specifically three different problems are looked at, namely fluctuation mitigation, network strengthening, and peak

load shaving. A LCOE assessment is done for each one of the solutions for the respective problem cases.

7.3.1 Fluctuation Mitigation for intermittent PV

In Chapter 4 the intermittent nature of PV installations as well as fluctuation mitigation methods are investigated. An inverter ramp-rate control strategy is implemented to mitigate the fluctuations. The strategy is applied using different degrees of damping and it was found that higher degrees of damping require larger capacity batteries. A cost breakdown is done to show that the degree of damping affects the contribution of BESS to the total LCOE. This is done for the years 2017, 2020 and 2024 to examine how the predicted costs will influence the cost breakdown of the respective parts in the installation. The BESS is assumed to be a lithium chemistry with a calendar life of 7 years; thus, the batteries will be replaced twice after the initial installation. The efficiency of the power conversion unit is assumed to be 90% and the batteries are allowed a maximum depth-of-discharge of 90%.

The LCOE for the BESS is represented as a percentage of the LCOE of the PV installation; thus it can be seen in Figure 7.5, 7.6 and 7.7 that the LCOE of the BESS reduces as larger adjustment ramp-rates are allowed. This is expected since the size of the BESS reduces. Choosing the 12% adjustment ramp-rate above the 1% can reduce the battery capacity enormously, as illustrated in Chapter 4, reducing the LCOE increase between 1.48% and 2.63%.

Examining all three of the figures, it is noticed that the BESS, in 2016, is responsible for increasing the energy production costs by 18.59% for 1%/min ramp-rate, which is a substantial amount. If the projected costs are correct, the LCOE increase can reduce between 1.83% and 2.98% by 2024, which suggests that BESSs are becoming more affordable.

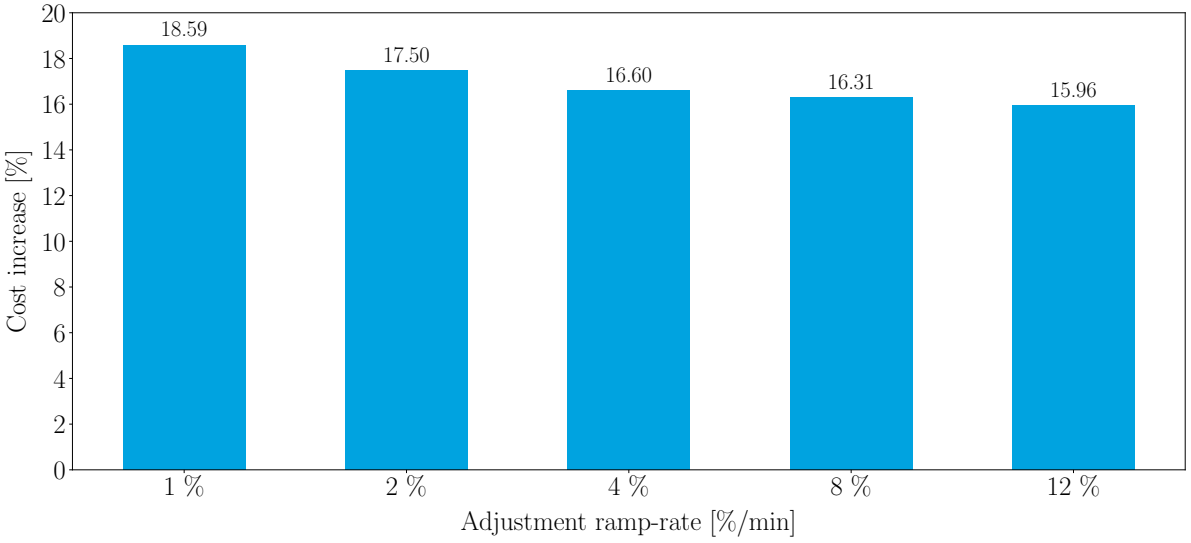

Figure 7.5: 2017 levelised cost of energy increase due to a BESS used to dampen fluctuations at certain ramp-rates.

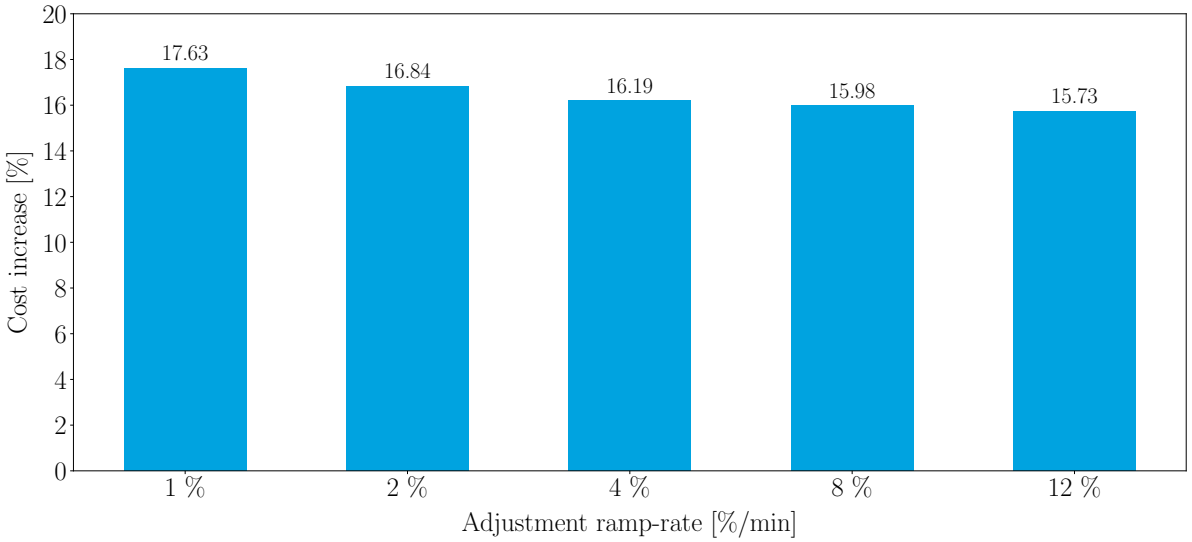

Figure 7.6: 2020 levelised cost of energy increase due to BESS used to dampen fluctuations at certain ramp-rates.

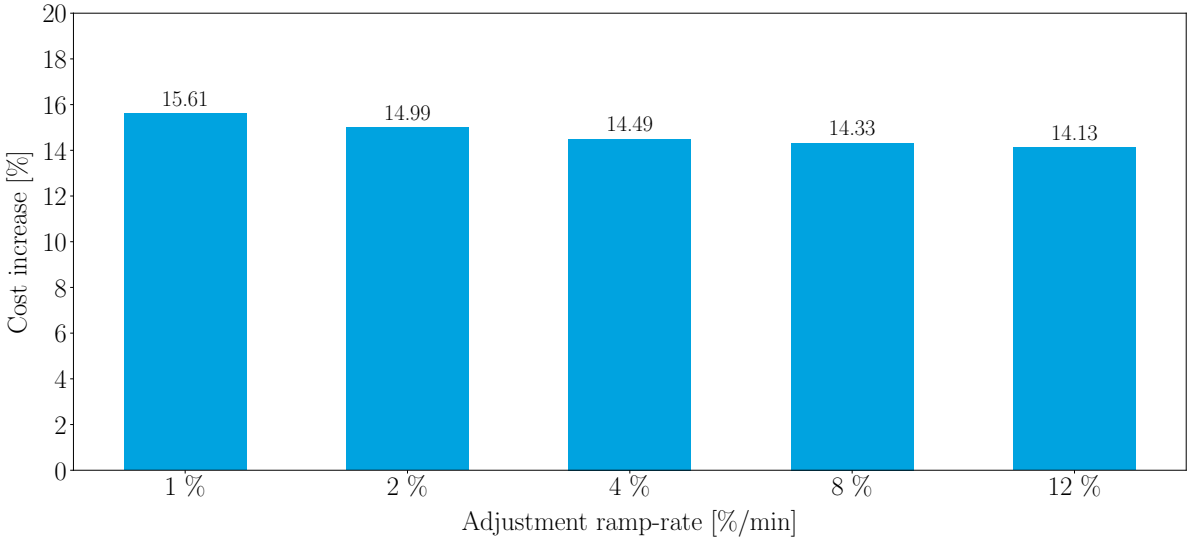

Figure 7.7: 2024 levelised cost of energy increase due to BESS used to dampen fluctuations at certain ramp-rates.

The results are presented in this manner to illustrate to utilities the costs involved when considering these solutions. Presenting the results as a percentage of the LCOE of the PV installation give utilities a benchmark with which to reference the extra costs of the BESS. This representation is relevant assuming that the prices of the various systems scale equally with size and region. It is also important to note that for fluctuation mitigation, the size of the BESS can change a lot based on the regional climate and weather.

7.3.2 Network Strengthening For Increased PV Installation

In Chapter 5 there is a description of how a BESS is used in conjunction with an on-load tap changing transformer to ensure grid compliance at the point of common coupling. The BESS is sized to provide enough active power during a sudden power-loss condition whilst not discharging past a minimum SOC of 20%. The BESS peak power requirement is 22.2 MW with an energy capacity of 385 kWh. With a PV power plant design life of 20 years and a calender life on the lithium chemistry of 7 years, it is expected that the batteries will be replaced twice after the initial installation.

The BESS cannot be installed behind the inverter of the PV power plant because if a fault occurs at the power plant that causes it to disconnect, the BESS will not be able provide active power support. Thus, a complete BESS needs to be installed separate from the PV power plant; hence the centralised PV and separate centralised BESS.

Using the data in Section 7.2 and expressions (7.4),(7.5) and (7.7), the BESS is represented as a percentage of the LCOE of the PV installation as illustrated in Figure 7.8 and 7.9. Knowing that the PV and battery system costs are going to decline, it is observed that the cost of the BESS will reduce further compared to the PV since its added contribution reduces over time. This could potentially make it more financially feasible to consider in the future. Given the current situation, utilities can get a 50% increase in installed capacity while producing energy that costs 12.1% more in 2016 but this increase in capacity will only cost 9.24% more in 2024.

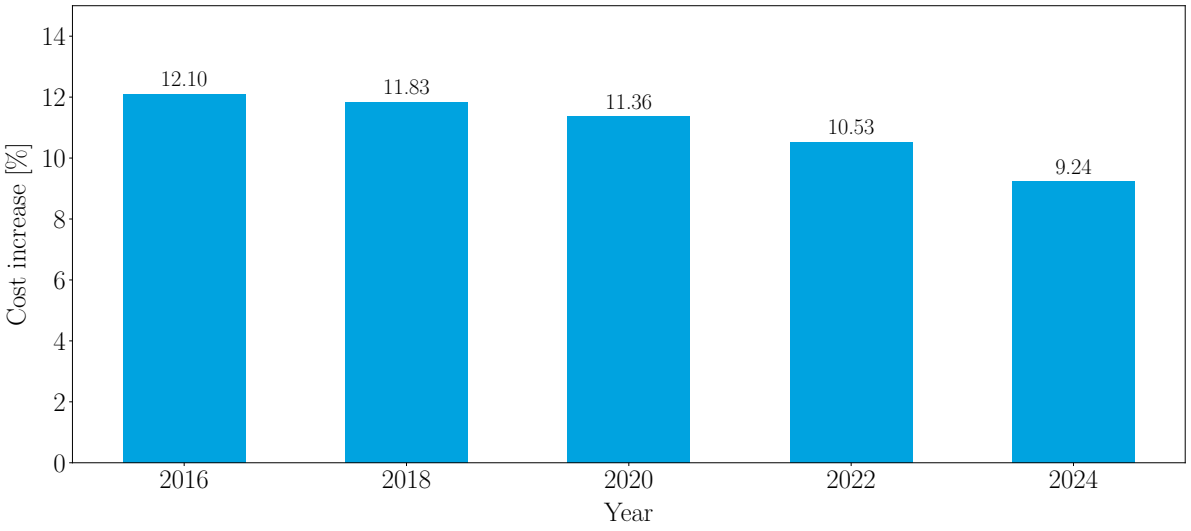

Figure 7.8: Levelised cost of energy increase due to a BESS used to strengthen the network for a 75 MW PV installation.

Considering the same weak network, if the planned PV system is reduced to a 60 MW installation, the BESS requirements can be reduced to 11.1 MW peak power and 173 kWh of energy. When examining Figure 7.9, it can be seen that the cost of the BESS compared to the PV system size is smaller in the 60 MW case than the 75 MW case. This is to be expected because the 50 MW PV installation does not require a BESS; thus as the PV installation capacity increases the BESS requirements increase. Given this situation,

utilities can get a 20% increase in installed capacity while producing energy that costs 7.55% more in 2016 but this increase in capacity will only cost 5.77% more in 2024.

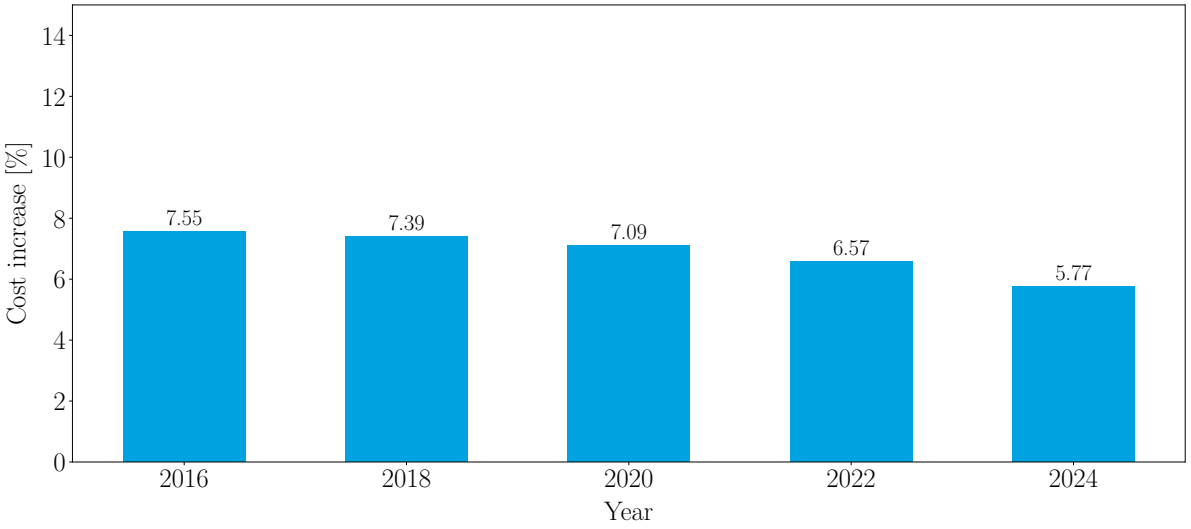

Figure 7.9: Levelised cost of energy increase due to a BESS used to strengthen the network for a 60 MW PV installation.

It is up to the utilities to decide whether it is feasible to consider a BESS to increase the size of the PV installation now or whether they should wait.

7.3.3 BESS Sizing for Peak Load Shaving

In Chapter 6 a BESS is sized for peak load shaving. During a peak load shaving event, the BESS provides the required energy in order to prevent feeders from operating above the rated maximum specifications. A new sizing strategy is developed using a statistical tool called Cook's Distance to identify influential outliers. These outliers are anomalous power usage cases and typically have abnormally large magnitudes that have a substantial influence on the sizing of the BESS.

The resulting BESS specifications in Table 6.1, in Chapter 6, are used. The LCOE of each case, for the original and optimised sizing strategy, is determined using equation (7.8). These costs are compared and the savings are calculated using equation (7.9) and illustrated in Figure 7.10. A substantial cost saving is seen in four of the five cases. A cost savings of up to 24% is seen in Case 5. Case 3 is a situation in which no anomalous power usage is detected; thus, no improvement can be made as a results of the sizing of the BESS.

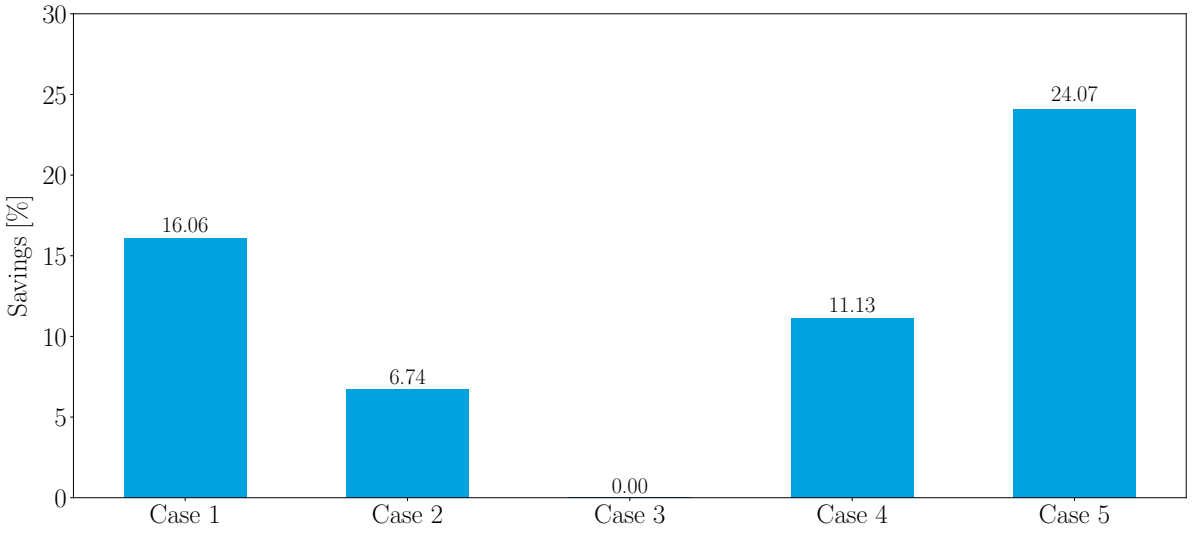

Figure 7.10: Cost saving of optimised BESS sizing strategy for peak load shaving.

7.4 Conclusion

In this chapter, a cost analysis is done on the implementation of a BESS for fluctuation mitigation, grid strengthening and peak load shaving. These strategies are discussed in Chapters 3, 4 and 5, respectively.

The fluctuation mitigation model allows the user to adjust the degree of damping which leads to changes in the BESS requirements. How the degrees of damping affect the cost breakdown of the complete system is investigated. It is found that a BESS, utilised for the purpose of fluctuation mitigation, contributes to more than 18% of the LCOE of the PV power plant in 2016. This is expected to decrease to 15.7% in 2024. Decreasing the degree of dampening can reduce the contribution of the BESS. However, the LCOE of the BESS is expected to keep on reducing until at least the year 2024.

The BESS can be utilised to assist PV installations on a weak grid in order to install larger capacity PV power plants. How the cost of the BESS influences the cost of energy production is investigated. It is found, for the specific weak network, that the BESS, in 2016, increased the costs by 12.1% in order to strengthen the grid for a 75 MW PV installation. A cost reductions in the BESSs can be expected at least until the year 2024 which can reduce to cost increase to 9.24%. It is also found that reducing the installed PV capacity reduces the percentage cost of the battery; thus, the BESS becomes a higher fraction of the LCOE as the PV capacity is increased in this case.

The cost savings with regards to the BESS sizing strategy for peak load shaving is investigated. It is found that the optimised sizing strategy can provide substantial cost saving if some compromises are made. As shown in Figure 7.10, there can be cases where there are no optimised solutions. Some cases can provide larger cost saving than others, this purely depends on the feeder profile. A cost saving of up to 24.07% is found for one of the case studies.

The three strategies can be adjusted to fit the specific scenario of the user and the cost analysis can be repeated so that the results are relevant to the specific case.

Chapter 8

Conclusion and Recommendations

In this thesis, three different problems with regard to the electric network are considered: the intermittent nature of photovoltaic (PV) technology, weak network strengthening for the integration of larger PV power plants and the optimisation of the sizing strategy of a battery energy storage system (BESS) for peak load shaving. Solutions to the problems, which are implemented in Python, serve as tools to provide a means with which users can assess these solutions and determine the costs involved.

8.1 Conclusions

8.1.1 Battery State-of-Health Model

In Chapter 2, a battery state-of-health (SOH) model is implemented in the form of a Python script. The model estimates battery degradation, at constant charge or discharge, as linear. Because the lithium chemistry ($LiFePO_4$) degrades in a linear manner; the model estimation is more accurate over time. Chemistries, such as lead-acid ($PbSO_4$), degrade exponentially; thus, the model's estimated degradation is less accurate over time. If users plan to track the SOH over time; it is recommended that a different model be used for non-linear degrading batteries. Otherwise, users are recommended to calibrate the model and use it to determine when the battery's end-of-life will occur. This tool eases the process of modelling and benchmarking various battery chemistries which can assist users in deciding whether or not a battery is sufficient for a task. If an accurate representation of the battery degradation is imperative, an equivalent circuit model or electrochemical model should be considered.

8.1.2 Photovoltaic Systems

In Chapter 3, the photovoltaic system implemented for fluctuation mitigation is discussed as well as the fundamentals around photovoltaics. How the photovoltaic output is influenced by temperature and irradiance is also discussed.

8.1.3 PV Fluctuation Mitigation

In Chapter 4 a PV output fluctuation mitigation model is selected and implemented, in Python, as a solution to the intermittent nature of PV technology. This model is based on an inverter ramp-rate control strategy which allows the user to apply a certain degree of damping to a PV inverter output profile. The user is left with a resulting inverter- and battery output profile which can be used for further analysis. This tool can be used in conjunction with the SOH model to provide results on the battery performance. Utilities can use such a tool to assess how this solution will affect the sizing and cost of the BESS. Furthermore, the tool can also be used to assess the smoothing of the power output on wind turbines.

Based on the assessment done on smoothing strategy, it is found that for higher degrees of damping larger capacity BESSs are required. For the specific test case, the peak power requirement remains largely unchanged until the degree of damping reaches the 12%/minute-mark. At this point, the peak power requirement reduces. Two battery chemistries are tested for the purpose of fluctuation mitigation. When compared to lead-acid ($PbSO_4$) batteries, lithium proves to be the superior battery for the demanding energy-throughput. It is also considered more cost effective for the task.

In Chapter 7, how the degree of damping influences the levelised cost of energy (LCOE) of the PV power plant is investigated. When restricting the fluctuating power output to 1%/minute, it is found that, for this test case, the BESS can increase the cost of energy production by more than 18%. Decreasing the degree of dampening to 12%/minute can reduce the cost increase between 1.48% and 2.63%. Based on the projected costs, the LCOE increase is to reduce between 1.83% and 2.98% by 2024. Utilities will have to consider how feasible this solution is for their case studies based on the required degree of damping. Utilities are recommended to repeat the cost assessment using their respective location weather data in the fluctuation mitigation model.

8.1.4 Network Strengthening for PV Integration

In Chapter 5 a BESS in conjunction with an on-load tap changing (OLTC) transformer is used to strengthen the electric network during sudden power loss conditions to allow for larger PV installations. This solution can prove useful to utilities looking for larger profits that result from larger PV installations but are restricted by the characteristics of the electric network. Utilities will have to determine how feasible the solution is based on the extra expenses and energy bids. Sizing the BESS according to this strategy can prove useful for the feasibility study. If required, utilities can also consider sizing the batteries such that they can be utilised for fluctuation mitigation or for other ancillary services.

In Chapter 7 how the BESS system affects the total LCOE of the PV power plant is investigated. As the planned PV installation capacity on a weak network increases, so does the cost of energy production due to the cost of the BESS. Thus the profit margin reduces as the PV installation capacity increases. In 2016, the BESS on a 75 MW PV

installation would have increased the cost of energy production by an estimated 12.1% whilst it is estimated to only increase the cost by 9.24% in 2024. In real terms, the utility could earn more but with a lower profit margin because there is 50% increase in installed capacity to 75 MW, over the originally allowed 50 MW, and it cost about 12% more to produce the same unit of energy. If the utility settles for a 60 MW installation, a 20% increase in capacity would be gained at the expense of producing energy that costs 9.24% more.

8.1.5 Sizing for Peak Load Shaving

In Chapter 6 a statistical tool known as Cook's distance is used to filter influential outliers from the feeder output datasets. This is done to provide an optimal BESS sizing strategy for peak load shaving that is aimed at cost reduction. Typically, the sizing strategies are aimed at the worst case scenarios. It is found that the worst cases are typically outliers and not regularly reoccurring cases. By removing these outlier, substantial reductions in power and energy requirements are seen. It was also found that some cases have no room for further optimisation.

In Chapter 7 how the reductions in the BESS specification influence the LCOE for the peak load shaving solution is investigated. The results are represented as a percentage of the costs saved. Cost reductions of up to 24.07% are examined between the tested cases. This BESS sizing strategy can prove quite useful to the network service provider as well as businesses trying to reduce their peak power requirement from the electric network.

8.1.6 Final Thoughts

In this thesis tools are provided and questions around three problems are answered. Solutions are provided to the respective problems as well as a means with which to assess the respective solutions. Each of the solutions are also assessed in terms of cost; providing information relevant to considering them.

The three solutions discussed in Chapters 4, 5 and 6 are significant because they can be used singly or be combined to form a multi-purpose solution. This includes a solution such as the integration of a PV installation into a weak network using a BESS but then utilising the BESS to mitigate the fluctuation of the PV power output. Or, alternatively, utilise the BESS, which is purposed for fluctuation mitigation, to assist the network during peak hours when the PV system typically does not output power any longer.

All-in-all the thesis provides solutions to three problems but takes it a step further by analysing the solutions and providing more insight into the costs involved.

8.2 Recommendations & Future Work

8.2.1 Battery State-of-Health Model

In Chapter 2, a battery state-of-health (SOH) model is implemented in Python to provide a means with which the performance of a battery chemistry can be estimated with ease. Is is found that for the lead-acid ($PbSO_4$) chemistry the SOH estimation is not accurate across the whole depth-of-discharge range. Thus, for future work, it is recommended

that a more complex model be developed for this chemistry, like the modified Arrhenius equation used for the lithium chemistry.

8.2.2 Fluctuation Mitigation of PV Power Output

In Chapter 4 an inverter ramp-rate control strategy is chosen as fluctuation mitigation method. It is implemented in Python and assessed in further detail. For future work, it is recommended that the competing moving average strategy be implemented as well and its performance compared to that of the ramp-rate strategy. This comparison can be done in terms of required BESS specifications and costs.

8.2.3 Network Strengthening for PV Integration

In Chapter 5, the network is modelled using weak network characteristics and a assumption of no inertia. The inertia of an electric network provides resistance to change in frequency. It can be of interest to develop a new network model that incorporates inertia in terms of turbine generators to study the effect of a sudden power loss on the network and how the BESS can assist in providing a stable network frequency.

8.2.4 Sizing for Peak Load Shaving

In Chapter 6 the effect of PV on the BESS requirements is briefly touched upon. It is recommended that further investigation be done into the energy profiles of businesses and the contribution PV makes since these profiles typically reach peaks during daytime.

Bibliography

[1] M. Gaikwad, "Push for Renewables Grows Stronger," Cmfe News, Tech. Rep., August 2017. [Online]. Available: https://cmfenews.com/push-renewables-grows-stronger/

[2] P. Papapetrou, "Enabling Renewable Energy in South Africa: Assessing the Renewable Energy Independent Power Producer Procurement Programme," World Wildlife Fund (WWF), Tech. Rep., 2014. [Online]. Available: http://awsassets.wwf.org.za/downloads/enabling-re-in-sa.pdf

[3] J. Johnson, B. Schenkman, A. Ellis, J. Quiroz, and C. Lenox, "Initial operating experience of the 1.2-MW La Ola photovoltaic system," in *2012 IEEE 38th Photovoltaic Specialists Conference (PVSC) PART 2*, June 2012, pp. 1–6.

[4] S. Abdollahy, A. Mammoli, F. Cheng, A. Ellis, and J. Johnson, "Distributed compensation of a large intermittent energy resource in a distribution feeder," in *2013 IEEE PES Innovative Smart Grid Technologies Conference (ISGT)*, Feb 2013, pp. 1–6.

[5] C. Vartanian, "Grid Stability Battery Systems for Renewable Energy Success," in *2010 IEEE Energy Conversion Congress and Exposition*, September 2010, pp. 132–135.

[6] E. Telaretti and L. Dusonchet, "Battery storage systems for peak load shaving applications: Part 1: Operating strategy and modification of the power diagram," in *2016 IEEE 16th International Conference on Environment and Electrical Engineering (EEEIC)*, June 2016, pp. 1–6.

[7] F. Lambert, "Electric vehicle battery cost dropped 80% in 6 years down to $227/kwh - tesla claims to be below $190/kwh," January 2017. [Online]. Available: https://electrek.co/2017/01/30/electric-vehicle-battery-cost-dropped-80-6-years-227kwh-tesla-190kwh/

[8] S. Vazquez, S. M. Lukic, E. Galvan, L. G. Franquelo, and J. M. Carrasco, "Energy storage systems for transport and grid applications," *IEEE Transactions on Industrial Electronics*, vol. 57, no. 12, pp. 3881–3895, Dec 2010.

[9] Z. Wang, M. Xia, and M. Lemmon, "Voltage stability of weak power distribution networks with inverter connected sources," in *2013 American Control Conference*, June 2013, pp. 6577–6582.

[10] S. Chanda and B. Das, "Identification of weak buses in a power network using novel voltage stability indicator in radial distribution system," in *India International Conference on Power Electronics 2010 (IICPE2010)*, Jan 2011, pp. 1–4.

[11] Z. Taylor, H. Akhavan-Hejazi, E. Cortez, L. Alvarez, S. Ula, M. Barth, and H. Mohsenian-Rad, "Battery-assisted distribution feeder peak load reduction: Stochastic optimization and utility-scale implementation," in *2016 IEEE Power and Energy Society General Meeting (PESGM)*, July 2016, pp. 1–5.

[12] A. S. Hintz, K. Rajashekara, and R. Prasanna, "Controller for combined peak-load shaving and capacity firming utilizing multiple energy storage units in a microgrid," in *2016 IEEE Energy Conversion Congress and Exposition (ECCE)*, Sept 2016, pp. 1–7.

[13] E. Telaretti and L. Dusonchet, "Battery storage systems for peak load shaving applications: Part 1: Operating strategy and modification of the power diagram," in *2016 IEEE 16th International Conference on Environment and Electrical Engineering (EEEIC)*, June 2016, pp. 1–6.

[14] C. Venu, Y. Riffonneau, S. Bacha, and Y. Baghzouz, "Battery storage system sizing in distribution feeders with distributed photovoltaic systems," in *2009 IEEE Bucharest PowerTech*, June 2009, pp. 1–5.

[15] M. Bellis, "History Timeline of the Battery," April 2017. [Online]. Available: https://www.thoughtco.com/battery-timeline-1991340

[16] B. University, "When Was the Battery Invented?" [Online]. Available: http://batteryuniversity.com/learn/article/when-was-thebattery-invented

[17] R. Carnegie, G. Douglas, D. Nderitu, and P. V. Preckel, *Utility Scale Energy Storage Systems: Benefits, Applications, and Technologies*. State Utility Forecasting Group, June 2013.

[18] T. Reddy, *Linden's handbook of batteries*. New York: McGraw-Hill, 2011.

[19] R. Corkish, M. A. Green, M. E. Watt, and S. R. Wenham, *Applied Photovoltaics*. Routledge, 2013.

[20] G. M. Masters, *Renewable and Efficient Electric Power Systems (Wiley - IEEE)*. Wiley-IEEE Press, 2013.

[21] W. Howard, C. Schmidt, and E. Scott, "Lithium-ion battery," July 2009, US Patent 7,563,541. [Online]. Available: http://www.google.com/patents/US7563541

[22] J. Salminen, D. Steingart, and T. Kallio, "Fuel cells and batteries," in *Future Energy - Improved Sustainable and Clean Options for Our Planet*. Amsterdam London: Elsevier, 2008, pp. 259–276.

[23] A. Väyrynen and J. Salminen, "Modular li-ion battery systems for electric and hybrid powertrains," in *6th AVL International Commercial Powertrain Conference*. Graz, Austria: AVL List GmbH, May 2011.

[24] S. Vazquez, S. M. Lukic, E. Galvan, L. G. Franquelo, and J. M. Carrasco, "Energy Storage Systems for Transport and Grid Applications," *IEEE Transactions on Industrial Electronics*, vol. 57, no. 12, pp. 3881–3895, 2010.

[25] Meridian International Research, "The Trouble with Lithium 2 Under the Microscope," *Meridian International Research*, pp. 1–54, May 2008.

[26] I. Rade and B. A. Andersson, "Requirement for metals of electric vehicle batteries," *Journal of Power Sources*, vol. 93, no. 1–2, pp. 55–71, 2001.

[27] G. Wang, M. Ciobotaru, and V. G. Agelidis, "Power smoothing of large solar PV plant using hybrid energy storage," *IEEE Transactions on Sustainable Energy*, vol. 5, no. 3, pp. 834–842, 2014.

[28] S. C. Smith, P. Sen, and B. Kroposki, "Advancement of energy storage devices and applications in electrical power system," *2008 IEEE Power and Energy Society General Meeting - Conversion and Delivery of Electrical Energy in the 21st Century*, pp. 1–8, 2008.

[29] H. Chen, T. N. Cong, W. Yang, C. Tan, Y. Li, and Y. Ding, "Progress in electrical energy storage system: A critical review," *Progress in Natural Science*, vol. 19, no. 3, pp. 291–312, 2009.

[30] B. Lawson, "Battery and Energy Technologies: Nickel Cadmium Batteries," 2005. [Online]. Available: http://www.mpoweruk.com/nicad.htm

[31] J. Tarabay and N. Karami, "Nickel metal hydride battery: Structure, chemical reaction, and circuit model," in *2015 Third International Conference on Technological Advances in Electrical, Electronics and Computer Engineering (TAEECE)*, April 2015, pp. 22–26.

[32] M. Broussely, *Industrial Applications of Batteries From Cars to Aerospace and Energy Storage*. Burlington: Elsevier Science, 2007.

[33] M. Skyllas-Kazacos, G. Kazacos, G. Poon, and H. Verseema, "Recent advances with unsw vanadium-based redox flow batteries," *International Journal of Energy Research*, vol. 34, no. 2, pp. 182–189, 2010.

[34] H. Bindner, C. Ekman, O. Gehrke, and F. Isleifsson, "Characterization of Vanadium Flow Battery," *Tech. Rep. Riso-R-1753(EN), 2011*, no. October, pp. 1–29, 2010.

[35] V. Smith, I. Tshwagong, M. Ntusi, and C. Masike, "Ancillary Services Technical Requirements for 2017/18 - 2021/22," Sep 2016.

[36] J. Wang, P. Liu, J. Hicks-Garner, E. Sherman, S. Soukiazian, M. Verbrugge, H. Tataria, J. Musser, and P. Finamore, "Cycle-life model for graphite-LiFePO4 cells," *Journal of Power Sources*, vol. 196, no. 8, pp. 3942–3948, 2011.

[37] B. Y. Liaw, E. Roth, R. G. Jungst, G. Nagasubramanian, H. L. Case, and D. H. Doughty, "Correlation of arrhenius behaviors in power and capacity fades with cell impedance and heat generation in cylindrical lithium-ion cells," *Journal of Power Sources*, vol. 119 - 121, pp. 874 – 886, 2003. [Online]. Available: http://www.sciencedirect.com/science/article/pii/S0378775303001964

[38] S. Ebbesen, P. Elbert, and L. Guzzella, "Battery State-of-Health Perceptive Energy Management for Hybrid Electric Vehicles," *IEEE Trans. Veh. Technol.*, vol. 61, no. 7, pp. 2893–2900, 2012.

[39] Y. Gao, J. Jiang, C. Zhang, W. Zhang, Z. Ma, and Y. Jiang, "Lithium-ion battery aging mechanisms and life model under different charging stresses," *Journal of Power Sources*, vol. 356, pp. 103 – 114, 2017. [Online]. Available: http://www.sciencedirect.com/science/article/pii/S0378775317305876

[40] M. Jongerden and B. Haverkort, "Battery modeling," *Technical Report TR-CTIT-08-01*, 2008.

[41] C. Lyu, Q. Lai, L. Wang, J. Li, and W. Cong, "A healthy charging method based on estimation of average internal temperature using an electrochemical-thermal coupling model for lifepo4 battery," in *2016 Prognostics and System Health Management Conference (PHM-Chengdu)*, Oct 2016, pp. 1–6.

[42] R. Ahmed, M. E. Sayed, I. Arasaratnam, J. Tjong, and S. Habibi, "Reduced-order electrochemical model parameters identification and soc estimation for healthy and aged li-ion batteries part i: Parameterization model development for healthy batteries," *IEEE Journal of Emerging and Selected Topics in Power Electronics*, vol. 2, no. 3, pp. 659–677, Sept 2014.

[43] S. Abu-Sharkh and D. Doerffel, "Rapid test and non-linear model characterisation of solid-state lithium-ion batteries," *Journal of Power Sources*, vol. 130, no. 1-2, pp. 266 – 274, 2004. [Online]. Available: http://www.sciencedirect.com/science/article/pii/S0378775303011455

[44] O. Tremblay, L. A. Dessaint, and A. I. Dekkiche, "A generic battery model for the dynamic simulation of hybrid electric vehicles," in *2007 IEEE Vehicle Power and Propulsion Conference*, Sept 2007, pp. 284–289.

[45] A. Rahmoun and H. Biechl, "Modelling of Li-ion batteries using equivalent circuit diagrams," *Przeglad Elektrotechniczny*, vol. 2, no. 7, pp. 152–156, 2012. [Online]. Available: http://red.pe.org.pl/articles/2012/7b/40.pdf

[46] V. Sangwan, R. Kumar, and A. K. Rathore, "Estimation of battery parameters of the equivalent circuit model using grey wolf optimization," in *2016 IEEE 6th International Conference on Power Systems (ICPS)*, March 2016, pp. 1–6.

[47] M. Chen and G. A. Rincon-Mora, "Accurate electrical battery model capable of predicting runtime and i-v performance," *IEEE Transactions on Energy Conversion*, vol. 21, no. 2, pp. 504–511, June 2006.

[48] S. Drouilhet and B. L. Johnson, "A Battery Life Prediction Method for Hybrid Power Applications Preprint," *35th AIAAA Aerospace Science Meeting and Exhibit*, January 1997.

[49] H. Bindner, T. Cronin, P. Lundsager, J. F. Manwell, U. Abdulwahid, and I. Baring-gould, "Lifetime Modelling of Lead Acid Batteries," *Risø Nat*, vol. 1515, pp. 1–81, April 2005. [Online]. Available: http://130.226.56.153/rispubl/VEA/veapdf/ris-r-1515.pdf

[50] K. J. Laidler, *Chemical Kinetics*, 3rd ed. Pearson, 1987.

[51] I. Bloom, B. W. Cole, J. J. Sohn, S. A. Jones, E. G. Polzin, V. S. Battaglia, G. L. Henriksen, C. Motloch, R. Richardson, T. Unkelhaeuser, D. Ingersoll, and H. L. Case, "An accelerated calendar and cycle life study of Li-ion cells," *Journal of Power Sources*, vol. 101, no. 2, pp. 238–247, 2001.

[52] R. K. Jaworski, "Effects of nonlinearity of arrhenius equation on predictions of time to failure for batteries exposed to fluctuating temperatures," in *INTELEC - Twentieth International Telecommunications Energy Conference (Cat. No.98CH36263)*, 1998, pp. 289–296.

[53] S. McCluer, "Wanted: Real word battery life prediction," in *Battcon - International Stationary Battery Conference*, 2003.

[54] Y. Yang, X. Hu, D. Qing, and F. Chen, "Arrhenius equation-based cell-health assessment: Application to thermal energy management design of a hev nimh battery pack," *Energies*, vol. 6, no. 5, pp. 2709–2725, 2013. [Online]. Available: http://www.mdpi.com/1996-1073/6/5/2709

[55] L. Ma, "Lithium-ion battery life evaluation method based on fuzzy nonlinear accelerated degradation process," in *2016 10th International Conference on Software, Knowledge, Information Management Applications (SKIMA)*, Dec 2016, pp. 309–313.

[56] B. Torres, V. Quintero, C. Estevez, M. Orchard, and C. Azurdia, "Soc control for improved battery life and throughput performance under vst-tdma," *Electronics Letters*, vol. 53, no. 3, pp. 183–185, 2017.

[57] G. Lacey, G. Putrus, and E. Bentley, "Smart ev charging schedules: supporting the grid and protecting battery life," *IET Electrical Systems in Transportation*, vol. 7, no. 1, pp. 84–91, 2017.

[58] J. Jousse, E. Lemaire, N. Ginot, C. Batard, and J. F. Diouris, "Assessment of lithium ion lifepo4 cells usage in photovoltaic standalone systems," in *IECON 2013 - 39th Annual Conference of the IEEE Industrial Electronics Society*, November 2013, pp. 1530–1535.

[59] F. J. Lin, M. S. Huang, Y. C. Hung, C. H. Kuan, S. L. Wang, and Y. D. Lee, "Kang type probabilistic fuzzy neural network control for grid-connected lifepo4 battery storage system," *IET Power Electronics*, vol. 6, no. 6, pp. 1029–1040, July 2013.

[60] M. Świerczyński, D. Stroe, A. I. Stan, and R. Teodorescu, "The lifetime of the lifepo4/c battery energy storage system when used for smoothing of the wind power plant variations," in *IECON 2013 - 39th Annual Conference of the IEEE Industrial Electronics Society*, November 2013, pp. 6825–6830.

[61] W. Marańda, "Capacity degradation of lead-acid batteries under variable-depth cycling operation in photovoltaic system," in *22nd International Conference Mixed Design of Integrated Circuits Systems (MIXDES)*, June 2015, pp. 552–555.

[62] E. Bellini, "South Africa's PV capacity reaches 1.47 GW, new PV installations for 2016 total 509 MW," March 2017. [Online]. Available: https://www.pv-magazine.com/2017/03/17/south-africas-pv-capacity-reaches-1-47-gw-new-pv-installations-for-2016-total-509-mw/

[63] M. J. E. Alam, K. M. Muttaqi, and D. Sutanto, "A Novel Approach for Ramp-Rate Control of Solar PV Using Energy Storage to Mitigate Output Fluctuations Caused by Cloud Passing," *IEEE Transactions on Energy Conversion*, vol. 29, no. 2, pp. 507–518, June 2014.

[64] M. Sengupta and A. Andreas, "Oahu Solar Measurement Grid (1-Year Archive): 1-Second Solar Irradiance; Oahu, Hawaii (Data)," 2014. [Online]. Available: https://dx.doi.org/10.7799/1052451

[65] N. Kakimoto, H. Satoh, S. Takayama, and K. Nakamura, "Ramp-Rate Control of Photovoltaic Generator With Electric Double-Layer Capacitor," *IEEE Transactions on Energy Conversion*, vol. 24, no. 2, pp. 465–473, June 2009.

[66] T. Kinjo, T. Senjyu, N. Urasaki, and H. Fujita, "Output levelling of renewable energy by electric double-layer capacitor applied for energy storage system," *IEEE Transactions on Energy Conversion*, vol. 21, no. 1, pp. 221–227, March 2006.

[67] T. Monai, I. Takano, H. Nishikawa, and Y. Sawada, "A collaborative operation method between new energy-type dispersed power supply and EDLC," *IEEE Transactions on Energy Conversion*, vol. 19, no. 3, pp. 590–598, Sept 2004.

[68] S. Rahman and K. S. Tam, "A feasibility study of photovoltaic-fuel cell hybrid energy system," *IEEE Transactions on Energy Conversion*, vol. 3, no. 1, pp. 50–55, Mar 1988.

[69] K. S. Tam, P. Kumar, and M. Foreman, "Enhancing the utilization of photovoltaic power generation by superconductive magnetic energy storage," *IEEE Transactions on Energy Conversion*, vol. 4, no. 3, pp. 314–321, Sep 1989.

[70] T. D. Hund, S. Gonzalez, and K. Barrett, "Grid-Tied PV System Energy Smoothing," in *2010 35th IEEE Photovoltaic Specialists Conference*, June 2010, pp. 002 762–002 766.

[71] J. Traube, F. Lu, D. Maksimovic, J. Mossoba, M. Kromer, P. Faill, S. Katz, B. Borowy, S. Nichols, and L. Casey, "Mitigation of Solar Irradiance Intermittency in Photovoltaic Power Systems With Integrated Electric-Vehicle Charging Functionality," *IEEE Transactions on Power Electronics*, vol. 28, no. 6, pp. 3058–3067, June 2013.

[72] A. Ellis, D. Schoenwald, J. Hawkins, S. Willard, and B. Arellano, "PV output smoothing with energy storage," in *2012 38th IEEE Photovoltaic Specialists Conference*, June 2012, pp. 001 523–001 528.

[73] S. G. Tesfahunegn, Ø. Ulleberg, P. J. Vie, and T. M. Undeland, "PV Fluctuation Balancing Using Hydrogen Storage - a Smoothing Method for Integration of PV Generation into the Utility Grid," *Energy Procedia*, vol. 12, pp. 1015 – 1022, 2011. [Online]. Available: http://www.sciencedirect.com/science/article/pii/S187661021101959X

[74] S. Abdollahy, A. Mammoli, F. Cheng, A. Ellis, and J. Johnson, "Distributed compensation of a large intermittent energy resource in a distribution feeder," in *2013 IEEE PES Innovative Smart Grid Technologies Conference (ISGT)*, February 2013, pp. 1–6.

[75] X. Li, D. Hui, and X. Lai, "Battery Energy Storage Station (BESS)-Based Smoothing Control of Photovoltaic (PV) and Wind Power Generation Fluctuations," *IEEE Transactions on Sustainable Energy*, vol. 4, no. 2, pp. 464–473, April 2013.

[76] C. A. Hill, M. C. Such, D. Chen, J. Gonzalez, and W. M. Grady, "Battery Energy Storage for Enabling Integration of Distributed Solar Power Generation," *IEEE Transactions on Smart Grid*, vol. 3, no. 2, pp. 850–857, June 2012.

[77] C. J. Coe, A. N. Hurst, M. I. Hardin, M. C. Such, and R. T. Jennings, "Managing renewable power generation,," in *U.S. Patent 20110273129*, November 2011.

[78] J. S. Stein, C. W. Hansen, and M. J. Reno, "The variability index: A new and novel metric for quantifying irradiance and PV output variability," in *World Renewable Energy Forum*, 2012, pp. 13–17.

[79] P. Arjyadhara, S. M. Ali, and J. Chitralekha, "Analysis of Solar PV cell Performance with Changing Irradiance and Temperature," *International Journal Of Engineering And Computer Science*, vol. 2, no. 1, pp. 214–220, 2013.

[80] M. Q. Raza, M. Nadarajah, and C. Ekanayake, "On recent advances in pv output power forecast," *Solar Energy*, vol. 136, pp. 125 – 144, 2016. [Online]. Available: http://www.sciencedirect.com/science/article/pii/S0038092X16302547

[81] Lazard, "Lazard's Levelized Cost of Storage," no. 2.0, December 2016. [Online]. Available: https://www.lazard.com/media/438042/lazard-levelized-cost-of-storage-v20.pdf

[82] ——, "Lazard's Levelized Cost of Storage," no. 1.0, November 2015. [Online]. Available: https://www.lazard.com/media/2391/lazards-levelized-cost-of-storage-analysis-10.pdf

[83] F. Lambert, "Electric vehicle battery cost dropped 80% in 6 years down to $227/kWh - Tesla claims to be below $190/kWh," *Electrek*, January 2017. [Online]. Available: https://electrek.co/2017/01/30/electric-vehicle-battery-cost-dropped-80-6-years-227kwh-tesla-190kwh/

[84] Neil Hughes, "Apple pushes supply chain to adopt renewable energy, gets 3 more suppliers to go all-green," Apple Insider, Tech. Rep., April 2017. [Online]. Available: http://appleinsider.com/articles/17/04/13/apple-pushes-supply-chain-to-adopt-renewable-energy-gets-3-more-suppliers-to-go-all-green

[85] IRENA, "Renewable Energy in District Heating and Cooling," International Renewable Energy Agency (IRENA), Abu Dhabi, Tech. Rep., 2017. [Online]. Available: www.irena.org/remap

[86] ——, "Renewable Energy Prospects: Indonesia, a REmap analysis," International Renewable Energy Agency (IRENA), Abu Dhabi, Tech. Rep., 2017. [Online]. Available: www.irena.org/remap

[87] S. Vazquez, S. M. Lukic, E. Galvan, L. G. Franquelo, and J. M. Carrasco, "Energy storage systems for transport and grid applications," *IEEE Transactions on Industrial Electronics*, vol. 57, no. 12, pp. 3881–3895, Dec 2010.

[88] H. Nehrir, C. Wang, K. Strunz, H. Aki, R. Ramakumar, J. Bing, Z. Miao, and Z. Salameh, "A review of hybrid renewable/alternative energy systems for electric power generation: Configurations, control and applications," in *2012 IEEE Power and Energy Society General Meeting*, July 2012, pp. 1–1.

[89] "95 Projects," Energyblog, Tech. Rep., June 2017. [Online]. Available: http://energy.org.za/knowledge-tools/project-database

[90] "Grid Connection Code for RPPs in South Africa," July 2016. [Online]. Available: www.nersa.co.za

[91] M. Hartung and A. Panosyan, "Comparative Study of Tap Changer Control Algorithms for Distribution Networks With High Penetration of Renewables," *CIRED Workshop*, no. 0376, pp. 1–5, June 2014.

[92] M. Crappe, Ed., *Electric Power Systems*, 1st ed. Hoboken: Wiley, 2013.

[93] J. H. Harlow, "Load Tap Changing Control," 1996.

[94] J. D. Glover, M. S. Sarma, and T. Overbye, *Power System Analysis & Design, SI Version*. Cengage Learning, 2011.

[95] P. P. Kundur, *Power system stability and control*, ser. EPRI power system engineering series. New York, N.Y.: McGraw-Hill, 1994.

[96] A. Golieva, "Low short circuit ratio connection of wind power plants," Ph.D. dissertation, Technical University of Denmark, Delft University of Technology, The norwegian Institute for Science and Technology, 2015.

[97] S. Grunau, F. W. Fuchs, C.-a.-u. Kiel, and D. Kiel, "Effect of Wind-Energy Power Injection into Weak Grids," *EWEA - European Wind Energy Association Conference*, pp. 1–7, 2012.

[98] G. Liu, X. Cao, W. Wang, T. Ma, W. Yang, and Y. Chen, "Adaptive control strategy to enhance penetration of pv power generations in weak grid," in *2014 International Power Electronics and Application Conference and Exposition*, Nov 2014, pp. 1217–1221.

[99] A. Etxegarai, P. Eguia, E. Torres, and E. Fernandez, "Impact of wind power in isolated power systems," in *2012 16th IEEE Mediterranean Electrotechnical Conference*, March 2012, pp. 63–66.

[100] N. Sichwart, A. Eltom, and G. Kobet, "Transformer load tap changer control using iec 61850 goose messaging," in *2013 IEEE Power Energy Society General Meeting*, July 2013, pp. 1–5.

[101] D. Dohmal, "On-Load Tap-Changers For Power Transformers for Power Transformers," Regensburg, Germany, 2013. [Online]. Available: www.reinhausen.com/XparoDownload.ashx?raid=58092

[102] S. M. Knupfer, R. Hensley, P. Hertzke, P. Schaufuss, N. Laverty, and N. Kramer, *Electrifying insights: How automakers can drive electrified vehicle sales and profitability*. McKinsey & Company, January 2017.

[103] G. Delille, B. Francois, and G. Malarange, "Dynamic frequency control support by energy storage to reduce the impact of wind and solar generation on isolated power system's inertia," *IEEE Transactions on Sustainable Energy*, vol. 3, no. 4, pp. 931–939, Oct 2012.

[104] V. Knap, S. K. Chaudhary, D. I. Stroe, M. Swierczynski, B. I. Craciun, and R. Teodorescu, "Sizing of an energy storage system for grid inertial response and primary frequency reserve," *IEEE Transactions on Power Systems*, vol. 31, no. 5, pp. 3447–3456, Sept 2016.

[105] I. Ranaweera, S. Sanchez, and O. M. MidtgÃ¥rd, "Residential photovoltaic and battery energy system with grid support functionalities," in *2015 IEEE 6th International Symposium on Power Electronics for Distributed Generation Systems (PEDG)*, June 2015, pp. 1–7.

[106] S. A. Abdelrazek and S. Kamalasadan, "Integrated pv capacity firming and energy time shift battery energy storage management using energy-oriented optimization," *IEEE Transactions on Industry Applications*, vol. 52, no. 3, pp. 2607–2617, May 2016.

[107] R. D. Cook, "Detection of influential observation in linear regression," *Technometrics*, vol. 19, no. 1, pp. 15–18, 1977. [Online]. Available: http://dx.doi.org/10.1080/00401706.1977.10489493

[108] M. Lovric, Ed., *International Encyclopedia of Statistical Science*. Springer, 2010.

[109] W. G. Jacoby, "Regression III : Advanced Methods Outlying Observations," 2005. [Online]. Available: http://polisci.msu.edu/jacoby/icpsr/regress3

[110] "Studentized residuals." [Online]. Available: https://onlinecourses.science.psu.edu/stat462/node/247

[111] I. Pardoe, *Applied Regression Modeling*. Wiley, 2013.

[112] T. Georgitsioti, N. Pearsall, and I. Forbes, "Simplified levelised cost of the domestic photovoltaic energy in the UK: the importance of the feed-in tariff scheme," *IET Renewable Power Generation*, vol. 8, no. 5, pp. 451–458, July 2014.

[113] L. Ortiz, *Grid-Scale Energy Storage Balance of Systems 2015-2020: Architectures, Costs and Players*. Greentech Media, January 2016.

[114] Michael Taylor and Pablo Ralon and Andrei Ilas, *The Power to Change: Solar and Wind Cost Reduction Potential*. International Renewable Energy Agency (IRENA), June 2016.

[115] "Distributed Generation Renewable Energy Estimate of Costs," November 2015. [Online]. Available: https://www.nrel.gov/analysis/tech-lcoe-re-cost-est.html

[116] F. Lambert, "Tesla confirms base Model 3 will have less than 60 kWh battery pack option, cost is below $190/kWh and falling," April 2016. [Online]. Available: https://electrek.co/2016/04/26/tesla-model-3-battery-pack-cost-kwh/

[117] B. Zakeri and S. Syri, "Electrical energy storage systems: A comparative life cycle cost analysis," *Renewable and Sustainable Energy Reviews*, vol. 42, no. Supplement C, pp. 569 – 596, 2015. [Online]. Available: http://www.sciencedirect.com/science/article/pii/S1364032114008284